1994

Synthesis and characterization of new reduced rare-earth metal bromides

Sharon Joyce Steinwand
Iowa State University

Order Number 9503598

Synthesis and characterization of new reduced rare-earth metal bromides

Steinwand, Sharon Joyce, Ph.D.

Iowa State University, 1994

U·M·I
300 N. Zeeb Rd.
Ann Arbor, MI 48106

Synthesis and characterization of new reduced rare-earth metal bromides

by

Sharon Joyce Steinwand

A Dissertation Submitted to the

Graduate Faculty in Partial Fulfillment of the

Requirements for the Degree of

DOCTOR OF PHILOSOPHY

Department: Chemistry
Major: Inorganic Chemistry

Approved:

Signature was redacted for privacy.

In Charge of Major Work

Signature was redacted for privacy.

For the Major Department

Signature was redacted for privacy.

For the Graduate College

Iowa State University
Ames, Iowa

1994

TABLE OF CONTENTS

INTRODUCTION

For the past several years, the cluster chemistry of metal-rich halides has been studied intensively. The first such cluster compounds,[1,2] discovered in the niobium–chlorine,[3,4] niobium–fluorine,[5] and tantalum–chlorine[6] systems, were synthesized and characterized in the 1960's. Since then, a plethora of cluster-containing phases have been prepared, with both early transition metals and rare-earth metals and a variety of ligands including halogens, chalcogens, and oxides.[7-9]

Such cluster-containing compounds exhibit a fascinating variety of structures which are, in most cases, derived from transition metal M_6X_8 or M_6X_{12} units composed of M_6 octahedra which are sheathed by either eight face-capping X ligands (M_6X_8) or twelve edge-bridging X ligands (M_6X_{12}). Such units occur as discrete clusters or are condensed into extended metal-metal bonded arrays. Generally, the M_6X_8-type clusters are preferred in compounds which contain a smaller metal M and a larger ligand X and are relatively electron-rich, as in Nb_6I_{11},[10,11] Nb_6I_9S,[12] Mo_6S_8,[13] and Ti_5Te_4.[14] In contrast, the M_6X_{12} unit is found in more electron-poor phases with larger metals, as in the group III and IV metal halides, along with the presence of an interstitial atom (Z) located in the center of the M_6 octahedra.[15] Originally, the phenomenon resulted from the inclusion of impurities during synthesis, with the early examples containing light main-group elements (H,C,N), as in $Nb_6I_{11}H$,[16] $Sc_7Cl_{12}C$,[17] and $Zr_6Cl_{15}N$.[18] The interstitial atom at the M_6 center provides strong M-Z bonding interactions, as

well as its valence electrons to the metal-metal bonding levels of the otherwise electron-deficient M_6 cluster. Once the importance of the interstitial atom in cluster formation was recognized, systematic investigations were undertaken in attempts to incorporate a wide range of prospective Z atoms. Since then, elements covering a large portion of the periodic table have been encapsulated, resulting in numerous new phases and a variety of novel structures.

An abundance of compounds containing discrete M_6 clusters have been prepared in the zirconium chloride, bromide, and iodide systems,[19-29] with interstitials ranging from light main–group elements to transition metals. Additionally, inclusion of countercations, typically alkali metals, alkaline-earth metals, or rare-earth metals, has greatly increased the scope of stable compounds which adhere to the same electron rules. The prolific nature of these cluster phases has provided the opportunity for systematic studies based on both structural and electronic effects, resulting in a basic understanding of many bonding and dimensional principals.

Cluster phases in the rare-earth metal halide systems exhibit a structural chemistry including, in addition to discrete M_6 clusters, eg. $M_6I_{10}Z$,[30-32] $M_7I_{12}Z$,[31,33] $Pr_{12}I_{17}Fe$,[34] a variety of condensed cluster units. The degree of condensation ranges from bioctahedra in $Gd_{10}Cl_{18}C_4$ and related phases[35-38] to chains of edge-sharing octahedra (eg. M_4I_5Z[39,40]) or square anti-prisms (Y_4Br_4Os[41]), double chains (M_3I_3Z[42,43]), layers (eg. $GdClH_x$,[44] Gd_2Cl_2C[45], $Y_2Br_2Fe_{2+x}$[46]), and finally, three-dimensional frameworks (Gd_3Cl_3C,[47] Pr_3I_3Z[48]). Many of these phases plus other

examples have been reviewed recently.[49,50] The phases are again typically composed of M_6 octahedra which are condensed through shared edges and are sheathed by ligands. Generally, the degree of cluster condensation is controlled by the X:M ratio, with condensation proceeding until the metal unit is coordinatively saturated by the ligand.

In some cases, the inclusion of alkali metals or alkaline-earth metals into rare-earth metal halide cluster compounds has been possible.[33,51-54] The compound $Cs_2Lu_7Cl_{18}C$[51] contains octahedral Lu_6C units and is isostructural with $Cs_2Zr_7Cl_{18}H$,[55] while $CsEr_6I_{12}C$[51] adopts a structure closely related to the $Sc_7Cl_{12}N$[17] structure. Other phases include $Ca_{0.65}Pr_{0.35}(Pr_6I_{12}Co)$[33] and $RbPr_5Cl_{10}C_2$,[52] which has a novel structure built of trigonal bipyramidal Pr_5 units centered by C_2.

The existence of a group of rare-earth metal halides that are built of M_4 tetrahedral units has been known for several years.[49,50] The compounds, eg. Gd_3Cl_6N,[56] α-Gd_2Cl_3N,[57] β-$Y_2Cl_3N_x$,[58] $(Yb,Eu,Sm)_4OCl_6$,[59-60] are again stabilized by interstitial atoms, usually small main–group elements, which form strong M-Z bonds. Although the compounds tend to exhibit short M-M distances, some of these phases do not form metal-metal bonds, but instead are bound by only M-Z and M-X interactions, and are only loosely termed "cluster compounds". More recently, $M_9I_8C_4O$[61] (M = Y, Ho, Er, Lu) were discovered, which contain octahedrally coordinated C interstitials along with tetrahedrally coordinated O atoms.

The occurrence of a rare example of oligomeric cluster condensation was observed in $Y_{16}I_{20}Ru_4$[62] and in the recently discovered $Gd_{20}I_{28}Mn_4$[63]. The compounds contain $M_{16}Z_4$ units which can be described as tetramers of M_6Z clusters. Several new compounds in the scandium bromide and yttrium bromide systems have now been prepared which contain this type of oligomeric cluster as the major building block. The interstitially stabilized $M_{16}Z_4$ unit exhibits a narrow range of electronic stability, forming only with interstitial atoms and structure types that result in close to 60 electrons for cluster bonding. As the electronic nature of the interstitial varies, structural changes occur which maintain this optimal electron count.

In the following sections, the synthesis and characterization of some new reduced rare-earth metal halides will be discussed. The results are presented based on structural similarities and increasing structural complexity for a given rare-earth metal. The main emphasis will be on the new structural features exhibited in the phases, as well as their structural relationships with other cluster phases. In some cases, the magnetic properties will be presented as well.

EXPERIMENTAL

Materials

Rare-earth metals

The rare-earth metals used in the reactions were obtained from the Materials Preparation Center of Ames Laboratory. They were prepared by the metallothermic reduction of the rare-earth trifluorides by triply distilled calcium metal followed by vacuum distillation. After processing, the metals were stored inside a N_2-filled glovebox (VAC, HE-493). Impurity levels in the Pr, Sc, and Y, are listed in Table 1. Elements not listed were either present in quantities ≤1 ppm or below the detection limit. Scandium metal was in the form of strips (~3 x 5 mm), turnings, or powder. The powdered scandium was prepared by Dr. S.-J. Hwu through the thermal decomposition of ground ScH_2 under dynamic vacuum at 700-750°C and stored in a N_2-filled drybox.[64] Yttrium was cold-rolled into 2 mil sheets which were cut into small pieces (~2 x 3 mm) immediately before use. Praseodymium metal was in the form of turnings carved from a small chunk prior to use.

Table 1: Impurity levels in rare-earth metal starting materials (ppm atomic)

	H	C	N	O	F	Fe	other
Pr	558	210	121	299	<22	23	Si-2, Y-1.3, La-8, Ta-16, Nd-9
Sc	134	67	10	154	116	118	Cl-3, Cr-2, Co-2, Cu-10, Y-4.6, La-4.3, Pr-2, Nd-1.3, Tb-35
Y	176	89	13	107	<14	12	B-1.1, Cl-20, Ti-3, Cr-2, Cu-4, Zr-22, W-18

Rare-earth metal trihalides

The rare-earth metal tribromides were prepared according to the ammonium bromide route.[65-66] This method involved the oxidation of the metal by NH_4Br to form $(NH_4)_3MBr_6$. This ammonium salt was subsequently decomposed to form the rare-earth metal tribromide. The tribromides were purified by vacuum sublimation and stored in a N_2-filled dry box.

Scandium metal strips and turnings (Ames Lab, 1.5 g.) were placed in a Pyrex tube with a large excess of NH_4Br (Fisher, reagent grade). The Ar-filled tube was connected to a dry ice/acetone-cooled trap followed by an oil-filled bubbler. The material was heated to 320°C at which time H_2 and NH_3 gases were evolved. After two days of heating, the material still contained a few small pieces of unreacted metal. The material was ground in air and reheated for 14 hours, again exhibiting the evolution of gas. The resultant light-tan powder, presumably a mixture of $(NH_4)_3ScBr_6$, NH_4Br, and side products (ScOBr), was transferred to a fused-silica tube and heated under dynamic vacuum. The temperature was increased slowly over the course of two days to 550°C, during which the $(NH_4)_3ScBr_6$ decomposed and NH_4Br sublimed to the cooler end of the tube. The anhydrous $ScBr_3$ remained in the hot zone.

The $ScBr_3$ was purified by vacuum sublimation. Inside a N_2-filled glovebox, the white powder was placed in a two-piece Ta apparatus which was then placed inside a fused-silica tube. The Ta container prevented reaction of the tribromide with the fused silica and allowed for the easy removal of the

purified product. While under dynamic diffusion pump vacuum, the material was heated gradually to ~700°C, the temperature at which sublimation occurred. The purified product was characterized by powder diffraction and, when necessary, was resublimed until no ScOBr was detected. The final product, consisting of white plates and powder, was placed in a vial which was stored inside a mason jar in a N_2-filled glovebox.

YBr_3 was prepared in a manner similar to $ScBr_3$. The Y metal (Aesar's, dendrites) used was of lower purity with respect to oxygen than the Ames Lab material. This may have increased the amount of YOBr formed, but this impurity was removed in the later purification step. The formation of $(NH_4)_3YBr_6$ began at 310°C and the reaction was continued for three days. The tan powder was heated for ~12 hours at 400°C in vacuo to decompose the $(NH_4)_3YBr_6$ and sublime the NH_4Br to the cool zone. The white YBr_3 was vacuum sublimed at ~800°C and its purity confirmed by powder diffraction. YOBr is easily identified with powder diffraction, based on the presence of two strong characteristic lines.

Previously sublimed $PrBr_3$ was kindly provided by Dr. R. Llusar of Ames Laboratory. Purity of the light green powder was confirmed by powder diffraction.

Interstitial elements

Transition metals were introduced in elemental form as either powders or chunks. Powdered Ni, Ru, Rh, Pd, Os, Ir (Johnson Matthey, ≥99.9%), Re

(Aldrich, 99.99%), Cr (Aesar, 99.5%), Fe, and Cu (reagent grade) were degassed at ambient temperature and stored in small vials in a glovebox. Chunks of Co (Aesar, 99.5%), Mn (Johnson Matthey, 99.99%), and Pt strips (government issue, reagent grade) were used as received.

Main group elements were utilized as powders. Amorphous B (Aldrich, 99.999%) and spectroscopic grade graphite (National brand, Union Carbide) were readily available. PrN, kindly supplied by Dr. J. T. Zhao of Ames Laboratory, was used as a source of nitrogen. Oxygen was added in the form of Pr_6O_{11}. Both the PrN and Pr_6O_{11} were characterized by powder diffraction and found to be single phase, ie. ≥95% purity.

Alkali metals

Alkali metals were used either as the alkali-metal halide or in elemental form. The alkali-metal halides (reagent grade) were dried by slow heating under dynamic vacuum and then sublimed. Elemental sodium (Alfa, 99.9%) was preferred in some instances. The metal was freshly cut before use in order to minimize surface impurities.

Synthetic Techniques

The basic synthetic strategy involved loading a variety of stoichiometries over the compositional range of study and varying the reaction conditions to maximize the yield of new phases. When reaction products were multi-phase, the yield of other components (based on relative powder pattern intensities) was used to estimate the approximate composition of unidentified phases. Once a

compound was identified (by either powder pattern or single crystal information), attempts were made to prepare the phase in high yield.

The preparation of reduced rare-earth metal halides presents many challenges. Synthesis must generally be carried out at elevated temperatures (≥600°C) while every measure is taken to prevent contamination of the reactants. This requires a container that not only withstands high temperatures but also remains inert to the reactants and products of the synthesis. Since reaction of metal halides with traditional Pyrex or silica containers at these temperatures is well known, containers of Ta or Nb have been used extensively and with much success for the synthesis of a variety of reduced metal halides.[67] Such containers not only remain inert in these systems to >1000°C but can withstand internal pressures of as high as 30 atmospheres. The Ta or Nb containers are susceptible to attack by O_2 or H_2O at high temperatures and must be enclosed in a well-evacuated sealed silica container to prevent oxidation by air. This places a limit on the temperatures attainable using this type of container, as failure of the silica jacket occurs near 1250°C. However, this limitation was not a problem in the systems of interest. Niobium proved a better choice for most reactions in this study, due to its similar inertness to rare-earth metals and trihalides as well as most of the interstitial elements used coupled with its lower cost relative to Ta. In a few cases, Ta containers were used when formation of Nb–interstitial binary phases seemed problematic.

Another very important aspect of the synthesis of these reduced metal halides is their sensitivity to the presence of impurities in the reaction system. In fact, it was the presence of adventitious impurities in "binary" reactions that led to the discovery of many reduced Zr and rare-earth metal halides.[16,17,68,69] These phases were found to contain H, C, N, or O as interstitial atoms. In the present study, interstitial elements were purposefully introduced. However, phases formed with adventitious impurities could still cause much confusion and impede the characterization process. Thus, when preparing starting materials and loading reactions, extreme care was taken to exclude all possible sources of these light atoms.

A second problem is encountered when oxygen or water is introduced into the rare-earth metal halide systems. The reaction between O_2 or H_2O and MBr_3 to yield the corresponding MOBr is very favorable. The MOBr acts as a sink for any oxygen that enters the system. The formation of this phase, then, will change the amount of metal halide available to react with the interstitial element. That is, the stoichiometry of the reaction will have deviated from that originally loaded. This problem is intensified as the reaction temperature increases. Over long reaction periods at elevated temperatures, small amounts of oxygen-containing species are able to diffuse through SiO_2.[70] Consequently, the chances of oxygen contamination tend to increase as both reaction time and temperature are increased.

Synthesis began with the preparation of reaction containers. Niobium (and tantalum) tubing, available in 3/8" diameter, was cut into pieces 4.5 cm long and cleaned with a solution of 25% conc. HNO_3, 55% conc. H_2SO_4, and 20% conc. HF (by volume) for 15–30 seconds. The reaction was vigorous and was performed in a fume hood. The tubes were then rinsed thoroughly with running distilled water for ~20 minutes. After complete drying, one end of the tube was crimped tightly and welded shut using a tungsten-inert gas (TIG) procedure.[71] If further cleaning of the empty tube was necessary, soaking in distilled water for one day ensured the removal of all cleaning solution from the weld. The tubes were heated only slightly to prevent possible oxidation of the metal surface.

Reaction containers were loaded inside a N_2-filled glovebox equipped with a gas circulation and purification system and then welded shut. The moisture level inside the glovebox was maintained at <0.01 ppm by volume. Reactions were loaded with stoichiometries designed to prepare 150-200 mg. of a hypothetical compound. Quantities of starting materials were weighed by difference on an electronic balance with ±0.0005 g precision. Care was taken to prevent material from sticking to the rim of the Nb tube during loading, as vaporization or decomposition of this material during welding could result in the formation of holes. After addition of all starting materials, the end of the Nb tube was crimped tightly shut with a vise-grip and the tube was transferred in an air-tight container to the welder. The N_2-filled tubes were exposed to air for

only a few seconds while placing into the welding chamber. Once inside the welder, the tubes were immediately evacuated, followed by alternately purging with inert gas (He or Ar) and again evacuating until the pressure was less than 10 millitorr. The chamber was then backfilled with inert gas to just below atmospheric pressure and the tubes arc-welded shut.

The Nb reaction containers were enclosed in an evacuated fused silica vessel and then heated at elevated temperature (600–1200°C) for periods of time ranging from several days to several weeks. The Nb tubes were placed inside a silica tube connected through a long neck to a ball joint. The open end of the silica tube was sealed with a hydrogen-oxygen flame, with care taken to minimize heating of the Nb reaction containers. The Nb containers and interior of the silica tube were then etched with the afore-mentioned cleaning solution and rinsed thoroughly, first with distilled water and then by acetone. The apparatus was dried at ≤100°C before being connected to a vacuum line equipped with a mercury diffusion pump. While under dynamic vacuum, the silica container was heated repeatedly with a natural gas/oxygen torch until red hot, in order to remove as much water from the silica as possible.[72,73] After the vessel was evacuated to below the discharge level of a Tesla coil (~10^{-5} torr), the neck was sealed shut. The reactions were placed in the center of a furnace equipped with a temperature controller. Temperatures were measured by a chromel-alumel thermocouple, which was positioned next to the tube in the furnace interior. Typically, the reactions were heated quickly to temperatures near the

sublimation point of the trihalide and then maintained at or slowly ramped to temperatures between 725–1100°C. Various methods were employed to encourage crystal growth, including slow heating and cooling ramps, temperature gradients, addition of alkali-metal halides to provide a flux, and addition of $AlBr_3$ as a transporting agent.

All handling of reaction products was performed under a dry nitrogen or helium atmosphere inside a glovebox to prevent hydrolysis or oxidation of the material by moisture or oxygen. After visual examination, preparation of samples for powder diffraction, and selection of possible single crystals, the remaining sample was stored in a sealed, evacuated Pyrex ampoule.

Characterization

Visual inspection

Visual inspection of the reaction product often provided much information about the success or lack thereof of the synthesis. Reactions were opened in a drybox equipped with a binocular microscope mounted on a nearly horizontal plexiglass top. The products were carefully examined and the color, morphology and approximate amounts (by volume) of each of the materials were noted. Often, the success or failure of a reaction was evident with just this initial inspection. With experience, it was possible to identify much of the material (starting materials, MOBr, intermetallic phases, etc.) which allowed for more efficient characterization of new phases. In many cases, new phases could be recognized and separated from the bulk on the basis of color and crystal habit,

eg. black needles vs. white flakes. Even if a new material was obtained in low yield, it was possible to advance its characterization through selective sampling of the product. And though the yield estimates were crude, they were helpful in determining the likely composition of new phases.

X-ray powder diffraction

Routine characterization of these materials was accomplished with X-ray powder diffraction. This technique allowed identification of individual crystalline components of multiphase samples. Each phase exhibited a characteristic "fingerprint" which could also be used as a semiquantitative measure of its abundance in the sample. Also, the symmetry and precise lattice parameters of the compounds were determined when necessary.

After careful visual inspection, reaction products were prepared for analysis by Guinier diffraction. Samples were ground in the drybox, mixed with a small amount of Si standard (NIST, SRM-640b), and mounted between two layers of cellophane tape to prevent exposure to air. Frequently, more than one sample was prepared from a multiphase product. Powder patterns were photographically recorded with an Enraf-Nonius (FR-552) Guinier camera equipped with a rotating sample holder inside an evacuable chamber. The incident radiation was monochromatic $CuK\alpha_1$ (λ=1.540562 Å) and the range of the exposed film was from ~2–85° in 2θ, sufficient to record the position of the first five silicon lines. During the exposure, the chamber was under dynamic vacuum with a typical pressure of ~200 millitorr.

The observed powder patterns were compared to observed[74] or calculated patterns of known compounds (or hypothetical compounds with known structure types) that were generated with the program POWDER.[75] By careful examination, it was possible to identify lines characteristic of starting materials, side products, and other known phases. In multiphase samples, intensities of the strongest line of each phase were used as a rough estimate of their relative proportions in the product. However, this method was sometimes misleading, as these intensities may be affected differently by symmetry and preferred orientation from one phase to another.

When a new compound was discovered, the positions of the powder pattern lines were measured with an Enraf-Nonius Guinier viewer. These positions were converted into 2θ values with the program GUIN[76] using a quadratic equation derived from a least-squares fit of the positions of the silicon lines to known diffraction angles. If the structure type of the new phase was known, the lines were indexed manually and the lattice parameters and errors were calculated using the program LATT.[77] For phases with unknown structure types, determination of the lattice symmetry, cell parameters and indices of the lines was attempted, with limited success, using the program TREOR.[78]

Single crystal X-ray diffraction

Ultimately, the characterization of new phases with unknown structure types depended on the successful completion of single crystal X-ray diffraction studies. These studies revealed the structural geometry and stoichiometry of the

new phases, which allowed for interpretation and greater understanding of the structural and bonding features present in the new compounds.

Visual inspection of the product was very important when seeking single crystals of a new phase. The sample was searched painstakingly for particles exhibiting smooth faces or geometric shapes that might indicate single crystal growth. Lacking these features, small irregular chunks of the new phase were chosen, in the hope that suitable crystals might be located. When a likely crystal was found, it was picked up with the grease-coated tip of a glass fiber pulled from a silica rod. When necessary, powder and other material was removed from the surface of the crystal by rolling it in Apiezon-L vacuum grease. The crystal was mounted inside a glass capillary (0.2–0.5 mm dia.) where the grease held the crystal in place. The end of the capillary was plugged with grease and the capillary removed from the drybox. The capillary was sealed with a small natural gas/oxygen torch and the end was coated with molten Apiezon W wax. Prior to single crystal work, the capillary containing the crystal was mounted in a metal pin.

Crystal quality was measured by photographic methods. Initial screening was accomplished with oscillation and Laue photo techniques. Crystals exhibiting doubled spots or powder rings were set aside or discarded. The best crystals were studied further by single crystal X-ray diffraction. In some cases, Weissenberg and precession methods were employed to help determine the symmetry, lattice parameters, and space group of new phases.

Crystallographic data were collected at room temperature on a Rigaku AFC6R or Enraf-Nonius CAD4 diffractometer. Both are automated four-circle diffractometers operating with monochromatic Mo $K\alpha_1$ (λ=0.70173 Å) radiation. Use of a rotating anode for X-ray generation allows the Rigaku to operate at a higher power than the CAD4. The resultant increase in X-ray intensity permits crystallographic studies of very small or weakly diffracting crystals. Both instruments are operated by software systems that allowed for the convenient location, centering, and indexing of reflections. The systems also include programs for determination of cell parameters, lattice symmetry, and an orientation matrix. Axial photos were often used to confirm the suggested lattice parameters and Laue symmetry. Following this determination, data collection parameters were carefully chosen. Three standard reflections were measured periodically to monitor instrument and crystal stability. No significant decay was observed in any of the data sets. After data collection, Ψ-scans were measured on at least three intense reflections having χ near 90°.

Data processing included a Lorentz-polarization correction and an empirical absorption correction using an averaged Ψ-scan. Reflections were defined as observed if $I/\sigma_I \geq 3$. The data sets, usually containing redundant data, were studied carefully to identify any extinction conditions that would indicate the correct space group. Redundant data were then averaged in the chosen point group to generate a unique data set which was used for structure refinement.

The structure solution began by determination of an initial model. For a phase with a known structure type, the positional parameters of an isostructural compound were employed. If the structure was unknown, an initial model was obtained using the direct methods procedure available in the program SHELXS-86.[79]

Structure refinement was carried out with the TEXSAN[80] software package. Atomic positions and thermal parameters were refined with a full-matrix least-squares calculation followed by standard Fourier syntheses. The structure factors were calculated using neutral atomic scattering factors with corrections for both real and imaginary parts of anomalous dispersion for elements with $Z > 10$.[81] Usually, refinement of a secondary extinction coefficient was appropriate. If the empirical absorption correction seemed inadequate, an absorption correction based on the isotropic model was applied with DIFABS.[82] In some cases, it was appropriate to refine the occupancies of certain positions. Occupancies that refined to within 3σ of 100% were reset to that value. The overall quality of the solution was measured by the residual electron density observed in a final difference Fourier map, along with the values of R and R_w.

Important data collection and refinement parameters of specific structure determinations are tabulated in the corresponding results section. Positional and thermal parameters, as well as important bond distances and angles, are also reported in the results section. When available, lattice constants derived from Guinier powder patterns were used in distance and angle calculations.

Drawings of the structures were generated with ORTEP.[83] Thermal ellipsoids are drawn at the 90% probability level unless otherwise indicated. Definitions of some important structure refinement parameters are given below.

1) The linear absorption coefficient, μ

$$\mu = \frac{1}{V_c} \sum_i n_i \mu_{ia}$$

where V_c is the unit cell volume and n_i is the number of a given atom in the unit cell. μ_{ia} is the atomic absorption coefficient tabulated in the International Tables.[81]

2) The secondary extinction coefficient, g[84]

$$|F_o| = \frac{|F_c|}{1 + g|F_c|^2 Lp}$$

where L and p are the Lorentz and polarization factors.

3) The R factor for averaging data is calculated as

$$R_{ave} = \frac{\sum_{i=1}^{n}\sum_{j=1}^{m} |\langle F_i^2 \rangle - F_{ij}^2|}{\sum_{i=1}^{n} m\langle F_i^2 \rangle}$$

where n is the number of unique reflections that was observed more than once and m is the number of times a given reflection was observed. $\langle F_i^2 \rangle$ is the average value of F^2 for a unique reflection i.

4) The crystallographic R factors are defined as:

$$R = \frac{\sum_{i=1}^{n} \left(|F_{obs}|_i - |F_{calc}|_i \right)}{\sum_{i=1}^{n} |F_{obs}|_i}$$

$$R_w = \left(\frac{\sum_{i=1}^{n} w_i \left(|F_{obs}| - |F_{calc}| \right)^2}{\sum_{i=1}^{n} w_i |F_{obs}|^2} \right)^{1/2}$$

where $w = 1 / \sigma_F^2$ and n is the number of reflections

5) The coefficient U_{ij} of the anisotropic temperature factor expressions are defined as follows:

$$T=exp[-2\pi^2(U_{11}h^2a^{*2}+U_{22}k^2b^{*2}+U_{33}l^2c^{*2} +2U_{12}hka^*b^*\cos\gamma^*+2U_{13}hla^*c^*\cos\beta^*+2U_{23}klb^*c^*\cos\alpha^*)]$$

and the equivalent isotropic temperature factor is defined as

$$B_{eq}=\frac{8\pi^2}{3}\sum_{i=1}^{3}\sum_{j=1}^{3}U_{ij}a_i^*a_j^*\vec{a}_i\cdot\vec{a}_j$$

Magnetic susceptibility

Magnetic susceptibility measurements were performed to study the magnetic properties of some of the new phases. A powdered sample (~35 mg.) was enclosed in a small He-filled sealed silica apparatus. The data were collected on a SQUID (Superconducting Quantum Interference Device) by J. Ostenson of Ames Laboratory. The temperature range studied was from 6–300 K and the field strength was varied from 0.01–3.0 Tesla. Prior to data analysis, diamagnetic sample holder and core corrections were applied. The data were analyzed with a nonlinear least-squares program[85] which allowed calculation of the temperature-independent term χ_o, the Weiss constant θ, and the effective magnetic moment μ_{eff}. Results of the magnetic studies are presented under the specific compounds measured.

RESULTS AND DISCUSSION

$Y_{16}Br_{20}Ru_4$

$Y_{16}Br_{20}Ru_4$ was the first rare-earth metal bromide discovered that contains $RE_{16}Z_4$ oligomeric units. At the time of its discovery, the only other known rare-earth metal halide containing this type of oligomer was the analogous $Y_{16}I_{20}Ru_4$.[62] The synthesis of another compound built of these oligomers suggested that the $RE_{16}Z_4$ unit might be considered a new building block in reduced rare-earth metal halide structural chemistry.

Synthesis

The compound was obtained from a reaction between YBr_3, Y foil and Ru powder loaded as Y_4Br_5Ru and heated at 980°C for 24 days. The phase formed in 40% yield as black chunks and aggregates of intergrown black crystals. The remaining sample consisted of a mixture of YBr_3 (white plates), YOBr (orange transparent plates), Y_5Ru_2 (irregular gray chunks), and another unidentified phase. Higher yields of $Y_{16}Br_{20}Ru_4$ (60-85%) were obtained from reactions loaded as Y_5Br_7Ru, Y_4Br_5Ru, and Y_3Br_3Ru, all to which a small amount of $AlBr_3$ (~15 mg.) was added. The reactions were heated at 750°C for four days, slowly ramped (+5°/hr) to 850°C and maintained there for four days, then ramped again (+3°/hr) to 950°C. The reactions were heated for two more weeks at 950°C, followed by a slow cooling ramp to 700°C before turning off the furnace. Additional reaction products included YBr_3, YOBr, and a small amount of a different unidentified Y-Br-Ru compound which exhibits a powder pattern nearly

identical to that of $Y_{20}Br_{36}Ir_4$ (discussed in a later section). $Y_{16}Br_{20}Ru_4$ was obtained in nearly theoretical yield from a reaction heated under conditions similar to those just mentioned and loaded as $CsY_6Br_{10}Ru$ (slightly Ru deficient for $Y_{16}Br_{20}Ru_4$). Other reaction products were $Cs_3Y_2Br_9$ (observed powder pattern matched the stronger lines of a pattern calculated from the structure of $Cs_3Y_2I_9$,[86] hexagonal, a=7.87 Å, c=19.68 Å, but was not a perfect match), and small amounts of YBr_3 and YOBr. $Cs_3Y_2Br_9$ was formed in all reactions where Cs (as CsBr) was introduced, presumably exhausting the available alkali metal; the binary phase, CsBr, was not evident. The compound, $Y_{16}Br_{20}Ru_4$, was also observed in a reaction heated at 1100°C for 14 days followed by quenching, displaying a relatively high stability with respect to thermal decomposition. In virtually all cases, the reaction products consisted of a multiphase mixture of some combination of starting materials, YOBr, Y-Ru intermetallic phases, $Cs_3Y_2Br_9$, and rare-earth metal halide cluster phases. Sometimes the combinations were in violation of the phase rule, indicating that thermodynamic equilibrium had not been reached. The presence of $AlBr_3$ and $Cs_3Y_2Br_9$ seemed to aid the formation of $Y_{16}Br_{20}Ru_4$, presumably by increasing the mobility of YBr_3 in the gaseous state (with the former) or by acting as a flux (with the latter). Identification of all reaction products was complicated by the presence of a number of other phases that seem to occur in the Y-Br-Ru system, most of which have not been structurally characterized to date.

Structure determination

The powder pattern of the phase contains four strong low-angle lines that resemble those present in patterns calculated for the hypothetical $Y_6Br_{10}Ru$ ($Y_6I_{10}Ru$ structure[30]) and $Y_{10}Br_{18}Ru_2$ ($Gd_{10}Cl_{18}C_4$ structure[36]). Comparison to the powder pattern of $Y_{16}I_{20}Ru_4$ also showed marked similarities in line positions, although many of the line intensities were very different (largely due to the differences in scattering factors between I and Br). Based on previous results of a partial structure refinement,[87] the compound was thought to consist of infinite chains of condensed, centered Y octahedra similar to those seen in Y_4I_5C.[39]

A block-like black chunk picked from a reaction loaded as Y_4Br_5Ru was used for the single crystal structure determination. A summary of data collection and refinement parameters is given in Table 2. Data collection was performed at room temperature on a Rigaku AFC6R automated diffractometer using Mo Kα radiation. A random search located 20 reflections with an average intensity of 16,300 counts which indexed to a primitive tetragonal cell. The Laue class 4/mmm was suggested by the diffractometer software and confirmed by axial photos. A hemisphere (h,±k,±l) of data was collected between the 2θ limits of 1° and 50°, followed by measurement of three psi scans which resulted in a large transmission range of 0.194-1.000.

Structure solution began with data reduction, which included Lorentz-polarization corrections and an empirical absorption correction based on an

Table 2. Crystallographic data for $Y_{16}Br_{20}Ru_4$

Crystal data	
Formula	Y_4Br_5Ru
Space group, Z	$P4_2/nnm$, 8
a (Å)[a]	11.662(1)
c (Å)	16.997(2)
V (Å^3)	2311.6(6)
D_{calc} (g/cm^3)	4.920
μ (Mo Kα, cm^{-1})	383.2
Data collection	
Crystal dimensions, mm	0.11 x 0.17 x 0.34
Diffractometer	Rigaku AFC6R
Radiation, wavelength (Å)	Mo Kα, 0.71069
Scan mode	ω
Octant measured	h, ±k, ±l
$2\theta_{max}$, deg.	50
Refinement	
No. of measured reflections	8508
No. of independent reflections	1248
No. of indep. reflections ($I \geq 3\sigma_I$)	589
No. of variables	55
Transmission coefficient range	0.194 - 1.000
Secondary extinction coefficient	6.4(4) x 10^{-8}
R_{avg} (I>0)	0.171
R, R_w	0.0322, 0.0321
Largest residual peak, e/Å^3	1.62 (2.27 Å from Br2), -2.09

[a] Guinier cell constants from 23 lines

averaged transmission curve. Intensity statistics strongly indicated a centrosymmetric space group. The data set exhibited systematic absences for reflections of the type hk0: h+k=2n+1, indicating the presence of an n-glide perpendicular to the c-axis. Also, a majority of 0kl and h0l reflections with h+k=2n+1 were unobserved, suggesting the presence of a second n-glide along the a- and b-axes. However, due to the presence of twelve observed reflections violating the 0kl: k+l=2n condition, initial structure solution attempts were performed in space groups P4/nmm and P4/n. Data averaging in these space groups gave a slightly lower R_{avg} for Laue class 4/m than for 4/mmm (16.5% vs. 17.1% for all data). Direct methods (SHELXS-86) provided several solutions with reasonable bond lengths and coordinations; however, most of the refinements converged with R~25%. After reevaluating the extinction conditions, solution was attempted in the space group $P4_2/nnm$, disregarding the violations to the 0kl: k+l=2n condition required by the second n-glide. Direct methods yielded a solution with clearly defined Y and Ru atoms arranged in $RE_{16}Z_4$ cluster units. All data with I>0 were averaged in this space group, resulting in a R_{avg} of 17.1%. The halide atoms were located from subsequent difference Fourier calculations. The refinement was straightforward and resulted in final R-values of 3.22% and R_w=3.21%. Table 3 lists positional parameters and anisotropic thermal parameters with their associated errors. The largest peak in the final difference Fourier map was 1.62 e/Å^3 , located 2.27Å from Br2. The largest negative peak had a value of -2.09 e/Å^3. Only four reflections had

Table 3. Positional and thermal parameters for $Y_{16}Br_{20}Ru_4$

Atom	Type	x	y	z	B(eq)	U_{11}	U_{22}	U_{33}	U_{12}	U_{13}	U_{23}
Ru	8m	0.1481(1)	-x	0.31976(7)	0.87(3)	0.0112(5)	0.0112	0.0107(6)	-0.0013(9)	0.0005(5)	-0.0005
Y1	8m	0.1369(1)	-x	0.47892(8)	1.13(4)	0.0161(8)	0.0161	0.0108(7)	-0.001(1)	0.0001(6)	-0.0001
Y2	8m	0.1167(1)	-x	0.15603(9)	1.03(4)	0.0128(7)	0.0128	0.0136(8)	-0.000(1)	0.0017(5)	-0.0017
Y3	16n	0.1329(1)	0.0815(1)	0.32681(7)	1.00(5)	0.0138(8)	0.0110(7)	0.0133(5)	-0.0003(6)	-0.0002(6)	0.0005(5)
Br1	16n	0.1245(1)	0.3481(1)	0.33899(6)	1.28(6)	0.0183(8)	0.0142(8)	0.0162(6)	-0.0019(7)	0.0014(5)	0.0010(5)
Br2	8m	-0.1124(1)	-x	0.3395(1)	1.48(5)	0.0174(8)	0.0174	0.022(1)	0.003(1)	0.0002(5)	-0.0002
Br3	8m	-0.1222(1)	-x	0.0212(1)	1.53(4)	0.0193(8)	0.0193	0.0195(9)	-0.000(1)	-0.0053(6)	0.0053
Br4	8l	0.1196(1)	x	1/2	1.24(4)	0.0181(8)	0.0181	0.0110(7)	-0.001(1)	0.0007(6)	-0.0007

observed structure factors that deviated from those calculated for the final model by greater than five times $\Delta F/\sigma F$. No problems with the anisotropic thermal parameters were noted; for most atoms, the U-values did not deviate far from the isotropic values. Based on the quality of the refinement and the similarity to the structure of $Y_{16}I_{20}Ru_4$, $P4_2/nnm$ was determined the correct space group. The observed extinction violations were probably due to impurities or a small satellite on the surface of the crystal and were not indicative of a lower symmetry.

The powder pattern calculated from the structure model is in excellent agreement with the observed powder pattern. Lattice parameters based on 23 uniquely-indexed lines resulted in a tetragonal cell with dimensions of a=11.662(1) Å and c=16.997(2) Å.

Structural description

The structure of $Y_{16}Br_{20}Ru_4$ consists of $Y_{16}Ru_4$ clusters within a coordination sphere of Br ligands. The phase, isostructural with $Y_{16}I_{20}Ru_4$, can be thought of as containing small bits of intermetallic pieces surrounded by a cloud of halide atoms. The halide atoms form a shield around the clusters, effectively isolating each from its neighboring clusters. The tetragonal unit cell contains two cluster units, one centered at (1/4, 3/4, 1/4) and the other at (3/4, 1/4, 3/4).

The 20 atom metal cluster, shown in Figure 1a, consists of a tetrahedron of Ru atoms surrounded by a larger polyhedron of Y atoms. This polyhedron can be described as a distorted tetra-capped truncated tetrahedron. Its arrangement

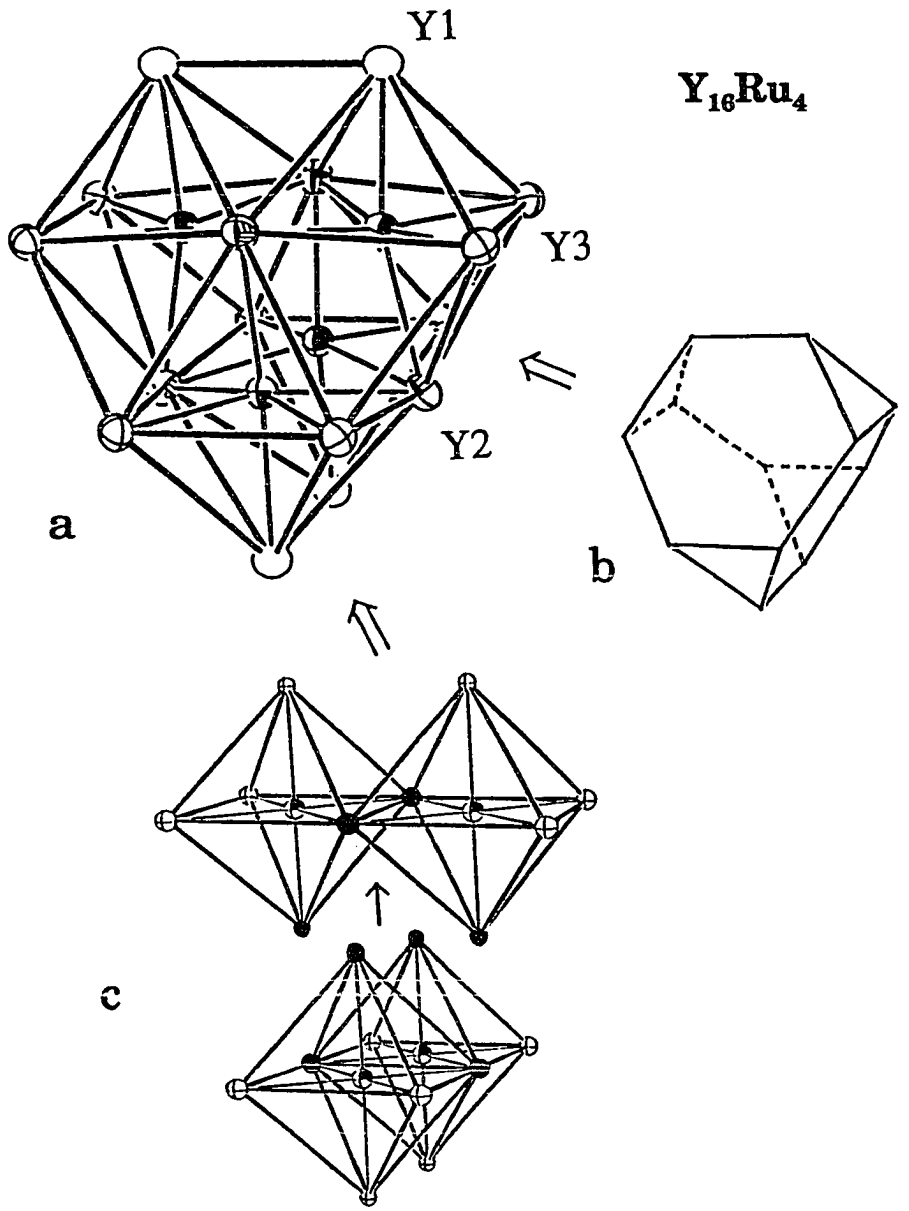

Figure 1. Illustration of a) the $Y_{16}Ru_4$ cluster ($\bar{4}2m$ symmetry, ~[110] view) as derived from a b) truncated tetrahedron or from c) pairwise condensation of Y_6Ru octahedra. $\vec{c}$ is vertical. Ru atoms are quarter-shaded.

can be visualized by considering a tetrahedron which has been cut across each corner such that four nearly hexagonal faces are created, as illustrated in Figure 1b. Replacement of each vertex of this polyhedron by a Y atom, accompanied by a Y atom capping each of the hexagonal faces, results in a Y_{16} tetra-capped truncated tetrahedron. In $Y_{16}Br_{20}Ru_4$, Y1 and Y3 atoms make up the truncated tetrahedron and Y2 atoms cap the pseudo-hexagonal faces. In actuality, the Y_{16} polyhedron has $\bar{4}2m$ (D_{2d}) symmetry; the 3-fold axis necessary for ideal tetrahedral symmetry is absent. This can be seen by a comparison of the bond distances and angles within the cluster. Tables 4 and 5 present bond distances and angles for both $Y_{16}Br_{20}Ru_4$ and $Y_{16}I_{20}Ru_4$. Notable differences are present within the Y1-Y3-Y3 triangular faces; in the bromide, the Y3-Y3 edge (d=3.535(3) Å) is shorter by nearly 0.1 Å compared to the Y1-Y3 distances of 3.629(2) Å. However, the Ru atoms which center the Y polyhedron form an ideal tetrahedron within experimental error. Similar features are present in $Y_{16}I_{20}Ru_4$.

An alternative description, emphasizing the importance of Y-Ru bonding in the structure, is obtained by viewing the metal cluster as an oligomer of Y_6Ru octahedra. Consider a pair of two edge-sharing octahedra oriented at 90° with respect to each other, as shown in Figure 1c. Sharing of the shaded atoms by both fragments results in an oligomeric 20 atom cluster, composed of condensed centered octahedra. It is convenient to use these centered octahedra as a reference in the larger cluster; then, in the upper right octahedron of the oligomer (Figure 1a), Y1 can be described as occupying an apical position, Y3

Table 4. Important bond distances in $Y_{16}Br_{20}Ru_4$ and $Y_{16}I_{20}Ru_4$

		$Y_{16}Br_{20}Ru_4$	$Y_{16}I_{20}Ru_4$			$Y_{16}Br_{20}Ru_4$	$Y_{16}I_{20}Ru_4$
Ru-Ru	(x2)	3.357(2)	3.572(3)	Y3-Ru		2.686(2)	2.684(2)
Ru-Ru		3.360(3)	3.572(3)	Y3-Y1		3.629(2)	3.662(2)
Ru-Y1		2.712(2)	2.714(3)	Y3-Y2		3.715(2)	3.794(2)
Ru-Y2		2.798(2)	2.804(2)	Y3-Y2		3.736(2)	3.803(2)
Ru-Y2	(x2)	2.831(2)	2.837(3)	Y3-Y3		3.535(3)	3.581(3)
Ru-Y3	(x2)	2.686(2)	2.684(2)	Y3-Y3		3.779(3)	3.920(3)
$\bar{d}_{Ru\text{-}Y}$		2.757	2.760	$\bar{d}_{Y3\text{-}Y}$		3.679	3.752
Y1-Ru		2.712(2)	2.714(3)	$Y3\text{-}X1^{i\text{-}a}$		2.937(2)	3.123(2)
Y1-Y1		3.731(5)	3.870(2)	$Y3\text{-}X1^{i\text{-}a}$		2.953(2)	3.132(2)
Y1-Y2	(x2)	3.685(2)	3.769(2)	$Y3\text{-}X1^{a\text{-}i}$		3.118(2)	3.417(2)
Y1-Y3	(x2)	3.629(2)	3.662(2)	$Y3\text{-}X2^{i\text{-}a}$		2.890(3)	3.115(2)
$\bar{d}_{Y1\text{-}Y}$		3.672	3.746	$Y3\text{-}X4^{i\text{-}i}$		2.981(1)	3.218(2)
$Y1\text{-}X2^{a\text{-}i}$		3.113(2)	3.467(3)	$\bar{d}_{Y3\text{-}X}$		2.976	3.201
$Y1\text{-}X3^{i\text{-}i}$	(x2)	2.905(2)	3.097(2)	$X1^{i\text{-}a}\text{-}Y2$		3.134(2)	3.309(2)
$Y1\text{-}X4^{i\text{-}i}$	(x2)	3.019(2)	3.223(2)	$X1^{i\text{-}a}\text{-}Y3$		2.937(2)	3.123(2)
$\bar{d}_{Y1\text{-}X}$		2.992	3.221	$X1^{i\text{-}a}\text{-}Y3$		2.953(2)	3.132(2)
Y2-Ru	(x2)	2.798(2)	2.804(7)	$X1^{a\text{-}i}\text{-}Y3$		3.118(2)	3.417(2)
Y2-Ru		2.831(2)	2.837(3)	$X2^{a\text{-}i}\text{-}Y1$		3.113(2)	3.467(3)
Y2-Y1	(x2)	3.685(2)	3.769(2)	$X2^{i\text{-}a}\text{-}Y3$	(x2)	2.890(3)	3.115(2)
Y2-Y2		4.398(4)	4.284(2)	$X3^{i\text{-}i}\text{-}Y1$	(x2)	2.905(2)	3.097(2)
Y2-Y2	(x2)	4.458(3)	4.337(3)	$X3^{i\text{-}i}\text{-}Y2$		3.015(2)	3.199(3)
Y2-Y3	(x2)	3.715(2)	3.794(2)	$X4^{i\text{-}i}\text{-}Y1$	(x2)	3.019(2)	3.223(2)
Y2-Y3	(x2)	3.736(2)	3.803(2)	$X4^{i\text{-}i}\text{-}Y3$	(x2)	2.981(1)	3.218(2)
$\bar{d}^{b}_{Y2\text{-}Y}$		3.712	3.789	X-X		>3.71	>3.94
$Y2\text{-}X1^{i\text{-}a}$	(x2)	3.134(2)	3.309(2)	$\bar{d}^{b}_{Y\text{-}Y}$		3.687	3.761
$Y2\text{-}X3^{i\text{-}i}$		3.015(2)	3.199(3)	$\bar{d}_{Y\text{-}X}$		3.000	3.219
$\bar{d}_{Y2\text{-}X}$		3.094	3.272				

a and i designate outer (terminal) and inner (bridging) connectivity of the halide to Y atoms.
b Y2-Y2 distances not included.

Table 5. Important bond angles in $Y_{16}Br_{20}Ru_4$ and $Y_{16}I_{20}Ru_4$

			$Y_{16}Br_{20}Ru_4$	$Y_{16}I_{20}Ru_4$				$Y_{16}Br_{20}Ru_4$	$Y_{16}I_{20}Ru_4$
Y1	Ru	$Y2^{ax}$	165.52(9)	169.57(5)	Y1	$Y3^{e}$	$Y3^{e}$	60.86(3)	60.73(3)
Y1	Ru	$Y2^{e}$	83.93(5)	86.16(6)	Y1	$Y3^{e}$	Y3	118.87(5)	119.22(4)
Y1	Ru	$Y3^{e}$	84.50(6)	85.46(6)	$Y2^{ax}$	$Y3^{e}$	$Y2^{e}$	73.51(6)	69.62(5)
$Y2^{ax}$	Ru	$Y2^{e}$	104.76(5)	100.49(7)	$Y2^{ax}$	$Y3^{e}$	$Y3^{e}$	61.59(2)	61.84(3)
$Y2^{ax}$	Ru	$Y3^{e}$	84.61(5)	86.78(6)	$Y2^{ax}$	$Y3^{e}$	Y3	59.79(3)	59.05(3)
$Y2^{e}$	Ru	$Y2^{e}$	103.62(8)	99.63(4)	$Y2^{e}$	$Y3^{e}$	$Y3^{e}$	96.64(4)	95.30(3)
$Y2^{e}$	Ru	$Y3^{e}$	85.85(4)	87.72(4)	$Y2^{e}$	$Y3^{e}$	Y3	59.25(4)	58.82(4)
$Y2^{e}$	Ru	$Y3^{e}$	164.15(7)	168.45(7)	$Y3^{e}$	$Y3^{e}$	Y3	120.74(2)	120.53(2)
$Y3^{e}$	Ru	$Y3^{e}$	82.29(8)	83.72(7)	$Y2^{i}$	X1	$Y3^{i}$	75.37(5)	72.22(3)
Ru	Ru	Y1	91.75(4)	90.66(4)	$Y2^{i}$	X1	$Y3^{i}$	75.64(5)	72.31(3)
Ru	Ru	Y2	101.35(4)	97.84(4)	$Y2^{1}$	X1	$Y3^{a2}$	177.74(5)	172.89(5)
Y2	Y1	Y2	73.29(7)	69.27(5)	$Y3^{i1}$	X1	$Y3^{a2}$	102.37(5)	101.79(4)
Y2	Y1	Y3	61.43(3)	61.54(4)	$Y3^{i1}$	X1	$Y3^{a2}$	104.05(6)	102.96(4)
Y2	Y1	Y3	95.91(5)	94.55(6)	$Y3^{i}$	X1	$Y3^{i}$	79.82(5)	77.62(5)
Y3	Y1	Y3	58.29(5)	58.54(5)	$Y1^{a}$	X2	$Y3^{i}$	100.15(7)	99.40(4)
Y1	Y2	Y1	60.83(7)	61.90(4)	$Y3^{i}$	X2	$Y3^{i}$	75.39(7)	70.17(5)
Y1	Y2	Y3	58.56(4)	57.85(3)	$Y1^{i}$	X3	$Y1^{i}$	79.91(9)	77.48(4)
Y1	Y2	Y3	118.74(6)	119.39(5)	$Y1^{i}$	X3	$Y2^{i}$	76.97(5)	73.51(6)
Y1	Y2	Y3	119.12(4)	119.76(4)	$Y1^{i1}$	X4	$Y1^{i2}$	98.44(8)	97.61(3)
Y1	Y2	Y3	165.53(7)	169.08(6)	$Y1^{i}$	X4	$Y3^{i}$	74.43(4)	69.30(5)
Y3	Y2	Y3	163.96(7)	167.97(6)	$Y1^{i1}$	X4	$Y3^{i2}$	100.30(5)	102.56(5)
Y1	$Y3^{e}$	$Y2^{ax}$	96.95(5)	95.68(5)	$Y3^{i1}$	X4	$Y3^{i2}$	172.1(1)	168.14(6)
Y1	$Y3^{e}$	$Y2^{e}$	60.02(5)	60.61(4)					

ax and e refer to axial and equatorial positions in pseudo-octahedral coordination around a Ru site.

i and a designate inner (bridging) and outer (terminal) connectivity of the halide with respect to the metal atoms of an oligomeric cluster. Numbers 1 and 2 are added when the connections involve two oligomers.

occupies two equatorial positions, and Y2 occupies two equatorial positions and the lower apical position. Any use of nomenclature defined for octahedral coordination is with respect to the centering atom (Ru) of a given octahedron.

Bond distances within the cluster are comparable to those found in other reduced rare-earth metal halide compounds. The Y-Ru distances in $Y_{16}Br_{20}Ru_4$ range from 2.686(2) Å to 2.831(2) Å, with an average of 2.757 Å. The corresponding distances in the iodide cluster are nearly identical. These distances are well within the range of Y-Ru distances observed in other Ru-centered Y octahedra, as in $Y_6I_{10}Ru$[30] and Y_3I_3Ru,[42] and are shorter than the sum of the single bond metallic radii of Ru and Y of 2.862 Å given by Pauling.[88] Bond distances between Y atoms range from 3.535(3) Å to 3.779(3) Å with $\bar{d}_{Y\text{-}Y}$ = 3.687 Å, which corresponds to a Pauling bond order of 0.17. Each Y1 and Y3 atom is bonded to five other Y atoms in the cluster. Y2 atoms are bonded to six other Y atoms; the increase in coordination number is accompanied by a slight increase in the average Y2-Y bond distance compared to the average Y1-Y and Y3-Y distances. The average Y-Y distance observed in $Y_{16}Br_{20}Ru_4$ is about 0.07 Å smaller than those of the iodide phase. This change is most likely due to differences in matrix effects caused by the coordinating halides. The Y-Y distances are similar to those in other reduced rare-earth metal halides and in Y metal where $d_{Y\text{-}Y}$ = 3.55 Å, 3.65 Å.[89] The Ru atoms are separated by a distance of 3.36 Å, corresponding to a Pauling bond order of 0.04, implying that Ru-Ru bonding is nearly negligible.

The Y_6Ru "octahedra" in both $Y_{16}Br_{20}Ru_4$ and $Y_{16}I_{20}Ru_4$ are very irregular. A large deviation from ideal octahedral geometry is evident in the bond angles as well as distances. Especially in the bromide, the Ru atom is shifted toward the center of the oligomer, ie. toward the other Ru atoms, and is not in the center of the octahedron; *trans* angles in the bromide are 165.5° and 164.2° (x2) and the Y1-Ru-Y3 and Y1-Ru-$Y2^{eq}$ angles are notably smaller than 90°. The Y1 atom mimics the movement of the Ru atom, maintaining its apical position; the Ru-Ru-Y1 angle is 91.8°. The Y2 atoms deviate the farthest from ideal octahedral geometry; the Ru-Ru-Y2 angle is 101.3° and the Y2-Y2 distances are over 0.7 Å longer than the other Y-Y distances that define the "octahedron" around each Ru atom. Similar distortions from octahedral geometry are present in $Y_{16}I_{20}Ru_4$, but with a smaller magnitude.

Deviation of the Y atoms from ideal octahedral coordination around the Ru can be better understood by imagining the pairwise condensation of Y_6Ru octahedra. In figure 1c, the ideal octahedra fit together perfectly to form a tetramer, but leave one apical Y atom (Y1 in the $Y_{16}Ru_4$ oligomer) from each octahedron with only four other coordinating Y atoms. Meanwhile, the Y atoms fusing the octahedra together (Y2 in the $Y_{16}Ru_4$ oligomer) maintain bonding distances to seven other Y atoms. Such disparity in metal coordination is uncommon in rare-earth metal halide cluster chemistry. However, if these apical Y atoms (Y1) were to shift toward each other and toward the center of the oligomer, an additional Y-Y bond could form without losing the Y-Y bonding

already present. This shift would in turn require the Ru atoms to shift toward each other to maintain suitable Y-Ru distances. Shortening of the Ru-Ru distances would bring them in close proximity to the four Y atoms (Y2) that fuse the octahedra together, resulting in uncomfortably short Y-Ru contacts. In response, these Y atoms (Y2) could move away from the center of the oligomer, losing an equatorial Y-Y bonding interaction, but allowing closer approach of the remaining six coordinating Y atoms to each other. This scenario, while describing a fictitious condensation of pairs of octahedra, is consistent with the geometry of the $Y_{16}Ru_4$ oligomer and could explain how Y-Y interactions are optimized without sacrificing Y-Ru bonding. Shortening of Y1-Y1 distances could be a driving force for the displacement of the Ru atoms toward each other (and toward the center of the oligomer), especially since Ru-Ru bonding appears to be minimal. Interestingly, the largest distortions observed upon substitution of the I by Br result in a marked decrease in the relevant Y1-Y1 and Y3-Y3 bond distances (new bonds formed upon "pairwise condensation"), accompanied by an increase in the Y2-Y2 distances. The magnitude of these changes is twice the average change in Y-Y distances between the iodide and bromide phases. This demonstrates the important role that halide coordination has on the cluster geometry as well. In many metal halide cluster phases, replacement of I by Br results in a decrease in matrix or steric effects[15] (due to packing requirements of the larger I atoms in an infinite crystalline array) and perhaps allows the cluster more geometric freedom. In this structure, the smaller size of the Br

necessitates changes in the cluster geometry, evident predominantly as smaller average Y-Y bond distances and correspondingly smaller Ru-Ru distances.

The halides exhibit four distinct modes of connectivity to the Y atoms, corresponding to their four crystallographically different positions. The four Y1-Y1-Y2 triangular faces created by the formation of Y1-Y1 bonds are capped by Br3 atoms, as shown in Figure 2a. These Br3 atoms are bonded only in an inner (bridging) fashion to Y atoms in one oligomer. In Figure 2b, eight of the twelve Y2-Y3-Y3 triangular faces around the waist of the oligomer are capped as shown by Br1 atoms. These Br1 atoms are also exo (outer or ausser) to Y3 atoms of a neighboring cluster, and are designated as Br^{i-a} and Br^{a-i} connections. Figure 3a shows $Br4^{i-i}$ atoms (shaded) that bridge the Y1-Y3 edges of two oligomers simultaneously, with eight connections per oligomer. In the same picture, $Br2^{i-a}$ and $Br2^{a-i}$ atoms (open ellipsoids) bridge Y3-Y3 edges of one oligomer while occupying the site exo to Y1 atoms in an adjacent oligomer. The inner-inner and inner-outer functionality is commonly seen in metal halide cluster chemistry, the latter particularly in compounds having larger X:M ratios. Capping of triangular faces is less common, having been seen more often in binary metal halide systems and a relatively small number of interstitially-stabilized rare-earth metal compounds, including Y_4Br_4Os.[41,49] Capping of triangular faces on the oligomers allows the Y atoms to achieve coordinative saturation, while maintaining an overall stoichiometry which fulfills the electronic requirements

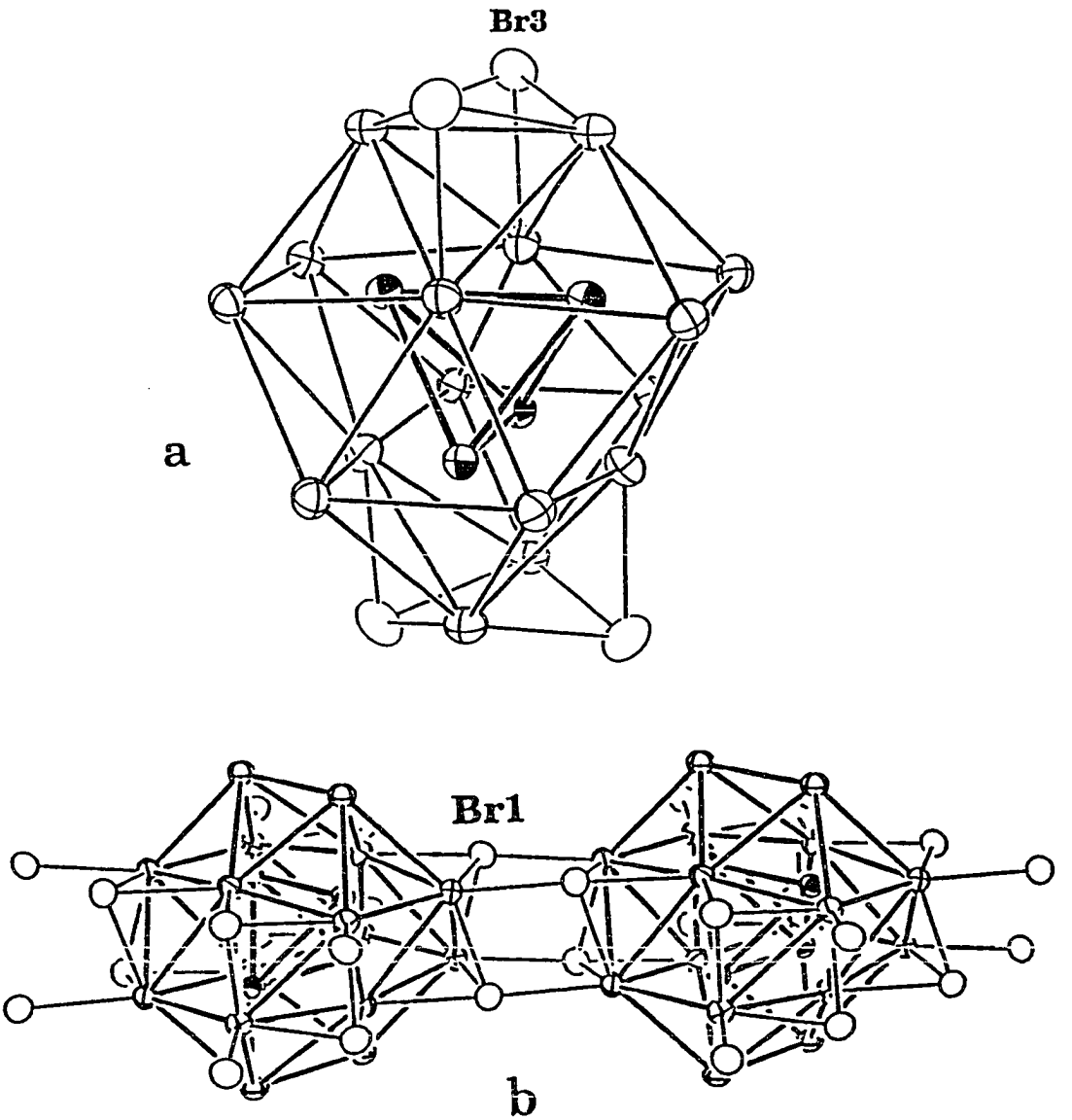

Figure 2. Two bromine (open ellipsoids) bonding modes adopted by a) Br3 atoms capping Y1-Y1-Y2 triangular faces and b) Br1 atoms capping Y2-Y3-Y3 triangular faces while bonding exo to the adjacent cluster. $\vec{c}$ is vertical.

of the cluster unit. When this bonding mode to a Y_{16} cluster is adopted, the size of the capped Y faces results in suitable Y-X bond distances, while the halide atoms maintain approximately octahedral coordination around three Y atoms. The shortening of Y-Y bonds in the bromide accomodate the decreased "reach" of the Y-Br bond compared to that of Y-I. Still, the Y-Br-Y angles indicate that the bromides have widened their "reach" to span the edges within the triangular faces compared to Y-I-Y angles in the iodide; Y1-Br3-Y1 and Y3-Br1-Y3 angles are nearly 80°, with the Y2-Br1-Y3 and Y1-Br3-Y2 angles nearer to 76°, larger than in the iodide phase in both cases. In Y_4Br_4Os, face-capping Y-Br-Y angles range from ~68-77°, and cap smaller Y triangles.

Thirty-six Br atoms surround each cluster (Figure 3b), satisfying the bonding requirements of each Y atom and precluding further cluster condensation. In Figure 3b, heavier Y-Ru and Y-Br bonds emphasize the octahedral network about each Y atom. The Y-Br bond distances range from 2.890(3) Å to 3.134(2) Å with an average value of 3.00 Å. The range of bond lengths is slightly larger than observed in Y_4Br_4Os, but the average values are comparable, even with the large differences in structure, Y_4Br_4Os consisting of infinite chains of Os-centered square antiprisms of Y atoms. Each Y1 and Y3 atom is bonded to five Br and one Ru atom in a pseudo-octahedral configuration. These Y atoms are withdrawn slightly from the square plane formed by coordinating bromides; *trans* Br-Y-Br angles at these vertices are ~156°. Each Y2 atom is bonded to three Br and three Ru atoms, the Y2 being shifted toward the three Ru atoms

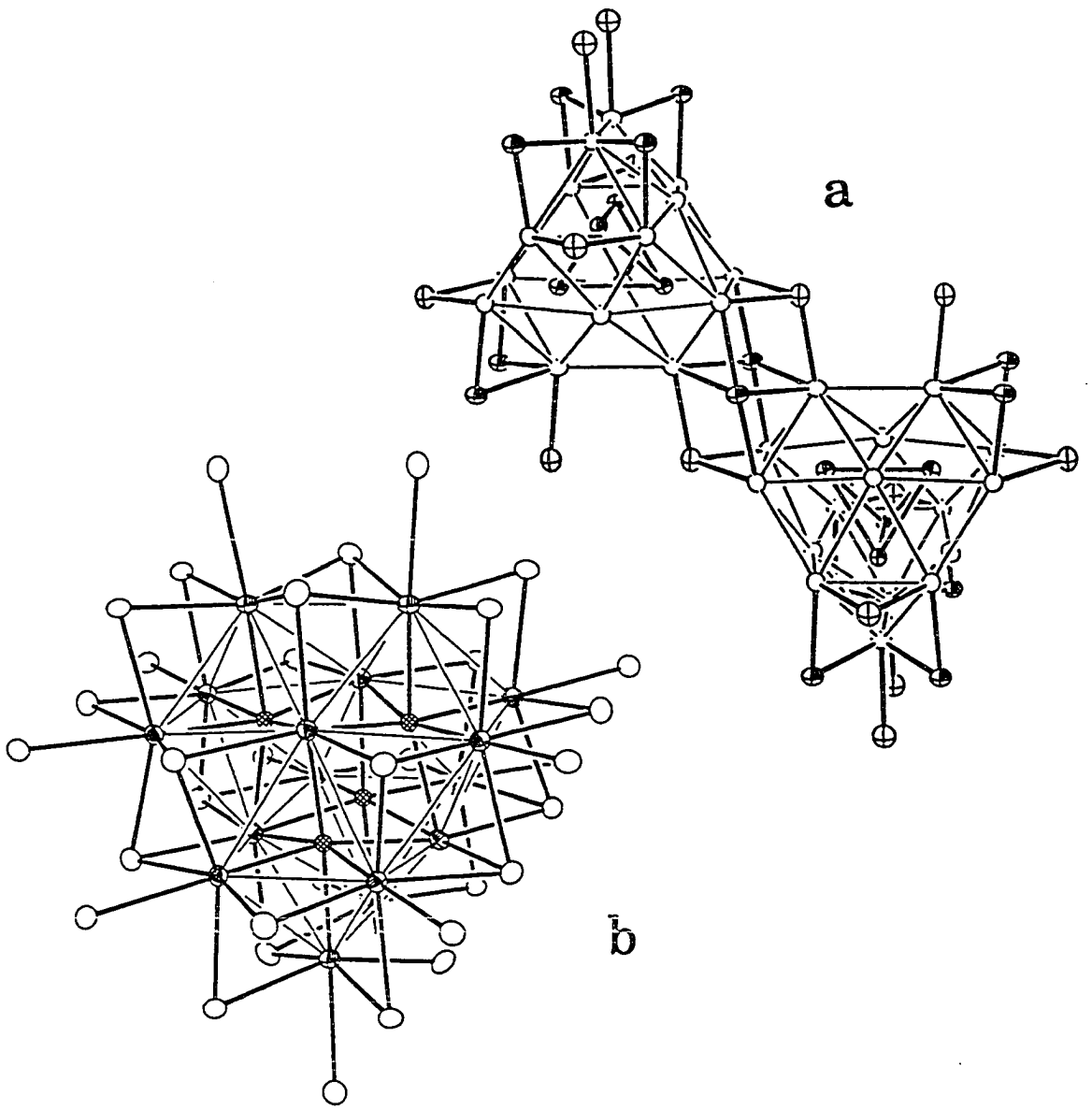

Figure 3. a) [110] view showing the bonding modes of Br2 (crossed) and Br4 (quarter-shaded) atoms, 70% ellipsoids. b) $Y_{16}Ru_4$ cluster with its 36 atom coordination sphere. Br (open), Y (quarter-shaded), Ru (cross-hatched). $\vec{c}$ is vertical in both pictures.

and away from the halides. In all cases, the Y-Br distances *trans* to a Ru atom within a given "octahedron" are considerably longer than the Y-Br distances in the other positions. This trend is consistent with observations in other rare-earth metal halide clusters,[15] where the interstitial atom appears to be "winning" over the opposing halide atom. In fact, four of the five longest Y-Br distances observed are *trans* to a Ru atom.

The Br and Ru atoms together may be viewed as forming roughly cubic-close-packed layers, shown in Figure 4, which lie parallel to $(2\bar{2}3)$, $(2\bar{2}\bar{3})$, $(\bar{2}\bar{2}3)$ and $(\bar{2}\bar{2}\bar{3})$. The Y atoms fill pseudo-octahedral holes around groups of Ru atoms, resulting in coordination by six heteroatoms. The layers stack imperfectly in an ..ABC.. manner. Figure 5 (compare to Figure 3b) reveals that near the oligomers, the Y layers are offset slightly toward the Ru positions which themselves are shifted out of the Br layer. This feature does not correspond to a large change in Y-Br distances between layers; the Br atoms are displaced accordingly within the layers. Yet, a small increase in distances is observed between the Br and Y layers directly above the hexagonal face of the oligomer, corresponding to the presence of a larger number of halides in a position *trans* to Ru atoms. The close-packing of halide atoms is a regular feature of metal halide structural chemistry, and again indicates the importance of metal-halide interactions in these structures.

Each oligomer is surrounded by twelve others and is connected to eight of these adjoining oligomers through two types of Br bridges. The first of these

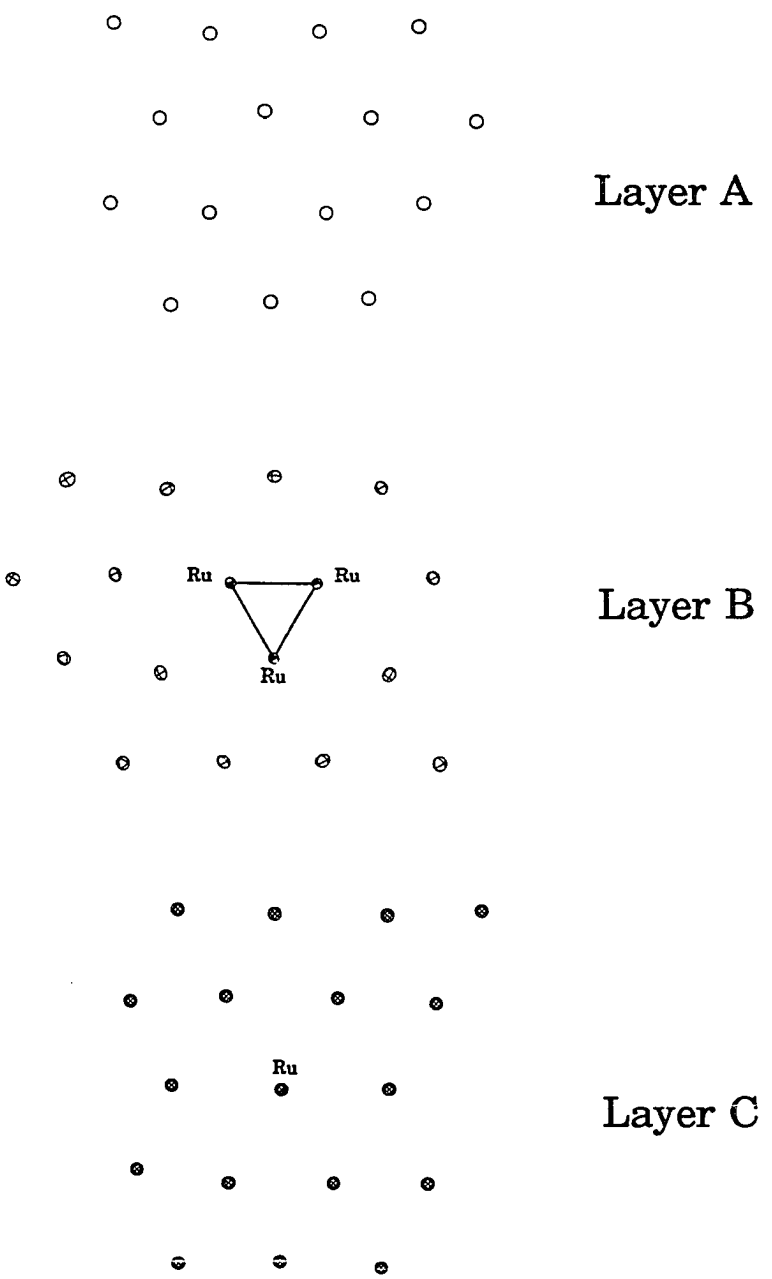

Figure 4. [$\overline{223}$] view of nearly cubic close-packed layers of Br and Ru atoms. Y atoms occupy pseudo-octahedral holes around the Ru positions.

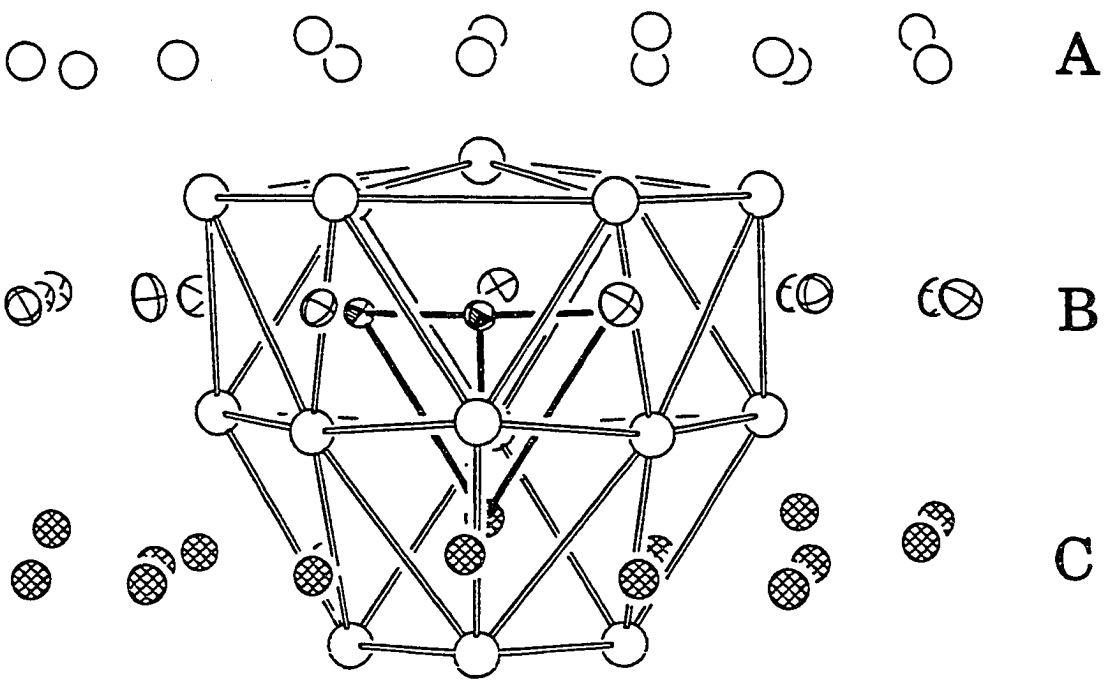

Figure 5. A $Y_{16}Ru_4$ cluster and nearby bromine atoms viewed parallel to the close-packed layers.

bridges, pictured in Figure 6a, joins each oligomer to four other oligomers within the a-b plane via $Br1^{i-a}$ and $Br1^{a-i}$ connections forming a square network at z=1/4. The smallest intercluster Y-Y distances in this plane are 4.72 Å and 4.79 Å along the a- and b-axes between Y3 atoms. Each cluster is related to the next by a unit cell translation of ±a and ±b and is in an equivalent orientation. A second layer at z=3/4 fits directly above the holes of the first layer (±a/2, ±b,2), resulting in an ...AB... stacking pattern. The second bridge is via $Br4^{i-i}$, $Br2^{i-a}$ and $Br2^{a-i}$ connections, shown in Figure 6b. Each cluster is bridged to four neighbors from the adjacent layers forming a pseudo-tetrahedral array. These clusters are related by an n-glide and differ in orientation from the central cluster by a 90° rotation around the c-axis, bringing the Y3-Y1-Y3 triangles face to face with each other. Intercluster Y-Y distances are 4.57 Å between Y1 atoms and 4.61 Å between Y1 and Y3 atoms. Four other clusters not connected via halide bridges form a second pseudo-tetrahedron, oriented such that Y hexagons are face to face. The shortest Y-Y distances between these clusters are over 6.5 Å. Accordingly, each cluster sits in an approximately cuboctahedral environment, with eight near-neighbor clusters and four more distant neighboring clusters.

Magnetic susceptibility measurements

Based on the formula, each $Y_{16}Ru_4$ cluster has 60 electrons available for metal-metal bonding. Extended Hückel calculations indicated that $Y_{16}I_{20}Ru_4$ has a closed-shell configuration with a calculated band gap of 0.3 eV.[62] A similar

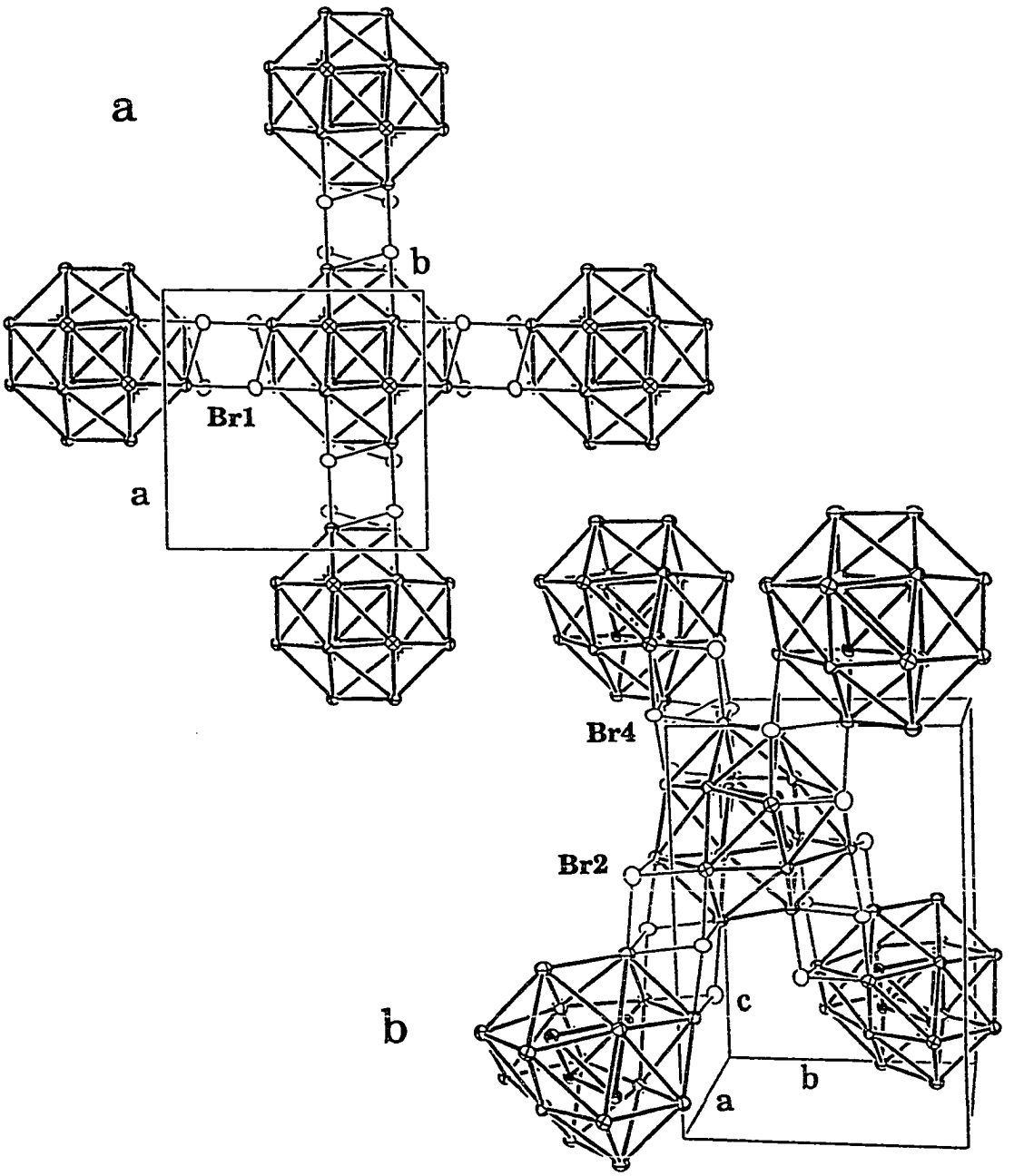

Figure 6. Intercluster bonding a) via Br1 atoms to form a square network within the a-b plane and b) via Br2 and Br4 atoms resulting in a pseudo-tetrahedral arrangement of bridged clusters.

bonding scheme was expected for $Y_{16}Br_{20}Ru_4$. To confirm this, magnetic susceptibility measurements were performed on a powdered sample of $Y_{16}Br_{20}Ru_4$ obtained by separation of a reaction product based on visual inspection. The data, presented in Figure 7, exhibit nearly T-independent paramagnetism at high temperatures, with a supposed Curie tail at T<60 K. The molar susceptibility at 300 K is 8.54 x 10^{-3} emu/mol. Although the compound might be expected to exhibit diamagnetism, the observed temperature-independent behavior is not inconsistent with a closed-shell configuration. Other metal halide cluster compounds have also exhibited temperature-independent paramagnetic behavior.[90] This has been attributed to intrinsic van Vleck paramagnetism,[91] arising from interactions between ground and excited-state functions in the presence of a magnetic field. The tail at low temperature may be due to a paramagnetic impurity. In addition to $Y_{16}Br_{20}Ru_4$, the sample contained small amounts of $AlBr_3$ (~15 mg. was added to the reaction to enhance crystal growth), YBr_3, and "Y_5Br_9Ru", the latter two phases identified by the weak presence of their strongest line in the powder pattern (~5%). It is possible that small amounts of other impurities were also present, giving rise to the observed low-temperature behavior.

$Y_{16}Br_{24}Ir_4$

$Y_{16}Br_{24}Ir_4$ is the second known example of a reduced rare-earth metal halide built up of isolated $RE_{16}Z_4$ cluster units sheathed by halogen atoms. The compound exhibits a new structure type, which is related to the structures of

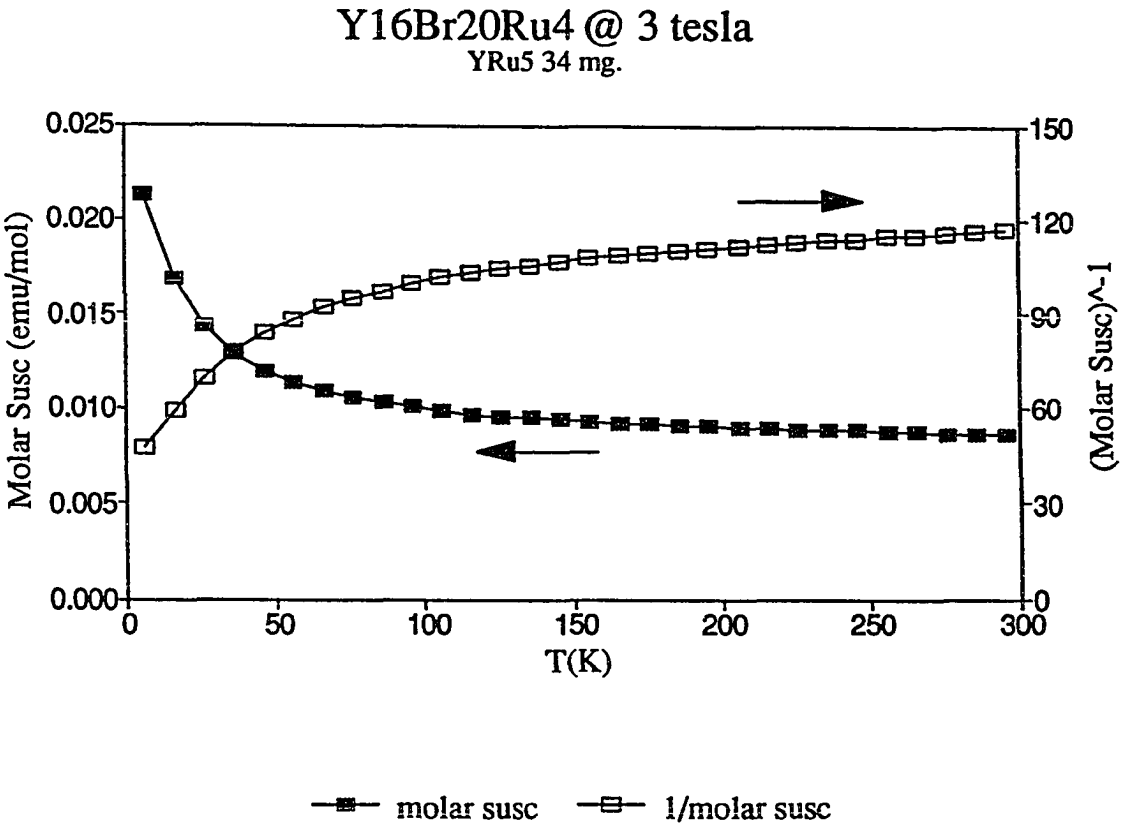

Figure 7. A plot of the magnetic susceptibility as a function of temperature for $Y_{16}Br_{20}Ru_4$ at 3 T.

$Y_{16}Br_{20}Ru_4$ and the analogous iodide. Formation of this new structure can be understood as a response to the replacement of the Ru by Ir in the $Y_{16}Z_4$ unit and the resulting electronic differences, which are accommodated by four new Br atoms and a new structure type. With the discovery of this phase, in addition to the aforementioned $Y_{16}Br_{20}Ru_4$ and the related $Gd_{20}I_{28}Mn_4$,[63] the $RE_{16}Z_4$ cluster has been established as a new building-block in reduced rare-earth metal halide structural chemistry. The novel oligomeric nature of the cluster provides an alternative mode of cluster condensation to those previously seen, e.g. infinite chains, double-chains, or three-dimensional networks.

Synthesis

$Y_{16}Br_{24}Ir_4$ was first observed in a reaction between YBr_3, CsBr, Y foil, and Ir powder loaded with the composition $CsY_6Br_{11}Ir$, in an attempt to either incorporate Cs into a cluster phase or enhance crystal growth of $Y_{16}Br_{24}Ir_4$. The reaction was heated quickly to 750°C, allowed to react for four days, then ramped slowly (+5°/hr) to 850°C. After another four day reaction period at this temperature, the reaction was again ramped (+3°/hr) to 950°C, where it was held constant for two weeks before cooling slowly (-5°/hr) to 700°C and then quenched. The reaction product consisted of ~50% $Y_{16}Br_{24}Ir_4$ as agglomerates of black brittle crystals and chunks grown in and around a mixture of plate-like YBr_3 (~10%), YOBr (~15%), and $Cs_3Y_2Br_9$ (~25%); the Cs was incorporated into the ternary phase, leaving the remaining material with a composition slightly Ir-deficient for producing $Y_{16}Br_{24}Ir_4$. A reaction with a similar composition,

$CsY_6Br_{10}Ir$, was heated even more slowly (over a period of 15 days) to 950°C, followed by a 14 day reaction period. In this case, $Y_{20}Br_{36}Ir_4$ (discussed in the next section) was observed (~20% yield) in addition to the phases mentioned above; the products seem to be dependent not only on temperature but on reaction time as well. Increasing the amount of Cs to the composition $Cs_3Y_6Br_{10}Ir$ forestalled formation of any cluster phase, and instead yielded both $Cs_3Y_2Br_9$ and CsBr in addition to Y_3Ir, YOBr, and a trace amount of YBr_3.

The phase $Y_{16}Br_{24}Ir_4$ was also synthesized in analogous reactions containing Rb and K. The reactions, loaded as $RbY_6Br_{10}Ir$ and $KY_6Br_{10}Ir$, were heated slowly (as in the first reaction mentioned) to 900°C and held there for five weeks. The reaction products consisted of the cluster phases $Y_{16}Br_{24}Ir_4$ and $Y_6Br_{10}Ir$, along with Y_5Ir_2, YOBr, YBr_3, and weak lines tentatively assigned to $Rb_3Y_2Br_9$ and K_3YBr_6, respectively.

The phase was observed only in reactions that contained alkali metals; the alkali-metal halide reacted with YBr_3 to form a ternary halide, which presumably acted as a flux and promoted growth of $Y_{16}Br_{24}Ir_4$. Reactions loaded without alkali-metal halides over a wide range of M:Br ratios both larger and smaller than 2:3 yielded instead the phase $Y_{20}Br_{36}Ir_4$ or other products. Based on the results of a single crystal X-ray diffraction study, there is no evidence that the alkali metals were incorporated into the phase. The relatively low yields of the reactions were largely due to the reactivity of the alkali metals with the other reactants, which consumed much of the YBr_3 and altered the

stoichiometry of the remaining components. It would be interesting to attempt the synthesis of the phase in the presence of a different flux, perhaps an alkaline-earth metal halide, that would be less reactive to the other components of the system. If a suitable flux were found, the synthesis should result in higher yields of the phase.

Structure determination

The crystal used for the structural determination was from the reaction loaded as $CsY_6Br_{11}Ir$. The black crystal was block-shaped with irregular surfaces, having been cut out of a larger aggregate of crystals. A Laue photo of the crystal suggested a rather large unit cell and indicated that the crystal quality was adequate for further study. A preliminary peak search procedure on a Rigaku automated diffractometer found 15 peaks that indexed to an F-centered orthorhombic cell with lengths of 11.72 Å, 22.39 Å, and 44.69 Å. At a later date, a second peak search on the same crystal located 27 peaks with an average intensity of ~3200 counts, 25 of which indexed to a primitive orthorhombic cell with 11.17 Å, 22.30 Å, and 5.84 Å. Axial photos confirmed the presence of three mirror planes, but indicated that all three cell lengths were double these values. After transforming the cell to the larger values, the diffractometer software yielded a primitive orthorhombic unit cell matching those found originally. An initial data collection of 360 reflections using an omega scan mode uncovered several observed reflections unique to a primitive cell (h+k=2n+1, h+l=2n+1, k+l=2n+1 were observed), but closer examination

revealed that most had very asymmetrical backgrounds. In addition, these violations to F-centering were adjacent to stronger reflections allowed by F-centering. Several reflections unique to the primitive cell were scanned and found to be simply mis-indexed, i.e. the scanning range for neighboring peaks overlapped due to the large size of the c-axis. The omega scan width had been determined based on the peak shape from the search procedure, and could not be narrowed further without risking loss of peak intensity. Based on these considerations, no violations to the F-centered cell could be confirmed, and subsequently, a quadrant (±h,k,l) of data was collected on the F-centered cell to a maximum 2θ of 50°. Due to the relatively weak scattering power of the crystal, a scan speed of 8°/min. was employed. Following data collection, three psi scan measurements were performed, which exhibited a significant transmission range of 0.342-1.000.

After data reduction, including Lorentz-polarization corrections followed by an empirical absorption correction based on the averaged transmission curve, the data were examined for possible extinction conditions. Intensity standards indicated that no decay correction was necessary, and the p-factor (fudge factor) was calculated and reset to 0.002. In addition to the reflection conditions required by F-centering, the data exhibited extinction conditions for reflections of the type 0kl:k+l≠2n, h0l:h+l≠2n, hk0:h+k≠2n, h00:h≠4n, 0k0:k≠4n, 00l:l≠4n. Fourteen violations to hk0, h0l, and 0kl conditions were observed, but were ignored at this point. Intensity data strongly indicated the presence of a center

of symmetry. These conditions are unique to the space group Fddd, which was used for the structure solution.

After several trial models, provided by SHELXS-86, a solution was obtained in which eleven atoms formed $Y_{16}Ir_4$ cluster units and accompanying Br atoms. The identities of the peaks were clearly defined by geometry, peak height, bond distances and coordination environments. A sharp dropoff in peak height separated the eleven atoms from the remaining peaks in the solution. Refinement of the positional parameters and scale factor, then isotropic thermal parameters yielded an R=0.076 and R_w=0.092. The B-values were very small for the atoms, and were negative for the Ir and one Y, until after refinement of a secondary extinction coefficient. Upon anisotropic refinement of the thermal parameters, the ellipsoids of several atoms were not positive-definite. Even after a second absorption correction with the DIFABS program, four atoms were still not positive-definite. ORTEP drawings of the other atoms indicated a large anisotropic character in the x-y plane. One possible explanation for these problems was incorrect space group assignment. Lowering the symmetry to space groups Fdd2 and F222 resulted in major correlation problems between the fractional coordinates and thermal parameters of atoms equivalent in Fddd. Two possible alternate cells were identified, both corresponding to C-centered monoclinic space groups. Attempts at refinement in these cells in space group $C2_1/c$ resulted in similar R-values (~7%), but did not eliminate the problems with thermal parameters.

Weissenberg photos of the crystal were taken for the h0l, h1l, and h2l layers, to help determine the space group. The h0l layer confirmed the cell dimensions and exhibited extinctions for h+l=2n. Also, a significant number of streaked spots were observed, which formed portions of a net not corresponding to the aligned crystal. This indicated the presence of a satellite on the major crystal which could have been responsible for the 14 observed violations to Fddd. The h1l and h2l photos were much "cleaner", and were consistent with an F-centered cell. Two weak "violations" were observed in the h1l photo, but the symmetry equivalent reflections were not present. The conclusion reached was that the initial F-centered space group was still the best choice.

An alternative cause for the refinement problems in Fddd was thought to be a systematic error in the observed structure factors. Although the presence of a satellite crystal could result in some interference with the data, it seemed unlikely that it would result in the large systematic errors suggested by the thermal parameters. A more likely reason was that absorption by the crystal had not been adequately accounted for. To better estimate the absorption, the ABSN93 program[93] was employed, followed by data reduction with the CHES structural solution package.[93] The main advantage of ABSN93 was that it incorporated information regarding the size, shape, and absorption coefficient of the crystal to apply a 2θ-dependent spherical correction to the data, and this was then modified according to the psi-scan measurements. Data collection and refinement information is listed in Table 6. Refinement of positional and

Table 6. Crystallographic data for $Y_{16}Br_{24}Ir_4$

Crystal data	
Formula	Y_4Br_6Ir
Space group, Z	Fddd, 32
a (Å)[a]	11.718(3)
b (Å)	22.361(7)
c (Å)	44.702(17)
V (Å^3)	11,713(11)
D_{calc} (g/cm^3)	4.660
μ (Mo Kα, cm^{-1})	409.95
Data collection	
Crystal dimensions, mm	0.16 x 0.20 x 0.28
Diffractometer	Rigaku AFC6R
Radiation, wavelength (Å)	Mo Kα, 0.71069
Scan mode	ω
Octant measured	±h, k, l
$2\theta_{max}$, deg.	50
Refinement	
No. of measured reflections	6334
No. of independent reflections	3092
No. of indep. reflections ($I \geq 3\sigma_I$)	1180
No. of variables	101
Transmission coefficient range	0.510 – 1.162
Secondary extinction coefficient	3.3(3) x 10^{-10}
R_{avg} ($I \geq 0$, $I \geq 3\sigma_I$)	0.178, 0.058
R, R_w	0.0574, 0.0553
Largest residual peak, e/Å^3	2.23 (1.75 Å from Br1), -2.01

[a] Guinier cell constants from 27 lines.

isotropic thermal parameters with this absorption-corrected data set yielded R-values of 0.0838 and R_w of 0.0836, along with much larger B-values for the atoms. The thermal parameters were refined anisotropically, with heavy damping, until convergence at R=0.0689 and R_w=0.0739. No problems with the anisotropic values were evident in the model. The difference Fourier calculation revealed the presence of several peaks, the largest with a value of 3.82 e/Å^3, that appeared to ring the Ir atom. Refinement after application of a DIFABS absorption correction yielded a difference map that showed no evidence of these peaks, and resulted in an R-value of 0.0628 and an R_w of 0.0637. Of the 1182 unique reflections, 17 had observed structure factors that deviated from those calculated for the model by more than $5\sigma_F$. Many of these were of the 0kl type, two of which had F_{obs} that were particularly large relative to F_{calc} and could have resulted from the satellite crystal. Removal of these two reflections caused a decrease in the R to 5.75% and R_w to 5.53%. The largest positive and negative peaks in the final difference Fourier map were 2.24 e/Å^3, located 1.75 Å from Br1, and -2.02 e/Å^3. Positional parameters and anisotropic thermal parameters are listed in Tables 7 and 8.

The powder pattern calculated from the structure model agrees very well with the observed powder pattern. The phase exhibits three strong low-angle lines, two of which are nearly overlapping. Only a few other lines (~6) exhibit intensities larger than ~10% of the strongest line, while many weak lines are present. Lattice parameters were calculated based on 27 lines measured in a

Table 7. Positional and equivalent isotropic thermal parameters for $Y_{16}Br_{24}Ir_4$

Atom	Type	x	y	z	B_{eq}
Ir	32h	0.0238(2)	0.0728(1)	0.09899(5)	1.40(7)
Y1	32h	0.0073(4)	0.0677(3)	0.0372(1)	2.1(2)
Y2	32h	0.0086(4)	-0.0536(2)	0.8389(1)	1.8(2)
Y3	32h	0.0423(4)	-0.0656(2)	0.3444(1)	1.8(2)
Y4	32h	0.0092(4)	-0.0497(2)	0.0952(1)	1.6(2)
Br1	32h	0.0032(4)	-0.0809(2)	0.1579(1)	2.1(2)
Br2	32h	0.0028(4)	0.0592(2)	0.2273(1)	2.0(2)
Br3	32h	0.0245(4)	0.0581(2)	0.5930(1)	2.1(2)
Br4	32h	0.0156(5)	0.0635(3)	0.3433(2)	2.6(3)
Br5	32h	0.0071(5)	-0.0613(2)	0.0307(2)	2.4(3)
Br6	32h	0.0177(5)	-0.0694(3)	0.2823(2)	2.8(2)

Table 8. Anisotropic thermal parameters for $Y_{16}Br_{24}Ir_4$

Atom	U_{11}	U_{22}	U_{33}	U_{12}	U_{13}	U_{23}
Ir	0.0186(9)	0.017(1)	0.017(1)	-0.0009(9)	-0.001(1)	-0.001(1)
Y1	0.028(3)	0.026(3)	0.025(3)	-0.002(2)	0.001(2)	-0.002(2)
Y2	0.022(3)	0.021(3)	0.024(3)	0.001(2)	-0.001(2)	-0.002(2)
Y3	0.022(2)	0.021(3)	0.024(3)	-0.002(2)	-0.002(2)	0.002(2)
Y4	0.021(2)	0.020(3)	0.021(3)	-0.001(2)	-0.000(2)	-0.001(2)
Br1	0.025(3)	0.028(3)	0.028(3)	-0.002(2)	-0.001(2)	0.001(2)
Br2	0.026(3)	0.026(3)	0.024(3)	0.000(2)	0.000(2)	0.000(2)
Br3	0.025(3)	0.027(3)	0.029(4)	0.001(2)	0.001(3)	-0.000(2)
Br4	0.027(3)	0.025(3)	0.045(4)	0.001(2)	-0.000(3)	0.003(3)
Br5	0.046(3)	0.021(3)	0.022(3)	-0.004(2)	0.003(3)	0.001(3)
Br6	0.026(2)	0.055(4)	0.026(3)	-0.001(3)	0.001(2)	0.003(3)

multi-phase Guinier powder pattern.

Structural description

$Y_{16}Br_{24}Ir_4$ is built of $Y_{16}Ir_4$ oligomeric clusters similar to those observed in $Y_{16}Br_{20}Ru_4$ and $Y_{16}I_{20}Ru_4$. The clusters are isolated from each other by Br atoms, which sheath each cluster unit. A major difference between this structure and that of $Y_{16}Br_{20}Ru_4$ is the manner of Br connectivity around and between cluster units. This change is a logical result of the replacement of Ru by Ir, which increases the number of available electrons by a total of four per cluster. This new structure maintains a local environment around each cluster similar to that seen in $Y_{16}Br_{20}Ru_4$, but the Br atoms are shared in a manner that results in the addition of four more Br atoms per cluster. This change nicely accommodates the four extra electrons, leaving 60 electrons for cluster bonding and resulting in a formula of $Y_{16}Br_{24}Ir_4$.

The orthorhombic unit cell of $Y_{16}Br_{24}Ir_4$ is face-centered and contains a total of eight $Y_{16}Ir_4$ cluster units, which are shown in Figure 8. These clusters can be described as distorted tetra-capped truncated tetrahedra of Y atoms enclosing an Ir tetrahedron. Alternatively, the clusters can be viewed as oligomers created upon pairwise condensation of edge-sharing Y_6Ir octahedra. The clusters are centered around (1/8, 1/8, 1/8), (7/8, 7/8, 7/8), and the corresponding (F-centered) symmetry-related sites, and exhibit 222 (D_2) symmetry. This is a much lower symmetry than was observed in $Y_{16}Br_{20}Ru_4$ ($\bar{4}2m$). Accordingly, the cluster contains four crystallographically distinct types of Y

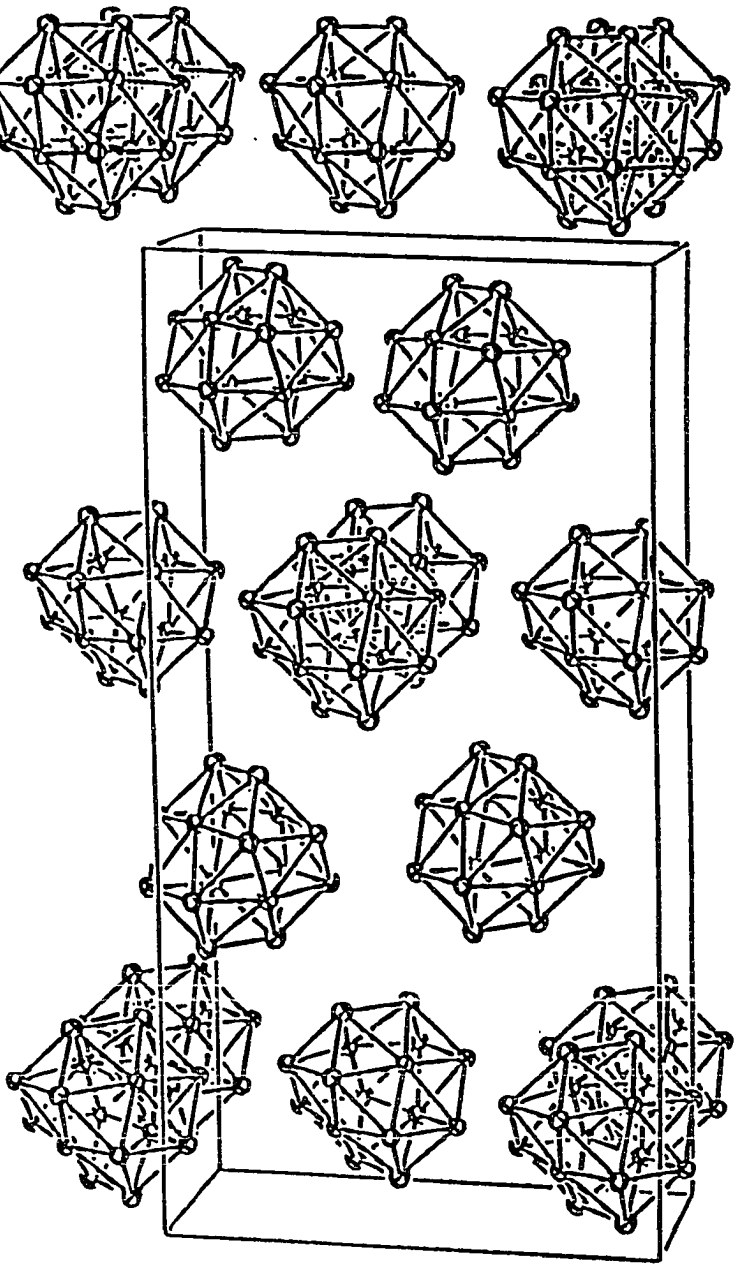

Figure 8. [$\bar{1}$00] view of the unit cell of $Y_{16}Br_{24}Ir_4$ illustrating the face-centered nature of the cluster packing; $\vec{b}$ is horizontal, $\vec{c}$ is vertical. Each unit cell contains a total of eight $Y_{16}Ir_4$ clusters. Br atoms are omitted for clarity.

atoms, as seen in Figure 9. The truncated tetrahedron is formed by Y1, Y3, and Y4 atoms, which correspond to Y1 and Y3 in $Y_{16}Br_{20}Ru_4$; Y3 and Y4 are symmetry-equivalent in the $Y_{16}Ru_4$ clusters. The pseudo-hexagonal faces are capped by Y2 atoms, as in $Y_{16}Br_{20}Ru_4$. Three mutually-perpendicular 2-fold axes intersect at the cluster center. One 2-fold axis, parallel to the a-axis, passes through the center of the two Y3-Y3 edges. The second 2-fold axis runs parallel to $\vec{b}$ and bisects the two Y4-Y4 edges. The third 2-fold axis, parallel to $\vec{c}$, passes through the center of the two Y1-Y1 edges. The lack of mirror symmetry is evident in the bond distances and angles, presented in Tables 9, 10, and 11. The Y1-Y3 and Y1-Y4 bond lengths differ by 0.10(1) Å, and Y2-Y1 distances (also equivalent in $Y_{16}Br_{20}Ru_4$) differ by 0.060(8) Å. The lower symmetry is present in the Ir "tetrahedron" as well; the Ir-Ir distances range from 3.294(4) Å to 3.328(4) Å. The shortest Ir-Ir distances are parallel to the two Y3-Y3 edges, which are also the nearest Y atoms, while the longest coincide with the two Y1-Y1 edges.

Most bond distances within the $Y_{16}Ir_4$ clusters are slightly larger on average than those found for the $Y_{16}Ru_4$ clusters in $Y_{16}Br_{20}Ru_4$, but are still smaller than were observed in $Y_{16}I_{20}Ru_4$. Generally, the Y-Y bond distances in $Y_{16}Br_{24}Ir_4$ are larger than seen in the Ru phase by a few hundredths of an Å or more, resulting in an average Y-Y distance of 3.72 Å in the former (Pauling bond order is 0.15) compared to 3.69 Å in the latter. The average Y-Y distances involving the five-coordinate Y1, Y3, and Y4 atoms are very similar to each

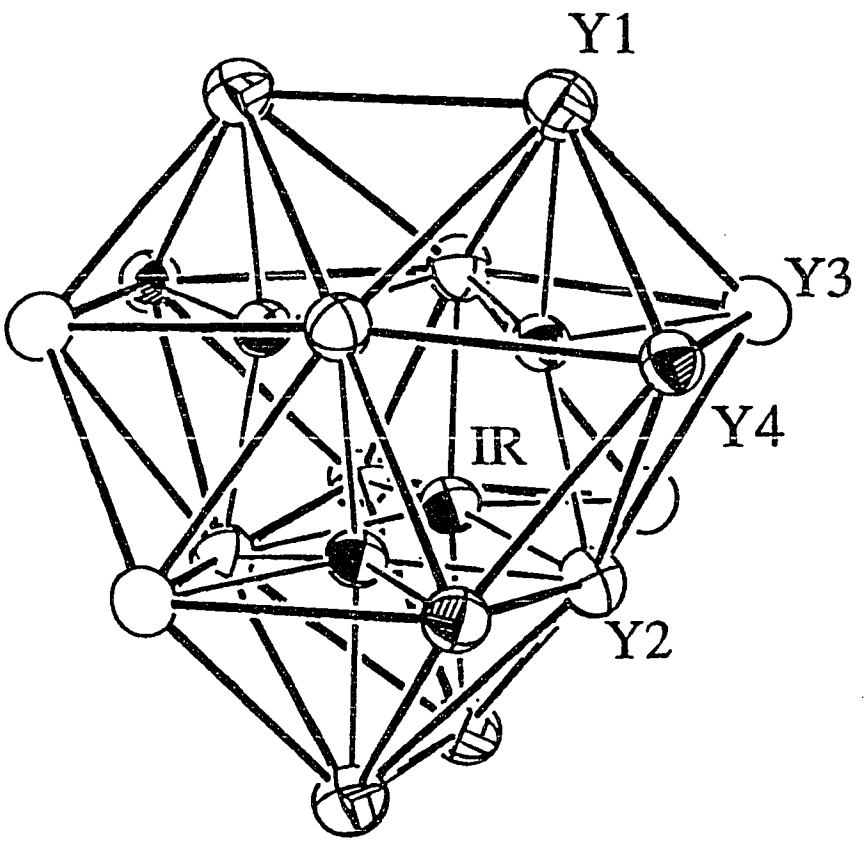

Figure 9. [110] view of a $Y_{16}Ir_4$ cluster unit; $\vec{c}$ is vertical. The cluster exhibits 222 (D_2) symmetry and can be viewed as an oligomer of distorted Y_6Ir octahedra.

Table 9. Bond distances in $Y_{16}Br_{24}Ir_4$

Ir–Ir	3.294(4)	Y2–Y1	3.757(7)	Y3–Ir	2.724(5)	Br1–Y2[b]	3.013(8)
Ir–Ir	3.322(4)	Y2–Y1	3.697(8)	Y3–Br3[b]	3.144(7)	Br1–Y4	2.890(9)
Ir–Ir	3.328(4)	Y2–Y2[a]	4.49(1)	Y3–Br3	2.932(7)	Br1–Y4	2.874(7)
Ir–Y1	2.771(7)	Y2–Y2[a]	4.47(1)	Y3–Br3	2.909(8)	Br2–Y1	2.828(8)
Ir–Y2	2.825(6)	Y2–Y2[a]	4.54(1)	Y3–Br4	2.903(9)	Br2–Y1	2.891(7)
Ir–Y2	2.821(6)	Y2–Y3	3.749(7)	Y3–Br6	2.79(1)	Br2–Y2[b]	2.966(9)
Ir–Y2	2.833(7)	Y2–Y3	3.793(8)	$\bar{d}_{Y3\text{-}Br}$	2.93	Br3–Y2[b]	3.122(7)
Ir–Y3	2.724(5)	Y2–Y4	3.735(7)	Y4–Y1	3.689(8)	Br3–Y3[b]	3.144(7)
Ir–Y4	2.750(6)	Y2–Y4	3.749(8)	Y4–Y2	3.735(7)	Br3–Y3	2.932(7)
$\bar{d}_{Ir\text{-}Y}$	2.787	$\bar{d}_{Y2\text{-}Y}$[a]	3.747	Y4–Y2	3.749(8)	Br3–Y3	2.909(8)
Y1–Y1	3.76(1)	Y2–Ir	2.825(6)	Y4–Y3	3.620(7)	Br4–Y3	2.903(9)
Y1–Y2	3.757(7)	Y2–Ir	2.821(6)	Y4–Y4	3.81(1)	Br4–Y4	2.873(8)
Y1–Y2	3.697(8)	Y2–Ir	2.833(7)	$\bar{d}_{Y4\text{-}Y}$	3.71	Br4–Y4[b]	3.075(8)
Y1–Y3	3.590(7)	Y2–Br1[b]	3.013(8)	Y4–Ir	2.750(6)	Br5–Y1	2.901(9)
Y1–Y4	3.689(8)	Y2–Br2[b]	2.966(9)	Y4–Br1	2.890(9)	Br5–Y1[b]	3.04(1)
$\bar{d}_{Y1\text{-}Y}$	3.69	Y2–Br3[b]	3.122(7)	Y4–Br1	2.874(7)	Br5–Y4	2.90(1)
Y1–Ir	2.771(7)	$\bar{d}_{Y2\text{-}Br}$	3.03	Y4–Br4	2.873(8)	Br6–Y1	2.817(8)
Y1–Br2	2.828(8)	Y3–Y1	3.590(7)	Y4–Br4[b]	3.075(8)	Br6–Y3	2.79(1)
Y1–Br2	2.891(7)	Y3–Y2	3.749(7)	Y4–Br5	2.90(1)	Br1-Br1	3.59(1)
Y1–Br5	2.901(9)	Y3–Y2	3.793(8)	$\bar{d}_{Y4\text{-}Br}$	2.92	Br-Br	≥3.70(1)
Y1–Br5[b]	3.04(1)	Y3–Y3	3.81(1)				
Y1–Br6	2.817(8)	Y3–Y4	3.620(7)			$\bar{d}_{Y\text{-}Br}$	2.937
$\bar{d}_{Y1\text{-}Br}$	2.90	$\bar{d}_{Y3\text{-}Y}$	3.70			$\bar{d}_{Y\text{-}Y}$[a]	3.721

a non-bonding distances not included in averaging
b corresponds to a Br atom *trans* to Ru

Table 10. Important intracluster bond angles in $Y_{16}Br_{24}Ir_4$

Ir	Ir	Ir	59.39(7)	Y1	Y1	Y2	58.9(1)	Y3	Y2	Y4	57.4(1)
Ir	Ir	Ir	60.23(7)	Y1	Y1	Y3	121.5(2)	Y4	Y2	Y4	61.1(2)
Ir	Ir	Ir	60.38(8)	Y1	Y1	Y4	118.7(2)	Y1	Y3	Y2	60.4(2)
Ir	Ir	Y1	91.30(9)	Y2	Y1	Y2	73.7(2)	Y1	Y3	Y2	97.4(2)
Ir	Ir	Y1	94.5(1)	Y2	Y1	Y3	61.9(1)	Y1	Y3	Y3	120.1(2)
Ir	Ir	Y2	102.7(1)	Y2	Y1	Y4	96.6(2)	Y1	Y3	Y4	61.5(2)
Ir	Ir	Y2	101.6(1)	Y2	Y1	Y3	96.3(2)	Y2	Y3	Y2	74.0(2)
Y1	Ir	Y2	82.7(2)	Y2	Y1	Y4	60.2(1)	Y2	Y3	Y3	60.2(1)
Y1	Ir	Y2	84.4(2)	Y3	Y1	Y4	59.6(2)	Y2	Y3	Y4	96.8(2)
Y1	Ir	Y2	163.9(2)	Y1	Y2	Y1	60.6(2)	Y2	Y3	Y3	59.1(1)
Y1	Ir	Y3	81.6(2)	Y1	Y2	Y3	117.5(2)	Y2	Y3	Y4	60.7(1)
Y1	Ir	Y4	83.8(2)	Y1	Y2	Y3	163.6(2)	Y3	Y3	Y4	119.3(2)
Y2	Ir	Y2	104.8(2)	Y1	Y2	Y4	59.0(1)	Y1	Y4	Y2	60.8(1)
Y2	Ir	Y2	106.6(2)	Y1	Y2	Y4	119.5(2)	Y1	Y4	Y2	96.5(2)
Y2	Ir	Y3	85.0(2)	Y1	Y2	Y3	57.7(1)	Y1	Y4	Y3	58.8(1)
Y2	Ir	Y4	163.0(2)	Y1	Y2	Y3	117.9(2)	Y1	Y4	Y4	119.8(2)
Y2	Ir	Y2	105.3(2)	Y1	Y2	Y4	119.2(2)	Y2	Y4	Y2	73.8(2)
Y2	Ir	Y3	161.8(2)	Y1	Y2	Y4	165.6(2)	Y2	Y4	Y3	96.2(2)
Y2	Ir	Y4	84.2(2)	Y3	Y2	Y3	60.7(2)	Y2	Y4	Y4	59.6(1)
Y2	Ir	Y3	86.1(2)	Y3	Y2	Y4	164.7(2)	Y2	Y4	Y3	61.9(1)
Y2	Ir	Y4	84.3(2)	Y3	Y2	Y4	117.6(2)	Y2	Y4	Y4	59.3(1)
Y3	Ir	Y4	82.8(2)	Y3	Y2	Y4	117.8(2)	Y3	Y4	Y4	120.5(2)
Y1	Y1	Y2	60.5(1)								

Table 11. Bond angles around Y and Br in $Y_{16}Br_{24}Ir_4$

Ir	Y1	Br2	100.9(2)	Br2	Y2	Br3	95.8(2)	Br1	Y4	Br4	81.3(2)
Ir	Y1	Br2	99.1(2)	Ir	Y3	Br3	176.8(3)	Br1	Y4	Br5	86.5(2)
Ir	Y1	Br5	98.1(2)	Ir	Y3	Br3	102.1(2)	Br4	Y4	Br4	78.4(2)
Ir	Y1	Br5	179.1(2)	Ir	Y3	Br3	101.5(2)	Br4	Y4	Br5	87.3(2)
Ir	Y1	Br6	98.4(3)	Ir	Y3	Br4	99.7(2)	Br4	Y4	Br5	83.3(2)
Br2	Y1	Br2	91.8(2)	Ir	Y3	Br6	100.1(2)	Y2	Br1	Y4	78.8(2)
Br2	Y1	Br5	160.9(3)	Br3	Y3	Br3	77.6(2)	Y2	Br1	Y4	78.7(2)
Br2	Y1	Br5	79.4(2)	Br3	Y3	Br3	75.4(2)	Y4	Br1	Y4	82.6(2)
Br2	Y1	Br6	87.1(2)	Br3	Y3	Br4	80.7(2)	Y1	Br2	Y1	82.3(2)
Br2	Y1	Br5	85.0(2)	Br3	Y3	Br6	83.0(2)	Y1	Br2	Y2	79.2(2)
Br2	Y1	Br5	80.1(2)	Br3	Y3	Br3	90.2(2)	Y1	Br2	Y2	79.8(2)
Br2	Y1	Br6	162.3(3)	Br3	Y3	Br4	158.2(2)	Y2	Br3	Y3	76.5(2)
Br5	Y1	Br5	81.5(2)	Br3	Y3	Br6	85.5(2)	Y2	Br3	Y3[a]	177.5(3)
Br5	Y1	Br6	90.3(2)	Br3	Y3	Br4	86.0(2)	Y2	Br3	Y3	77.9(2)
Br5	Y1	Br6	82.4(2)	Br3	Y3	Br6	158.4(2)	Y3	Br3	Y3[a]	102.4(2)
Ir	Y2	Br1	95.7(2)	Br4	Y3	Br6	90.1(2)	Y3	Br3	Y3	81.5(2)
Ir	Y2	Br2	96.2(2)	Ir	Y4	Br1	100.5(2)	Y3	Br3	Y3[a]	104.3(2)
Ir	Y2	Br3	163.5(3)	Ir	Y4	Br1	100.6(2)	Y3	Br4	Y4[a]	177.4(3)
Ir	Y2	Br1	164.2(3)	Ir	Y4	Br4	99.8(2)	Y3	Br4	Y4	77.6(2)
Ir	Y2	Br2	96.4(2)	Ir	Y4	Br4	177.3(3)	Y4	Br4	Y4[a]	101.5(2)
Ir	Y2	Br3	95.3(2)	Ir	Y4	Br5	98.7(2)	Y1	Br5	Y1[a]	98.5(2)
Ir	Y2	Br1	95.7(2)	Br1	Y4	Br1	90.6(2)	Y1	Br5	Y4	79.1(2)
Ir	Y2	Br2	164.8(3)	Br1	Y4	Br4	88.7(2)	Y1	Br5	Y4[a]	176.3(3)
Ir	Y2	Br3	94.1(2)	Br1	Y4	Br4	77.5(2)	Y1	Br6	Y3	79.6(2)
Br1	Y2	Br2	95.0(2)	Br1	Y4	Br5	160.8(3)				
Br1	Y2	Br3	94.3(2)	Br1	Y4	Br4	159.3(3)				

a Intercluster bridging angle

other, as they were in $Y_{16}Br_{20}Ru_4$, consistent with their similar functionalities in the cluster. The unique functionality of the six-coordinate Y2 atoms results in a larger average Y2-Y bond length than Y1, Y3, or Y4, again as seen in the Ru compound. Notably, the Y2-Y2 (non-bonding) distances in the $Y_{16}Ir_4$ cluster are nearly 0.1 Å larger than in $Y_{16}Br_{20}Ru_4$. The average Y-Ir distance is slightly larger than the average Y-Ru distances in the Ru phase. This fact is consistent with the single bond radii tabulated by Pauling,[88] which predict an increase of ~0.02 Å upon substitution of Ru by Ir. Interestingly, the Ir-Ir distances are smaller than the Ru-Ru distances in $Y_{16}Br_{20}Ru_4$, yet the shortest Ir-Ir distance yields a Pauling bond order of 0.05, indicating the presence of only minimal Ir-Ir interactions. Evidently, the placement of the Ir atoms is dictated largely by optimization of Y-Ir bonding.

The Y_6Ir "octahedra" that make up the oligomeric $Y_{16}Ir_4$ clusters are very irregular, as all Y-Y and Y-Ir distances are symmetry-inequivalent. The Ir atoms are drawn out of the centers of the octahedra toward the center of the cluster even more so than the Ru atoms in $Y_{16}Br_{20}Ru_4$; *trans* angles across each octahedron (Y2-Ir-Y) range from 163.9° to 161.8°, compared to 165.5° and 164.2° in $Y_{16}Br_{20}Ru_4$ and 168.5° and 169.6° in the iodide phase. Yet each Ir atom is closer to the $\bar{Y}$ atoms in the $\bar{Y}1$-$\bar{Y}3$-$\bar{Y}4$ triangular face than to the three $\bar{Y}2$ atoms, due to the large size of Y2-Y2 distances.

The structure contains six crystallographically different types of Br atoms, which adopt four basic bonding modes. As shown in Figure 10, Br1, Br2, and

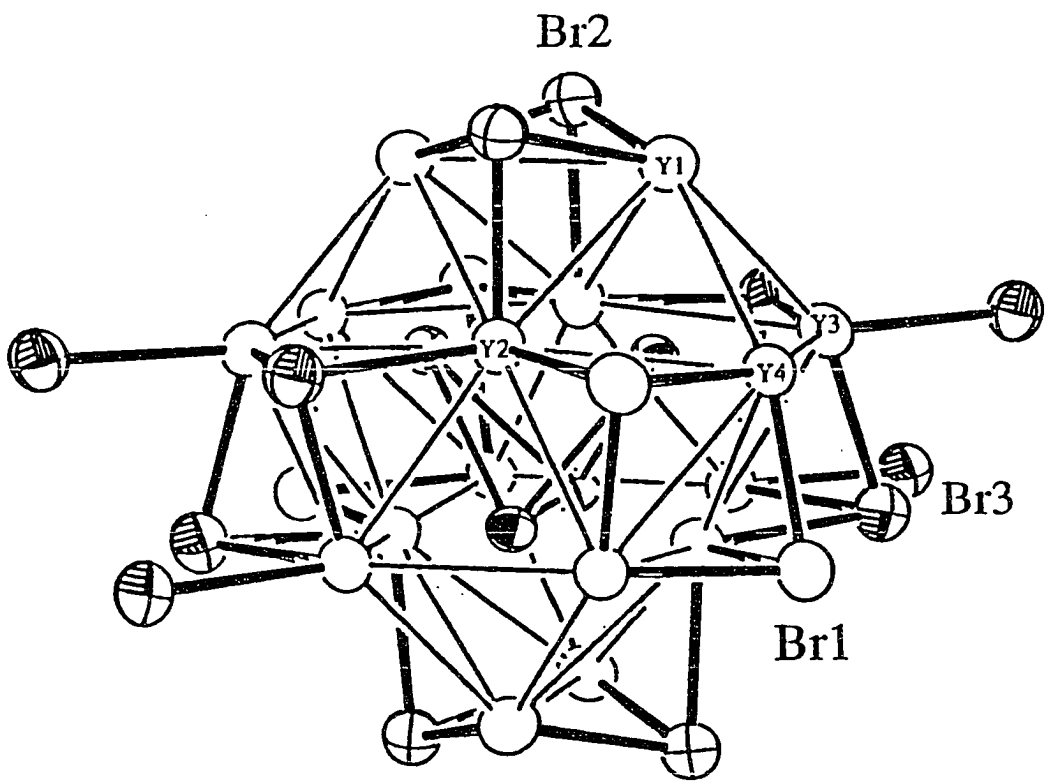

Figure 10. [110] view of the bonding modes adopted by Br1, Br2, and Br3 atoms; $\vec{c}$ is vertical. Br1 and Br2 cap triangular faces (Y2-Y4-Y4 and Y2-Y1-Y1, respectively) on only one cluster, while Br3 caps Y2-Y3-Y3 faces and occupies a site exo to Y3.

Br3 atoms cap triangular faces on the cluster, much like Br1 and Br3 did in $Y_{16}Br_{20}Ru_4$. However, in $Y_{16}Br_{24}Ir_4$, four Br1 and four Br2 atoms are bonded in an inner fashion to Y atoms in only one cluster, capping Y2-Y4-Y4 and Y2-Y1-Y1 triangular faces, respectively. The Br3 atoms simultaneously cap the four Y2-Y3-Y3 triangular faces of one cluster, while bonding exo to Y3 atoms from four neighboring clusters in a fashion identical to that adopted by Br1 in $Y_{16}Br_{20}Ru_4$. The slightly larger size of the Y triangular faces in this compound compared to the Ru phase results in larger capping angles; Y-Br-Y capping angles for Br1, Br2 and Br3 range from 76.5° to 82.6°, compared to a maximum value of 79.9° in the Ru phase. The bonding modes of Br4, Br5 and Br6 atoms are pictured in Figure 11. Each of these atom types bridge one edge of the triangular faces corresponding to the truncation of the tetrahedron, namely the Y1-Y3-Y4 face. The four Br4 atoms bridge the Y3-Y4 edges of one cluster, while occupying a position exo to Y4 atoms in four adjacent clusters. Similarly, the four Br5 atoms bridge Y1-Y4 edges of one cluster and are exo to Y1 atoms in four neighboring clusters. These atoms have functionalities similar to, but not identical with, that adopted by Br2 in $Y_{16}Br_{20}Ru_4$. The four Br6 atoms bridge Y1-Y3 edges on only one cluster, a functionality common in metal halide chemistry, but not found in $Y_{16}Br_{20}Ru_4$.

The structure of $Y_{16}Br_{24}Ir_4$ can also be described as Br and Ir atoms together forming distorted cubic-close-packed layers, with Y atoms filling octahedral sites next to the Ir atoms. The close-packed layers, similar to those

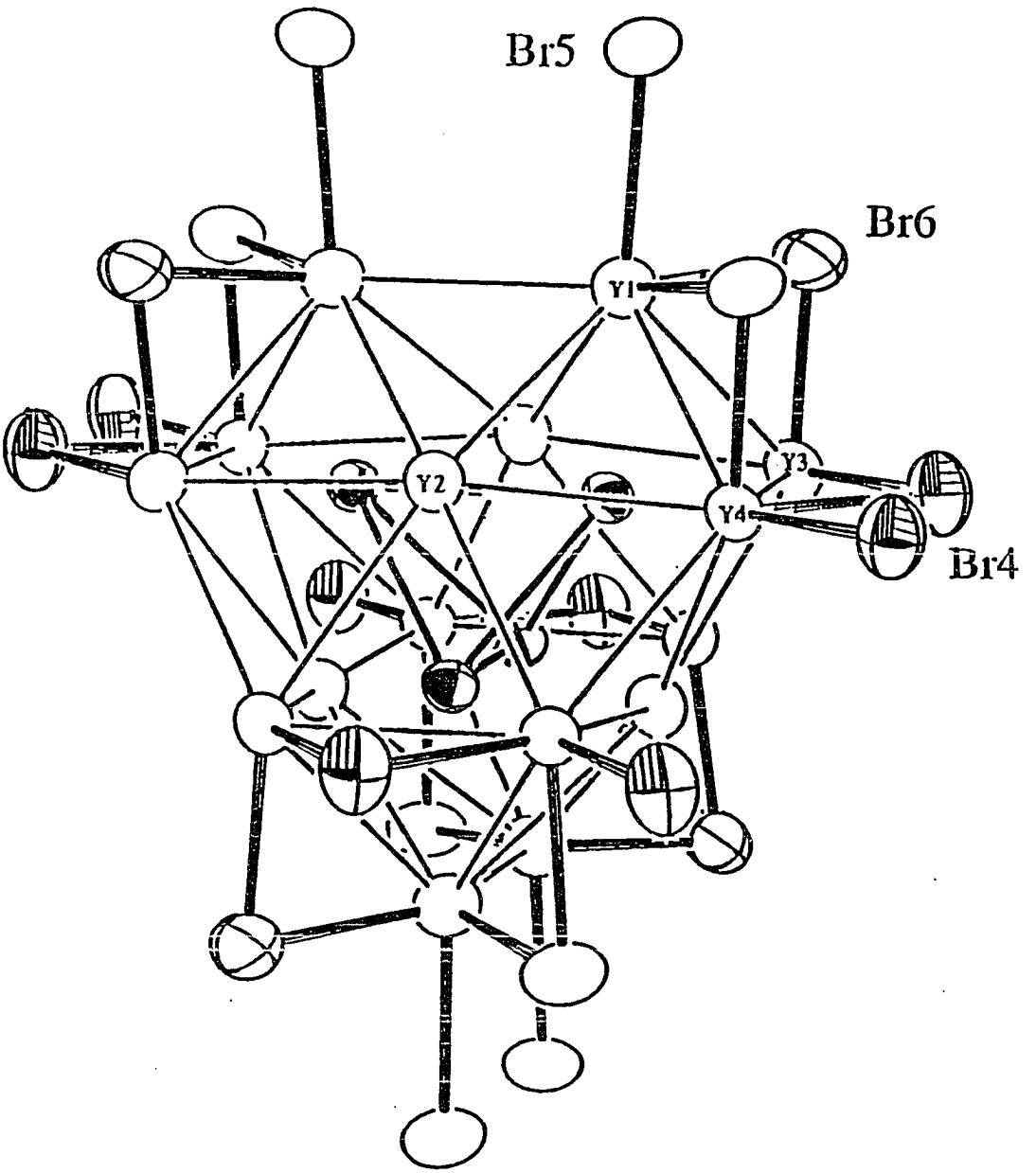

Figure 11. [110] view of the bonding modes adopted by Br4, Br5, and Br6 atoms; $\vec{c}$ is vertical. Br4 and Br5 bridge the Y3-Y4 and Y1-Y4 edges, respectively, while bonding exo to Y atoms in adjacent clusters. Br6 bridges only the Y1-Y3 edges of the cluster.

present in $Y_{16}Br_{20}Ru_4$ (shown previously in Figure 4), lie parallel to (124), (12$\bar{4}$), ($\bar{1}$24), and ($\bar{1}$2$\bar{4}$), which correspond to the orientations of the four triangular faces of the Ir tetrahedra. The shortest Br-Br contacts of 3.59 Å occur between Br1 atoms in adjacent close-packed layers.

Each $Y_{16}Ir_4$ cluster is surrounded by a total of 36 Br atoms, as shown in Figure 12, where heavier Y-Br and Y-Ir bonds are drawn to emphasize the octahedral geometry about each Y atom. The Br atoms adopt a geometry around the cluster very much like that in $Y_{16}Br_{20}Ru_4$. This similarity is best seen by comparing Figure 12 to Figure 3b. The Y-Br bond distances vary from 2.79(1) Å to 3.144(7) Å, a wider range than was found in $Y_{16}Br_{20}Ru_4$, but consistent with the variations in Br functionality and the lower symmetry. The average Y-Br bond distance in $Y_{16}Br_{24}Ir_4$ is 2.937 Å, notable smaller than the average of 3.000 Å observed in the Ru phase, yet larger than the sum of crystal radii, 2.86 Å (for six-coordinate Br^{-1}). The presence of shorter average Y-Br distances is consistent with the increased number of Br atoms per cluster, ie. more Br atoms bonded only to one cluster unit than in $Y_{16}Br_{20}Ru_4$, and the ensuing reduction in the Br coordination number; Br atoms in $Y_{16}Br_{24}Ir_4$ are bonded to either two or three Y atoms, while coordination numbers in $Y_{16}Br_{20}Ru_4$ range from two to four. Each Y1, Y3, and Y4 atom is bonded to 5 Br and one Ru atom in a pseudo-octahedral fashion. Each Y2 atom is at the center of a distorted trigonal antiprism (or highly distorted octahedron) formed by a triangle of Ru atoms and a triangle of Br atoms. The Y-Br distances *trans* to Ru atoms are significantly longer than

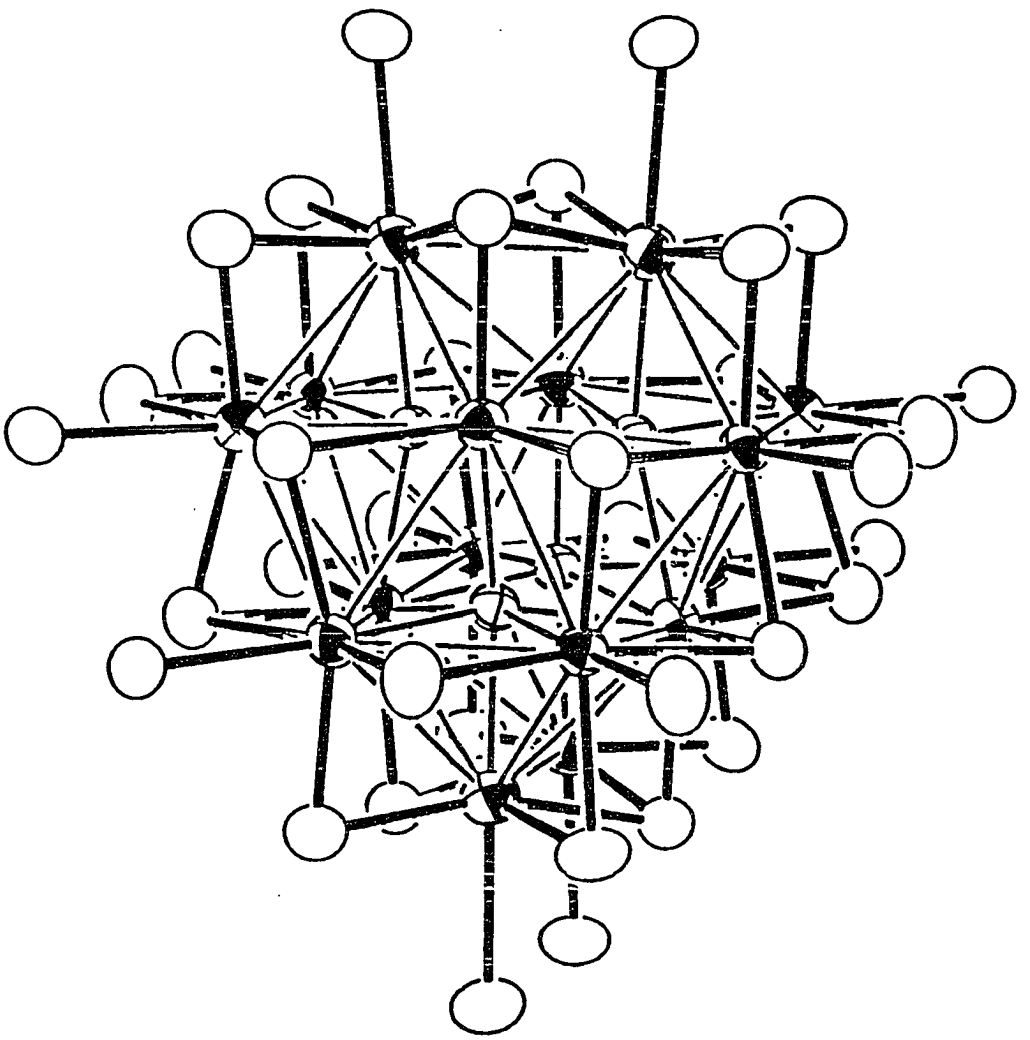

Figure 12. ~[110] view of a $Y_{16}Ir_4$ cluster and the 36 surrounding Br atoms; $\vec{c}$ is vertical. Each Y (quarter-shaded ellipsoid) is octahedrally coordinated by a combination of Br (open) and Ir (crossed) atoms, which form a distorted cubic-close-packed network.

the other Y-Br distances around a given Y atom, and correspond to the six largest Y-Br distances observed in the compound. Also, the atoms involved in outer-inner (intercluster) bonding occupy positions *trans* to Ru atoms, while the shortest Y-Br distances occur for Br6, which is two-bonded inner to only one cluster.

Every $Y_{16}Ir_4$ cluster is connected to ten neighboring clusters via Br bridges. As shown in Figure 13, each cluster is connected to six adjacent clusters within the a-b plane, forming a pseudo-hexagonal network or nearly close-packed layer. Along the a-axis, the clusters are bridged by Br3 atoms, yielding intercluster distances of 4.74 Å and 4.79 Å between Y3 atoms. Along the b-axis, Br4 bridges diagonally between clusters, with an intercluster distance of 4.61 Å between Y4 atoms. These close-packed layers are stacked on top of each other along $\vec{c}$ (at z=1/8, 3/8, 5/8, and 7/8) such that a diamond glide relates the clusters; the second cluster layer is shifted by (0,1/4,1/4) from the first, and is then reflected through a mirror plane perpendicular to $\vec{a}$. The resultant cluster layer has been shifted by a translation of (-1/4,1/4,1/4) and contains clusters turned by 90° with respect to those in the first layer. A third cluster layer is positioned at (1/4,1/4,1/4) from the second layer, with the clusters oriented as in the first layer, ie. mirror images of the second layer. This diamond glide is repeated two more times until a layer identical to the first layer is found. In addition, the clusters in the layers stack vertically to create rows of clusters aligned alternately within the (110) and $(1\bar{1}0)$ planes. The shortest

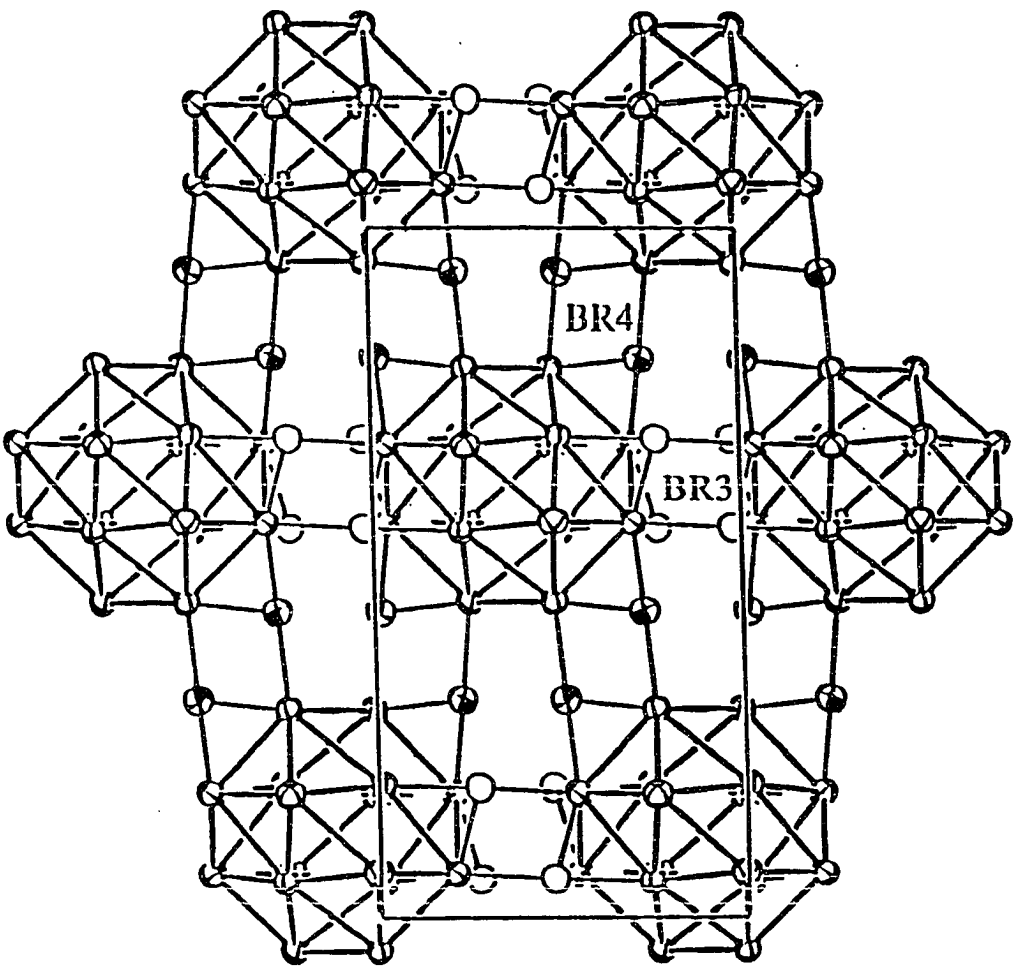

Figure 13. [00$\bar{1}$] view of the a-b plane at z=1/6, illustrating the pseudo-hexagonal (close-packed) cluster network. Br3 atoms (open ellipsoids) bridge along $\vec{a}$ (horizontal), while Br4 atoms (quarter-shaded) bridge along $\vec{b}$ (vertical).

repeating unit along $\vec{c}$ includes four cluster layers. These layers are not isolated, but are interconnected by Br5 atoms. In Figure 14, Br5 atoms bridge the clusters to four neighbors (in adjacent layers) in a pseudo-tetrahedral manner, somewhat similar to that seen in $Y_{16}Br_{20}Ru_4$ (see Figure 6b) although these $Y_{16}Ir_4$ clusters are not related by $\bar{4}$ symmetry; the rotation angles deviates from 90°. Additionally, the intercluster Br5 bridge connects the truncated corners of the Y tetrahedra (Y1-Y3-Y4) to the cluster edge (Y1-Y1) rather than to the waist of the cluster, resulting in a large increase in the vertical distances (along $\vec{c}$) between clusters compared to that found in $Y_{16}Br_{20}Ru_4$. The Y-Y intercluster distance along this bridge is 4.51 Å between Y1 atoms.

In addition to the many structural similarities between $Y_{16}Br_{24}Ir_4$ and $Y_{16}Br_{20}Ru_4$ that have been noted, dimensional relationships due to cluster packing and intercluster bridging also exist. The strongest relationship is between the a-b planes of $Y_{16}Br_{24}Ir_4$ and $Y_{16}Br_{20}Ru_4$. The cluster orientation and intercluster Br bonding modes are identical along $\vec{a}$ of $Y_{16}Br_{24}Ir_4$ and $\vec{a}$ and $\vec{b}$ of $Y_{16}Br_{20}Ru_4$ (compare Figures 6a and 13), resulting in a cell length of ~11.7 Å in these directions. The cluster is ~8 Å across at its waist, with the (tricapping) intercluster Br bridges accounting for the remainder of the unit cell length. Whereas the a-b plane of $Y_{16}Br_{20}Ru_4$ contains rows of clusters that form a square network, the a-b plane of $Y_{16}Br_{24}Ir_4$ consists of a pseudo-hexagonal network. This pseudo-hexagonal (close-packed) network can be obtained from the Ru structure, as illustrated in Figure 15. On the left side of the figure, the square-

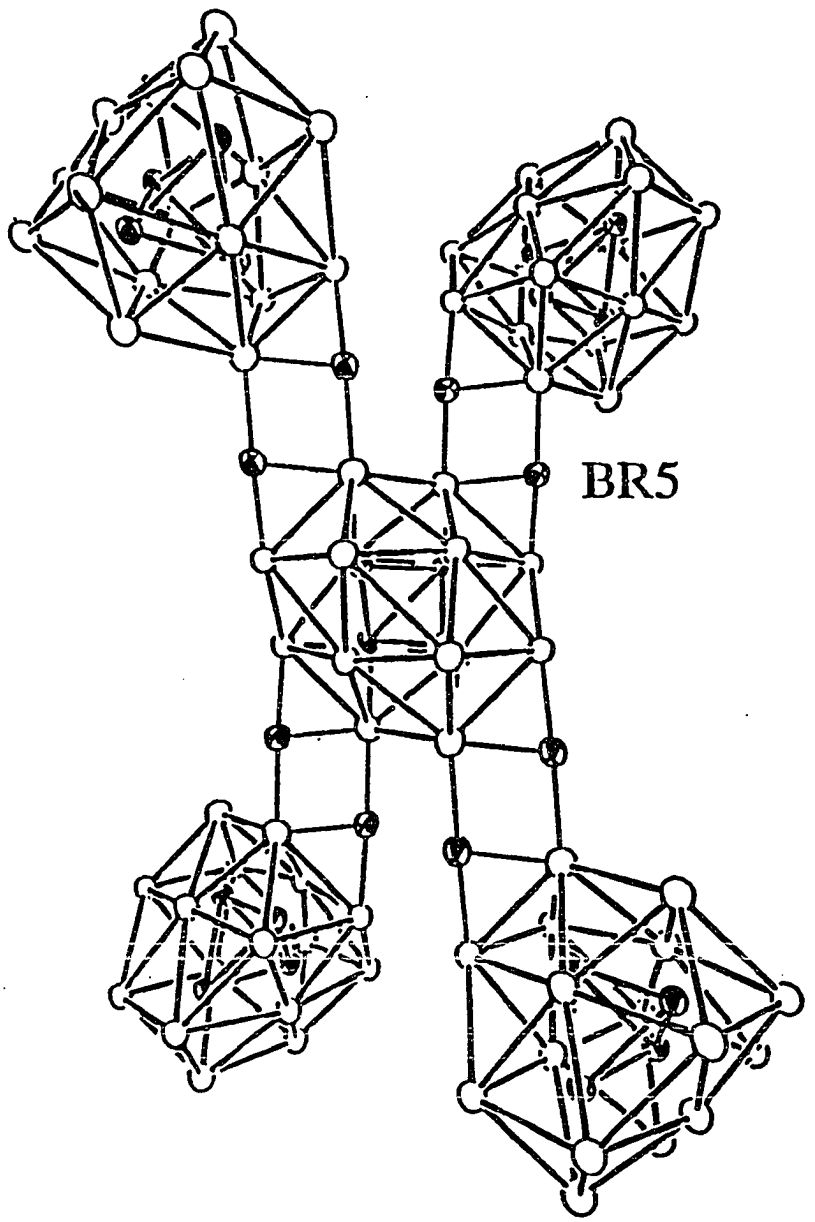

Figure 14. [$\bar{1}$00] view of intercluster bridging connections along $\vec{c}$ (vertical). Br5 atoms bridge four neighboring clusters in a pseudo-tetrahedral fashion.

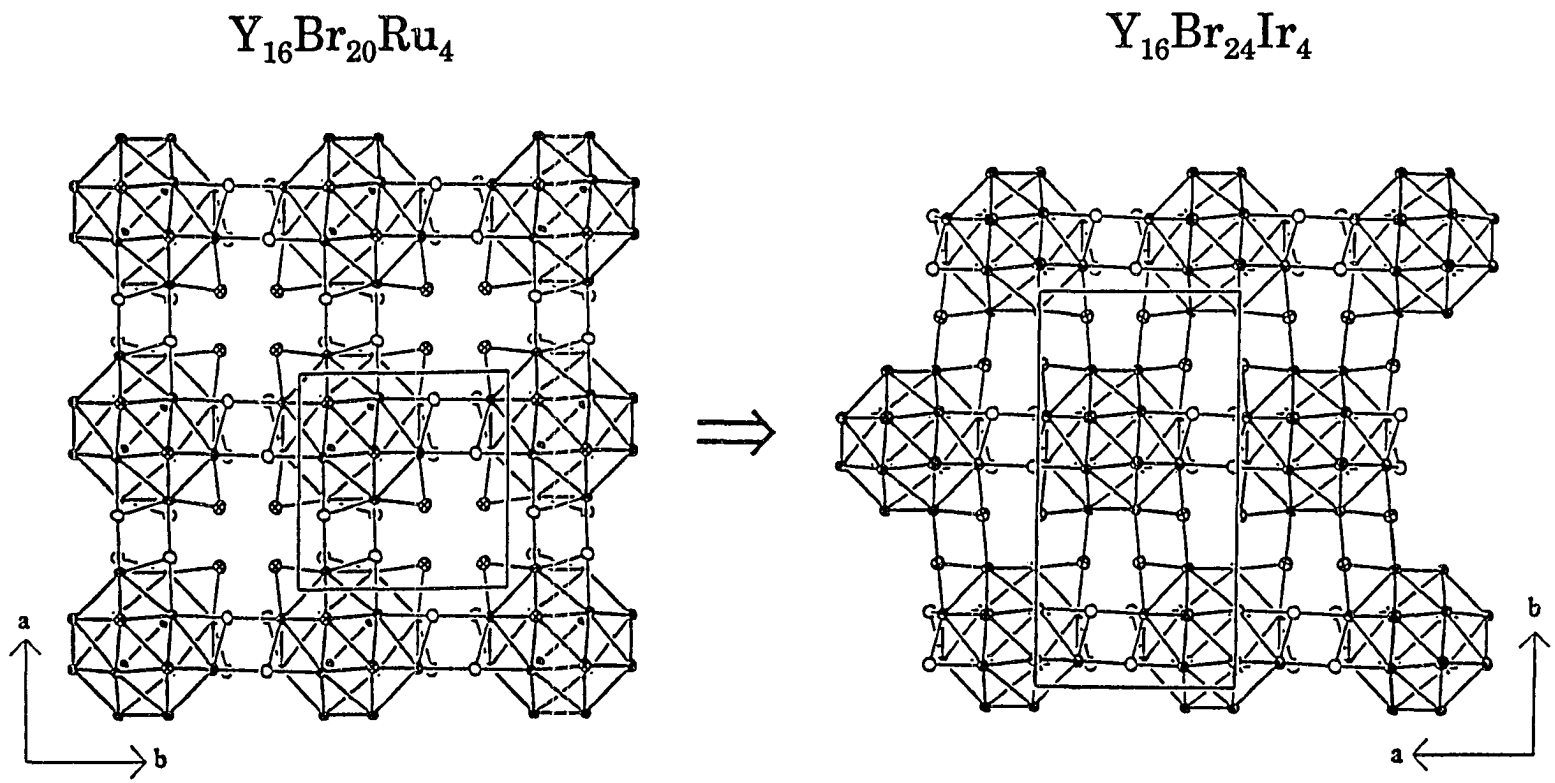

Figure 15. The cluster arrangement and Br bridging in the a-b plane of $Y_{16}Br_{24}Ir_4$ (pictured on the right) can be derived from that of $Y_{16}Br_{20}Ru_4$ (on the left) by shifting alternating rows of clusters by half a unit cell length along $\vec{b}$ (or $\vec{a}$). Hence, $Y_{16}Br_{24}Ir_4$ exhibits cell parameters related to those observed for $Y_{16}Br_{20}Ru_4$.

network of $Y_{16}Ru_4$ clusters at z=3/4 is pictured, along with the intercluster bonding (Br1) within the a-b plane and the edge-bridging Br (Br2) which is involved in interlayer bonding. By shifting every other (identical) row of clusters in this square network by 1/2 along $\vec{b}$ (or equivalently $\vec{a}$), the pseudo-hexagonal network seen in $Y_{16}Br_{24}Ir_4$ is generated. As seen in the $Y_{16}Br_{24}Ir_4$ layer (z=1/8) on the right, the formerly interlayer-bridging Br atoms (Br2 in $Y_{16}Br_{20}Ru_4$) now bridge clusters within one layer, while the tricapping Br atoms (Br1 in $Y_{16}Br_{20}Ru_4$) do not participate in intercluster bonding. This change in the layers within the a-b plane of $Y_{16}Br_{24}Ir_4$ increases the repeat length along $\vec{b}$ to two rows of clusters and intercluster bridges, resulting in a cell length (22.4 Å) of nearly twice the size of a. Due to the new intercluster bridging mode along $\vec{b}$ and, possibly, slight nesting of the cluster rows, a smaller than expected cell dimension is observed. Thus, the repeat length along $\vec{b}$ (22.4 Å) corresponds to two rows of clusters and two Br4 intercluster bridges. The repeat length along $\vec{c}$ corresponds to four rows of clusters and four Br5 intercluster bridges. Previously, it was noted that the bonding modes of Br4 and Br5 are very similar. Hence, the cell parameters (b and c) of $Y_{16}Br_{24}Ir_4$ are related by a factor of two. The c-axis lengths of the Ir and Ru phases are not closely related, due to the different bonding modes found in the phases. In $Y_{16}Br_{20}Ru_4$, the repeat length along $\vec{c}$ (17 Å) is approximately twice the size of the cluster, ie. two rows of clusters separated by a small gap (along $\vec{c}$) due to intercluster bridging.

$Y_{20}Br_{36}Ir_4$

One exciting feature of the chemistry of reduced rare-earth metal halides containing transition metal interstitials is the rich structural diversity that they exhibit. This diversity is apparent in the Y–Br–Ir system, where $Y_{20}Br_{36}Ir_4$ is one of three known cluster phases and two currently unidentified phases. The known phases, the title compound, $Y_{16}Br_{24}Ir_4$, and $Y_6Br_{10}Ir$,[87] incorporate a variety of structural elements. The compound $Y_6Br_{10}Ir$ is isostructural with $Y_6I_{10}Ir$[31] and consists of isolated Y_6Ir octahedra, which are connected via halogen bridges into infinite chains. Condensation of four Y_6Ir octahedra into isolated oligomeric clusters is observed in $Y_{16}Br_{24}Ir_4$. The structure of $Y_{20}Br_{36}Ir_4$ again contains isolated oligomeric clusters, with the additional feature of incorporation of a second structural unit, $YBr^{ch}_{4/2}Br^{cl}_{2/2}$ chains (ch=intrachain atoms, cl=bridge to clusters).

Synthesis

Although this compound was first observed several years ago,[87] its identification proved to be very challenging, owing to an inability to grow high quality single crystals of the material. In the current study, the phase was prepared in reactions spanning a wide range of compositions, appearing most often as black microcrystalline powder or small crystallites. Reactions loaded with metal-rich compositions of Y_3Br_2Ir and Y_2Br_2Ir were heated at 950°C for 30 days, followed by slow cooling (-5°/hr). The products of the first reaction type included small amounts (~20%) of nicely shaped black needles of $Y_6Br_{10}Ir$ and

aggregates of very small black gem-like crystals of $Y_{20}Br_{36}Ir_4$. Additional products were YOBr and a large amount of shiny gray massive chunks consisting of a variety of Y-Ir intermetallic phases (YIr, YIr_2, Y_5Ir_3) plus unreacted Y foil. The reaction with a smaller M:Br ratio yielded ~40% of $Y_{20}Br_{36}Ir_4$, with the balance of products consisting again of Y-Ir intermetallic phases (YIr, YIr_2, and Y_3Ir_2), YOBr and even a small amount of YBr_3. The reaction processes in these systems are not well understood, but clearly the reaction mixture was not at thermodynamic equilibrium. Still, the abundance of intermetallic phases in the products suggested that the phase contained more Br and less Ir.

Reactions were next loaded over a composition range from Y_3Br_3Ir to $Y_6Br_{10}Ir$ with a small amount (~15 mg.) of $AlBr_3$ added in an attempt to promote crystal growth. The reactions were heated very slowly to the final reaction temperature, hoping that the number of crystal nuclei formed would be small, thereby yielding larger, higher quality single crystals. The reactions were heated at 750°C for four days, then ramped (+5°/hr.) to 850°C, held constant for four more days, then ramped (+3°/hr.) to 950°C. After 14 days at this temperature, the reactions were slowly cooled (-5°/hr.) to 700°C before the furnace power was disconnected. The reaction loaded as $Y_6Br_{10}Ir$ gave nearly quantitative yield of that phase, with a small amount (<10%) of YOBr also. The other reactions with smaller Y:Br ratios produced moderate to high yields (a maximum of ≥80%) of $Y_{20}Br_{36}Ir_4$, again in the presence of small amounts of Y-Ir intermetallics,

YOBr, and either YBr_3 or in one case YBrH.[95] Additionally, small amounts (≤25%) of an unknown phase (or phases) were present. Although the yield of $Y_{20}Br_{36}Ir_4$ increased, the resultant crystals were still very small or poorly shaped, and no single crystals could be located. A reaction loaded as Y_5Br_8Ir with $AlBr_3$ added was heated at 860°C for 13 days, then 900°C for 26 days. The product was >80% black microcrystalline $Y_{20}Br_{36}Ir_4$ with traces of YOBr and YBr_3. Further heating of this product at 975°C for 36 days followed by quenching yielded, instead of $Y_{20}Br_{36}Ir_4$, a moderate amount (~40%) of the unidentified phase(s) along with YBr_3 and YOBr.

A reaction loaded stoichiometrically as Y_5Br_9Ir and heated slowly (over a five day period) to 975°C for 36 days before quenching yielded only ~20% of $Y_{20}Br_{36}Ir_4$, with roughly equal amounts of YBr_3 and the unknown phase(s), and a small amount of YOBr. Attempts at growing single crystals under a temperature gradient (925–950°C) for 12 weeks were relatively unsuccessful, usually resulting in YBr_3, YOBr, and intermetallic products. Using alkali-metal halides as a flux produced instead the ternary alkali-metal yttrium bromides and $Y_{16}Br_{24}Ir_4$.

In summary, the highest yield of $Y_{20}Br_{36}Ir_4$ was obtained from reactions loaded stoichiometrically or slightly Br-deficient and heated no higher than 900°C for several weeks. The addition of $AlBr_3$ seemed to increase the yield of the cluster phases, but did not result in single crystals. Reactions loaded over a range of compositions and heated at 950°–975°C for several weeks yielded, in

addition to $Y_{20}Br_{36}Ir_4$, moderate amounts of one or more other phases, which seem to be more metal-rich, but remain unidentified because of the lack of single crystals. At least one such phase also resulted from decomposition of $Y_{20}Br_{36}Ir_4$ at 975°C.

Structure determination

The structure determination proved to be as arduous as the preparation of single crystals. Based on the powder pattern of $Y_{20}Br_{36}Ir_4$, which contains eight intense low angle lines (with $2\theta<15.5°$) and numerous others, a relatively large unit cell was expected. A small weakly scattering crystal was placed on a Rigaku AFC6R automated four-circle diffractometer and was indexed to a primitive tetragonal cell with dimensions a=8.97 Å, c=22.5 Å. A data set was collected in this cell, but despite much effort, no solution was obtained. Another crystal from a different reaction indexed to a larger body-centered tetragonal cell with a=12.69 Å and c=45.09 Å; the cell was related to the first one by $\sqrt{2}$a, 2c. This larger cell matched one calculated by the TREOR program from 29 lines in the powder pattern. A data set collected for this primitive cell indicated that the Laue class was 4/m (based on data averaging) and the cell was most likely body-centered; although several weak violations to body-centering occurred, the majority of observed reflections met the condition hkl:h+k+l=2n. Unfortunately, the crystal quality was not very good; photographic studies on a Weissenberg camera confirmed the 45 Å cell, but indicated that the crystal was actually multiple. Structure solution again proved impossible.

The single crystal used for a successful structure determination was obtained from a reaction loaded as $Y_{10}Br_{13}Ir_3$ and heated at 975°C for 36 days before quenching. The product consisted of roughly equal amounts of black chunks of $Y_{20}Br_{36}Ir_4$, the unknown phase(s) and YBr_3, as well as a minor amount of YOBr. Oscillation photos indicated that the crystal quality was good.

Data collection was performed at room temperature on a Rigaku AFC6R automated diffractometer. A random search procedure located 25 peaks that indexed to the smaller tetragonal cell, a=8.97 Å, c=22.51 Å. The search was continued until 43 peaks were found, which had an average intensity of ~4600 counts. Indexing with several different combinations of 25 peaks consistently gave this small cell, contrary to the previous results. Subsequently, the small cell was converted to the larger cell, a=12.67 Å, c=45.02 Å. Axial photos confirmed the larger dimensions and the diffractometer programs identified the Laue class as 4/m. A quadrant of data (±h,k,l) was collected to a maximum 2θ of 50° without imposing the body-centering condition. Due to the relatively weak scattering power of the crystal, the scan speed was lowered from the normal 16°/min. to 8°/min. Following data collection, three psi scan measurements were performed, which revealed a transmission range of 0.422–1.000. Important data collection and refinement parameters are listed in Table 12.

Data reduction included Lorentz-polarization corrections followed by an empirical absorption correction based on the averaged transmission curve. The standard data did not indicate significant decay of the crystal; no decay

Table 12. Crystallographic data for $Y_{20}Br_{36}Ir_4$

Crystal data	
Formula	Y_5Br_9Ir
Space group, Z	$I4_1/a$, 16
a (Å)[a]	12.6986(9)
c (Å)	45.11(1)
V (Å^3)	7274(3)
D_{calc} (g/cm^3)	4.952
μ (Mo Kα, cm^{-1})	427.11
Data collection	
Crystal dimensions, mm	0.11 x 0.17 x 0.19
Diffractometer	Rigaku AFC6R
Radiation, wavelength (Å)	Mo Kα, 0.71069
Scan mode	ω
Octant measured	±h,k,l
$2\theta_{max}$, deg.	50
Refinement	
No. of measured reflections	6813
No. of independent reflections	3265
No. of obs. indep. refl. ($I \geq 3\sigma_I$)	876
No. of variables	137
Transmission coefficient range	0.898-1.062
Secondary extinction coefficient	6.9(3) x 10^{-8}
R_{avg} ($I>0$, $I \geq 3\sigma_I$)	0.260, 0.082
R, R_w	0.0426,0.0502
Largest residual peak, e/Å^3	1.61 (1.46Å from Br7),-1.49

[a] Guinier cell constants from 26 powder pattern lines.

correction was applied. Examination of the data for possible extinction conditions showed that only ~7% of all possible violations to body centering (h+k+l≠2n) were observed. Also, the majority of these reflections occurred in 0kl or h0l zones. Closer inspection of the data revealed that in many cases these "violations" to body-centering occurred adjacent to more intense peaks allowed by I-centering and were most likely due to misidentification of the peaks, e.g., (0 2 29) mistaken for (0 2 30). This problem developed because the cell parameter along $\vec{c}$ was so large (45 Å) that the peaks in reciprocal space overlapped, or at least the scan ranges of the peaks overlapped. Other observed "violations" occurred in groups of reflections differing only by the l indices, e.g., (0 3 14) through (0 3 20) were observed. In addition to peak misidentification, these violations could have resulted from intensity "streaks" along this direction in reciprocal space, due to crystal imperfections or impurities on the surface of the crystal. In addition to the reflection conditions required by body-centering (h+k+l=2n), the data exhibited systematic absences for most reflections of the type hk0: h,k≠2n, 00l: l≠4n, which are conditions for the space group $I4_1/a$. Weissenberg photographs later confirmed this space group. Intensity statistics indicated a centrosymmetric space group.

Initially, structure solution was attempted in space group $I4_1/a$ using the direct methods routine of SHELXS-86 to obtain a starting model. However, none of the several trial models calculated provided a reasonable solution, most resulting in R-values near 35%. Solution attempts in space groups I4/m and $I\bar{4}$

proved equally futile, yielding solutions with R-values near 20%. Finally, after attempting refinement with several trial models in space group $I4_1$, a solution containing well-defined $Y_{16}Ir_4$ units was obtained. Refinement of these Y and Ir positions (twelve in all) and subsequent difference Fourier calculations resulted in the location of 20 other atoms; the isotropic refinement converged with an R-value of 6.1%, but the positional and thermal parameters of all the atoms were strongly correlated. Examination of ORTEP drawings of the clusters within the unit cell suggested that a glide plane was present in the a-b plane. When the cluster atom positions were tested for higher symmetry, an inversion center relating the clusters was located, which generated the observed glide plane; the true symmetry of the structure was $I4_1/a$. After transforming the coordinates of the cluster atoms to match the higher symmetry space group, refinement and subsequent difference Fourier calculations provided the remaining Y and Br atoms. The isotropic refinement converged with R=0.056 and R_w=0.064. Upon anisotropic refinement of the thermal parameters, the ellipsoids of two atoms were non-positive-definite. Application of a DIFABS absorption correction solved this problem; the isotropic refinement converged at R=0.0506, R_w=0.0590 and anisotropic refinement yielded final values of R=0.0426, R_w=0.0502. The anisotropic thermal parameters were generally well-behaved considering the relatively low observations:variables ratio, with only one atom (Br1) displaying a larger than normal anisotropy. The orientation of this anisotropic ellipsoid is perpendicular to a bridged octahedral edge, a feature similar to that seen in

$Y_6I_{10}Ir$,[31] which can be rationalized based on the bonding mode of the atom. Generally, the relative sizes and shapes of the Br atom ellipsoids are consistent with their varying functionalities in the structure. The largest positive and negative peaks in the final difference Fourier calculation were 1.61 e/Å^3, located 1.46 Å away from Br7, and -1.49 e/Å^3. Only one reflection had an observed structure factor that deviated from those calculated for the model by more than $5\sigma_F$. Positional and anisotropic thermal parameters are listed in Tables 13 and 14.

The powder pattern calculated from the structure model is in excellent agreement with the observed pattern. Lattice parameters were calculated with the LATT program based on the positions of 26 Guinier powder pattern lines. The powder pattern of a phase tentatively identified as "$Y_{20}Br_{36}Ru_4$" (noted in the earlier section) has many strong low angle lines that match those of $Y_{20}Br_{36}Ir_4$ although some lines are shifted, and appears to be structurally similar to this phase. Based on nine strong Guinier powder pattern lines, this new Ru-containing phase is tetragonal with a=12.701(3) Å and c=45.23(6) Å.

Structure description

The structure of $Y_{20}Br_{36}Ir_4$ is built up of two basic units or building-blocks, the first being $Y_{16}Ir_4$ oligomeric clusters, similar to those seen in $Y_{16}Br_{24}Ir_4$, and the second consisting of chains of edge-sharing $YBr^{ch}_{4/2}Br^{cl}_{2/2}$ octahedra. The $Y_{16}Ir_4$ clusters are encompassed by Br atoms, some of which are bonded only to one cluster and others that bridge between two clusters or between clusters and

Table 13. Positional and equivalent isotropic thermal parameters for $Y_{20}Br_{36}Ir_4$

Atom	Type	x	y	z	B_{eq}
Ir	16f	0.1265(2)	0.2106(2)	0.15110(5)	0.6(1)
Y1	16f	0.1411(4)	0.2057(5)	0.2118(1)	0.7(2)
Y2	16f	0.1690(5)	0.1970(5)	0.0899(1)	0.7(3)
Y3	16f	0.2373(5)	0.0242(5)	0.1537(1)	0.7(2)
Y4	16f	0.1769(5)	0.2028(5)	0.3454(2)	0.7(3)
Y5	16f	0.1518(4)	0.2004(5)	0.7171(1)	1.4(3)
Br1	16f	0.2465(5)	0.0003(5)	0.2178(1)	1.6(3)
Br2	16f	0.1389(6)	0.1982(6)	0.9080(1)	1.7(3)
Br3	16f	0.1603(5)	0.1947(5)	0.2800(1)	1.7(3)
Br4	16f	0.1548(4)	0.2023(5)	0.0231(1)	1.3(3)
Br5	16f	0.2314(5)	0.0177(5)	0.5919(1)	1.0(3)
Br6	16f	0.1280(6)	0.1891(6)	0.4069(1)	1.2(3)
Br7	16f	0.1515(5)	0.1815(5)	0.6565(1)	1.7(3)
Br8	16f	0.1569(5)	0.1939(5)	0.7784(1)	1.6(3)
Br9	16f	0.1425(5)	0.2031(5)	0.5311(1)	1.6(3)

Table 14. Anisotropic thermal parameters for $Y_{20}Br_{36}Ir_4$

Atom	U_{11}	U_{22}	U_{33}	U_{12}	U_{13}	U_{23}
Ir	0.008(1)	0.006(1)	0.007(1)	0.001(1)	-0.001(1)	0.004(1)
Y1	0.007(3)	0.011(3)	0.009(3)	0.002(3)	0.005(2)	-0.002(3)
Y2	0.011(4)	0.008(3)	0.009(3)	0.000(3)	0.001(2)	0.000(3)
Y3	0.008(3)	0.010(4)	0.008(3)	0.000(3)	-0.002(3)	-0.004(3)
Y4	0.009(3)	0.007(4)	0.011(3)	-0.004(3)	-0.005(2)	-0.001(2)
Y5	0.011(4)	0.019(4)	0.023(3)	0.009(4)	0.004(3)	-0.002(4)
Br1	0.049(5)	0.006(4)	0.008(4)	0.005(4)	-0.009(3)	0.004(3)
Br2	0.013(4)	0.019(4)	0.032(3)	0.005(4)	-0.004(3)	0.003(3)
Br3	0.018(5)	0.029(5)	0.016(3)	-0.009(4)	-0.001(3)	-0.001(4)
Br4	0.014(4)	0.025(5)	0.009(3)	0.000(4)	0.007(2)	-0.003(3)
Br5	0.015(4)	0.013(4)	0.009(4)	0.003(3)	-0.006(2)	0.001(2)
Br6	0.014(4)	0.016(4)	0.014(3)	0.004(3)	0.004(3)	-0.002(2)
Br7	0.020(4)	0.019(4)	0.024(4)	0.008(3)	-0.006(3)	-0.005(3)
Br8	0.021(5)	0.028(5)	0.011(3)	-0.002(4)	0.000(3)	-0.006(3)
Br9	0.014(4)	0.015(5)	0.031(3)	-0.000(5)	0.002(3)	0.001(3)

chains. This structure can be considered an extension of the trend observed upon replacement of Ru by Ir in $Y_{16}Br_{20}Ru_4$, which resulted in $Y_{16}Br_{24}Ir_4$ through incorporation of more basic Br atoms per cluster unit by replacing some $Br^{i\text{-}i}$ and $Br^{i\text{-}a}$ connections between the clusters with different $Br^{i\text{-}a}$ and Br^{i} bonding modes; in $Y_{16}Br_{20}Ru_4$, 32 Br atoms around each cluster were involved in intercluster bridging, while in $Y_{16}Br_{24}Ir_4$ only 24 Br atoms took part in intercluster bridging. With the addition of a $YBr^{ch}_{4/2}Br^{cl}_{2/2}$ chain to the structure, only 16 Br atoms connected to a cluster are shared by other clusters; eight other Br atoms bridge between clusters and chains, and twelve more Br atoms take part only in intracluster bonding. Remarkably, while these Br atoms are redistributed, no overall change is observed in the number of electrons available for cluster bonding; all the phases described so far maintain 60 cluster electrons. The $YBr^{ch}_{4/2}Br^{cl}_{2/2}$ chain that is assimilated into $Y_{20}Br_{36}Ir_4$ formally contains yttrium (III) and does not change the electron count.

The tetragonal unit cell of $Y_{20}Br_{36}Ir_4$, shown in Figure 16, is body-centered and contains a total of four $Y_{16}Ir_4$ oligomeric units along with infinite chains of $YBr^{ch}_{4/2}Br^{cl}_{2/2}$ edge-sharing octahedra that parallel $\vec{a}$ and $\vec{b}$. These chains consist of Y_2Br_{10} "dimers" connected in a skewed fashion so that two non-opposite edges of each dimer are shared, forming an infinite unbranched zigzag chain. A variation of this style of zigzag chain occurs in $ZrCl_4$.[96] The Y atoms in the oligomer form a distorted tetra-capped truncated tetrahedron, which encloses an Ir tetrahedron oriented coincident with the outer truncated tetrahedron. The

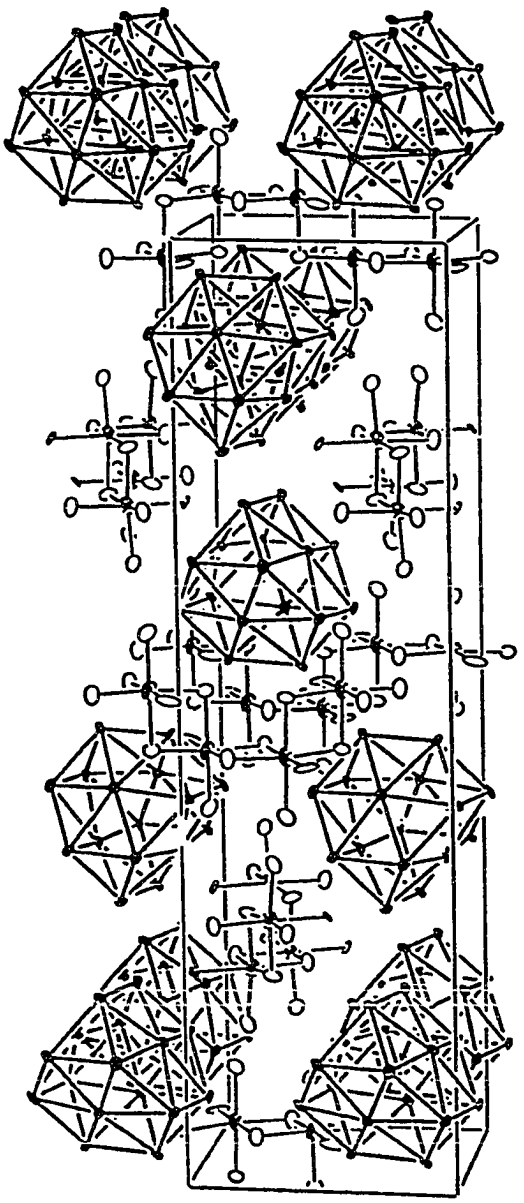

Figure 16. [$\bar{1}$00] view of the $Y_{20}Br_{36}Ir_4$ unit cell, illustrating the body-centered nature of the cluster packing. The structure is built of $Y_{16}Ir_4$ clusters and $YBr^{ch}_{4/2}Br^{cl}_{2/2}$ chains. For clarity, only Br atoms in the chains are pictured. $\vec{b}$ is horizontal, $\vec{c}$ is vertical.

clusters are centered around (0, 1/4, 1/8), (1/2, 1/4, 3/8), and the corresponding (I-centered) symmetry-related sites. The clusters possess $\bar{4}$ (S_4) symmetry, with the improper rotation axis along $\vec{c}$. As was the case for $Y_{16}Br_{24}Ir_4$, the clusters are of much lower symmetry compared to those in $Y_{16}Br_{20}Ru_4$, which exhibited $\bar{4}2m$ (D_{2d}) symmetry; the 2-fold rotational axis and mirror planes are absent. The clusters contain four crystallographically distinct types of Y atoms, as shown in Figure 17. Atoms Y1, Y3, and Y4 make up the distorted truncated tetrahedron, while Y2 atoms cap the four pseudo-hexagonal faces. The Y1 and Y2 atoms occupy similar sites in both $Y_{16}Br_{20}Ru_4$ and $Y_{16}Br_{24}Ir_4$. The Y3 and Y4 atoms in this phase sit in positions that are equivalent to Y3 in $Y_{16}Br_{20}Ru_4$. The absence of symmetry along $\vec{b}$ is clear in Figure 17, where $\vec{c}$ is vertical and $\vec{a}$ is horizontal; the clusters are oriented so that the b-axis passes through the two Y2-Y4 edges in the center of the picture (perpendicular to the plane of the paper). This orientation, in combination with the observed cluster packing, creates rather large holes in the structure, which are filled with $YBr^{ch}_{4/2}Br^{cl}_{2/2}$ chains.

The lack of mirror symmetry within the cluster is most pronounced in the Y1-Y3-Y4 triangular faces, which correspond to the truncated corners of the Y tetrahedron. From the bond distances and angles, listed in Tables 15, 16, and 17, the Y1-Y3 distance is nearly 0.05 Å longer than the Y1-Y4 distance. However, the Y2-Y distances in the hexagonal faces are closer to being equivalent (by mirror symmetry); the horizontal Y2-Y3 distance (3.767(8) Å) in

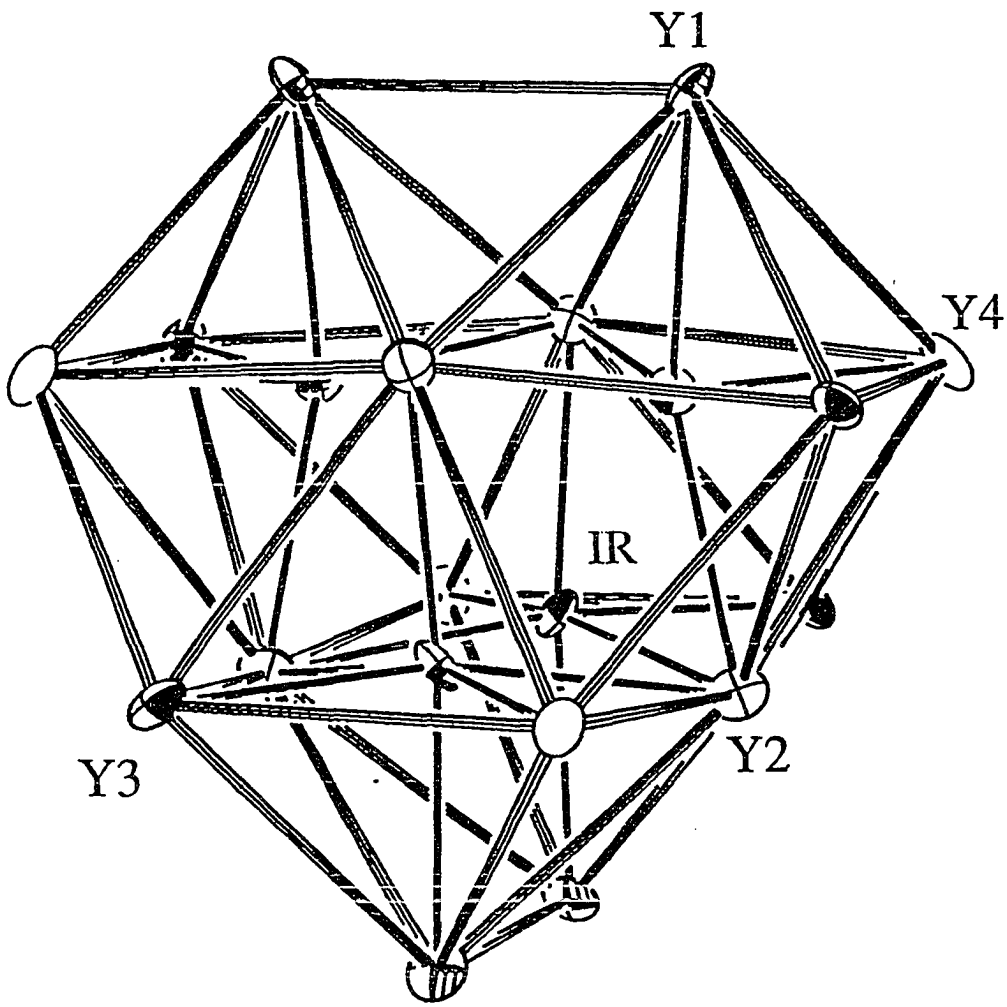

Figure 17. [0$\bar{1}$0] view of a $Y_{16}Ir_4$ cluster ($\bar{4}$ symmetry), illustrating the four crystallographically distinct types of Y atoms. $\vec{a}$ is horizontal, $\vec{c}$ is vertical. Each atom type has a unique symbol.

Table 15. Important bond distances around Y and Ir atoms in $Y_{20}Br_{36}Ir_4$

Ir-Ir	(x2)	3.348(4)	Y2-Y3	3.767(8)	Y4-Y1	3.651(9)
Ir-Ir		3.366(5)	Y2-Y4	3.737(8)	Y4-Y2	3.737(8)
Ir-Y1		2.743(6)	Y2-Y4	3.771(9)	Y4-Y2	3.771(9)
Ir-Y2		2.817(6)	$\bar{d}_{Y2\text{-}Y}$	3.748	Y4-Y3	3.634(8)
Ir-Y2		2.836(8)	Y2-Ir	2.743(6)	Y4-Y3	3.780(7)
Ir-Y2		2.841(7)	Y2-Ir	2.817(6)	$\bar{d}_{Y4\text{-}Y}$	3.715
Ir-Y3		2.756(7)	Y2-Ir	2.836(8)	Y4-Ir	2.732(8)
Ir-Y4		2.732(8)	Y2-Br4[b]	3.022(8)	Y4-Br2[b]	3.133(9)
$\bar{d}_{Ir\text{-}Y}$		2.788	Y2-Br5[b]	3.01(1)	Y4-Br2	2.85(1)
Y1-Y1		3.75(1)	Y2-Br6[b]	2.96(1)	Y4-Br3	2.96(1)
Y1-Y2	(x2)	3.745(8)	$\bar{d}_{Y2\text{-}Br}$	3.00	Y4-Br5	2.90(1)
Y1-Y3		3.696(7)	Y3-Y1	3.696(7)	Y4-Br6	2.85(1)
Y1-Y4		3.651(9)	Y3-Y2	3.721(8)	$\bar{d}_{Y4\text{-}Br}$	2.94
$\bar{d}_{Y1\text{-}Y}$		3.714	Y3-Y2	3.767(8)	Y5-Y5[a]	4.05(1)
Y1-Ir		2.743(6)	Y3-Y4	3.634(8)	Y5-Y5[a]	4.08(1)
Y1-Br1		2.946(9)	Y3-Y4	3.780(7)	Y5-Br1	2.86(1)
Y1-Br3[b]		3.093(8)	$\bar{d}_{Y3\text{-}Y}$	3.720	Y5-Br7	2.74(1)
Y1-Br3		2.85(1)	Y3-Ir	2.756(7)	Y5-Br8	2.770(9)
Y1-Br4		2.874(8)	Y3-Br1	2.908(9)	Y5-Br8	2.78(1)
Y1-Br4		2.861(9)	Y3-Br2	2.90(1)	Y5-Br9	2.786(9)
$\bar{d}_{Y1\text{-}Br}$		2.925	Y3-Br5	2.867(9)	Y5-Br9	2.781(9)
Y2-Y1	(x2)	3.745(8)	Y3-Br6	2.91(1)	$\bar{d}_{Y5\text{-}Br}$	2.79
Y2-Y2[a]	(x3)	4.50(1)	Y3-Br7[b]	2.972(9)	$\bar{d}_{Y\text{-}Y}$[a]	3.726
Y2-Y3		3.721(8)	$\bar{d}_{Y3\text{-}Br}$	2.911	Br6-Br6[c]	3.60(1)

a Non-bonding distances not included in averaging.
b Br atom is positioned *trans* to an Ir atom.
c All other Br-Br distances are ≥3.73 Å.

Table 16. Intracluster bond angles in $Y_{20}Br_{36}Ir_4$

Y1	Ir	Y2	164.3(2)	Y1	Y1	Y4	120.6(2)	Y4	Y2	Y4	118.3(2)
Y1	Ir	Y2	84.3(2)	Y2	Y1	Y2	73.9(2)	Y2	Y3	Y4	61.1(2)
Y1	Ir	Y2	84.2(2)	Y2	Y1	Y3	96.2(2)	Y1	Y3	Y2	95.9(2)
Y1	Ir	Y3	84.5(2)	Y2	Y1	Y4	61.3(2)	Y1	Y3	Y2	60.2(2)
Y1	Ir	Y4	83.6(2)	Y2	Y1	Y3	60.8(2)	Y1	Y3	Y4	59.7(2)
Y2	Ir	Y2	105.1(2)	Y2	Y1	Y4	96.4(2)	Y1	Y3	Y4	119.1(2)
Y2	Ir	Y2	104.9(2)	Y3	Y1	Y4	59.3(2)	Y2	Y3	Y2	73.6(2)
Y2	Ir	Y3	83.8(2)	Y1	Y2	Y1	60.2(2)	Y2	Y3	Y4	60.4(2)
Y2	Ir	Y4	84.7(2)	Y1	Y2	Y3	165.5(2)	Y2	Y3	Y4	96.3(2)
Y2	Ir	Y2	104.9(2)	Y1	Y2	Y3	59.0(1)	Y2	Y3	Y4	59.4(2)
Y2	Ir	Y3	164.5(2)	Y1	Y2	Y4	118.9(2)	Y4	Y3	Y4	120.8(2)
Y2	Ir	Y4	85.2(2)	Y1	Y2	Y4	117.7(2)	Y1	Y4	Y2	60.6(2)
Y2	Ir	Y3	84.6(2)	Y1	Y2	Y3	118.3(2)	Y1	Y4	Y2	96.4(2)
Y2	Ir	Y4	163.3(2)	Y1	Y2	Y3	118.6(2)	Y1	Y4	Y3	119.2(2)
Y3	Ir	Y4	82.9(2)	Y1	Y2	Y4	165.1(2)	Y1	Y4	Y3	61.0(2)
Ir	Ir	Y1	94.1(1)	Y1	Y2	Y4	58.1(2)	Y2	Y4	Y2	73.4(2)
Ir	Ir	Y2	101.5(2)	Y3	Y2	Y3	118.3(2)	Y2	Y4	Y3	59.0(2)
Ir	Ir	Y3	95.2(2)	Y3	Y2	Y4	58.3(1)	Y2	Y4	Y3	96.9(2)
Ir	Ir	Y4	92.1(1)	Y3	Y2	Y4	60.6(2)	Y2	Y4	Y3	60.1(1)
Y1	Y1	Y2	59.9(1)	Y3	Y2	Y4	60.5(2)	Y2	Y4	Y3	60.6(2)
Y1	Y1	Y3	120.2(2)	Y3	Y2	Y4	164.5(2)	Y3	Y4	Y3	120.2(2)

Table 17. Bond angles around Y and Br in $Y_{20}Br_{36}Ir_4$

Ir	Y1	Br1	98.2(2)	Ir	Y3	Br7	177.7(4)	Br7	Y5	Br8	173.2(3)
Ir	Y1	Br3	178.5(3)	Br1	Y3	Br2	86.4(2)	Br7	Y5	Br8	96.6(3)
Ir	Y1	Br3	100.3(2)	Br1	Y3	Br5	160.3(3)	Br7	Y5	Br9	89.5(3)
Ir	Y1	Br4	100.9(2)	Br1	Y3	Br6	85.2(3)	Br7	Y5	Br9	96.1(3)
Ir	Y1	Br4	101.1(2)	Br1	Y3	Br7	81.2(2)	Br8	Y5	Br8	85.5(2)
Br1	Y1	Br3	80.3(2)	Br2	Y3	Br5	90.4(3)	Br8	Y5	Br9	88.8(3)
Br1	Y1	Br3	88.8(2)	Br2	Y3	Br6	161.5(3)	Br8	Y5	Br9	90.4(3)
Br1	Y1	Br4	160.8(2)	Br2	Y3	Br7	83.9(3)	Br8	Y5	Br9	173.0(3)
Br1	Y1	Br4	85.7(3)	Br5	Y3	Br6	92.0(3)	Br8	Y5	Br9	89.6(3)
Br3	Y1	Br3	79.6(2)	Br5	Y3	Br7	79.2(2)	Br9	Y5	Br9	86.4(2)
Br3	Y1	Br4	80.5(2)	Br6	Y3	Br7	78.7(3)	Y1	Br1	Y3	78.3(2)
Br3	Y1	Br4	78.8(2)	Ir	Y4	Br2	178.0(3)	Y1	Br1	Y5	174.1(3)
Br3	Y1	Br4	86.8(3)	Ir	Y4	Br2	100.3(3)	Y3	Br1	Y5	95.8(3)
Br3	Y1	Br4	158.4(3)	Ir	Y4	Br3	97.9(3)	Y3	Br2	Y4	78.3(3)
Br4	Y1	Br4	91.7(2)	Ir	Y4	Br5	99.9(3)	Y3	Br2	Y4	173.4(3)
Ir	Y2	Br4	164.7(3)	Ir	Y4	Br6	99.6(3)	Y4	Br2	Y4	101.9(3)
Ir	Y2	Br5	96.2(2)	Br2	Y4	Br2	77.8(3)	Y1	Br3	Y1	100.4(2)
Ir	Y2	Br6	95.1(3)	Br2	Y4	Br3	82.7(3)	Y1	Br3	Y4	175.4(3)
Ir	Y2	Br4	95.1(2)	Br2	Y4	Br5	82.1(2)	Y1	Br3	Y4	78.0(2)
Ir	Y2	Br5	165.3(3)	Br2	Y4	Br3	86.4(3)	Y1	Br4	Y1	81.8(2)
Ir	Y2	Br6	96.1(3)	Br2	Y4	Br5	159.2(3)	Y1	Br4	Y2	79.0(2)
Ir	Y2	Br5	95.1(3)	Br2	Y4	Br6	88.9(3)	Y1	Br4	Y2	78.8(2)
Ir	Y2	Br6	165.2(3)	Br2	Y4	Br6	79.8(2)	Y2	Br5	Y3	78.6(2)
Y4	Y2	Br4	93.4(2)	Br3	Y4	Br5	86.0(3)	Y2	Br5	Y4	79.3(3)
Br4	Y2	Br5	94.3(2)	Br3	Y4	Br6	162.4(3)	Y3	Br5	Y4	81.9(3)
Br4	Y2	Br6	95.2(3)	Br5	Y4	Br6	92.6(3)	Y2	Br6	Y3	79.8(3)
Br5	Y2	Br6	94.4(3)	Br1	Y5	Br7	86.2(3)	Y2	Br6	Y4	80.1(2)
Ir	Y3	Br1	98.8(2)	Br1	Y5	Br8	87.3(2)	Y3	Br6	Y4	82.0(2)
Ir	Y3	Br2	98.5(3)	Br1	Y5	Br8	92.0(3)	Y3	Br7	Y5	96.8(3)
Ir	Y3	Br5	100.9(3)	Br1	Y5	Br9	91.8(3)	Y5	Br8	Y5	94.5(2)
Ir	Y3	Br6	99.0(3)	Br1	Y5	Br9	177.1(3)	Y5	Br9	Y5	93.5(2)

the closer hexagonal face (as seen in Figure 17) is within 0.5σ of the corresponding horizontal Y2-Y4 distance (3.771(9) Å) in the opposite hexagonal face. In fact, the Ir tetrahedron does exhibit mirror symmetry within experimental error, with the Ir-Ir edges that are coincident with Y1-Y1 edges 0.018(4) Å longer than the other four Ir-Ir edges. This implies that a slight compression along $\vec{c}$ is present. A similar trend is observed in the Y2-Y3 and Y2-Y4 distances; horizontal Y2-Y3 and Y2-Y4 distances in the hexagonal faces are ~0.04 Å longer than the vertical Y2-Y3 and Y2-Y4 distances.

Despite the minor differences mentioned above, the overall geometry of the clusters in $Y_{20}Br_{36}Ir_4$ is very similar to that of the clusters in $Y_{16}Br_{20}Ru_4$ and $Y_{16}Br_{24}Ir_4$. The average Y-Y intracluster distance of 3.726 Å (Pauling bond order is 0.15) is nearly identical to the average Y-Y distance in $Y_{16}Br_{24}Ir_4$ (3.721 Å), and is somewhat larger than that observed in $Y_{16}Br_{20}Ru_4$ (3.687 Å), the expansion consistent with the larger size of Ir compared to Ru. The five-coordinate Y1, Y3, and Y4 atoms, which share a common functionality in the cluster, have comparable average Y-Y distances. The average Y2-Y distance, however, is longer, consistent with its unique six-coordinate environment. These features are also present in both $Y_{16}Br_{20}Ru_4$ and $Y_{16}Br_{24}Ir_4$. The average Y-Ir distance in $Y_{20}Br_{36}Ir_4$ of 2.788 Å is nearly identical to that observed in $Y_{16}Br_{24}Ir_4$ and is shorter than the sum of Pauling's single bond radii, 2.88 Å. The Ir-Ir distances in $Y_{20}Br_{36}Ir_4$ are slightly longer (by ~0.04 Å) than is observed in $Y_{16}Br_{24}Ir_4$; the Pauling bond order is 0.04, signifying nearly insignificant Ir-Ir

interactions. The location of the Ir atoms seems more dependent on the position of the surrounding Y atoms and the resulting Y-Ir interactions than on their placement relative to other Ir atoms.

The cluster can also be described as an oligomer of four distorted Y_6Ir octahedra, generated by pairwise condensation of edge-sharing octahedra. In this view, the octahedra are very distorted, with the Ir atoms lying closer to the Y1, Y3, and Y4 atoms and farther away from the Y2 atoms. The Ir atoms are shifted out of the centers of the octahedra, towards the center of the cluster, while the Y2 atoms are shifted away from the cluster center. The magnitude of this distortion is evident in the bond angles around Ir; *trans* angles across each octahedron range from 163.3(2)° to 164.5(2)°, values intermediate between those seen in $Y_{16}Br_{20}Ru_4$ and $Y_{16}Br_{24}Ir_4$. The Y1 and Y3 atoms deviate farther from their apical positions than was observed in $Y_{16}Br_{20}Ru_4$; Ir-Ir-Y angles are 94–95° in this phase, compared to ~91° in the Ru phase.

There are nine crystallographically distinct types of Br atoms in $Y_{20}Br_{36}Ir_4$, which adopt five basic bonding modes. The bonding mode exhibited by Br4, Br5, and Br6 atoms is shown in Figure 18. Each of these atoms are bonded in an inner (bridging) fashion to three Y atoms that form a triangular face on only one cluster; Br4 caps the four Y1-Y1-Y2 triangular faces, while Br5 and Br6 cap eight of the twelve Y2-Y3-Y4 faces around the waist of the cluster so that each Y hexagon is capped by three Br atoms. In $Y_{16}Br_{24}Ir_4$, half of these Br atoms around the waist of the clusters are bridging to other clusters, while in

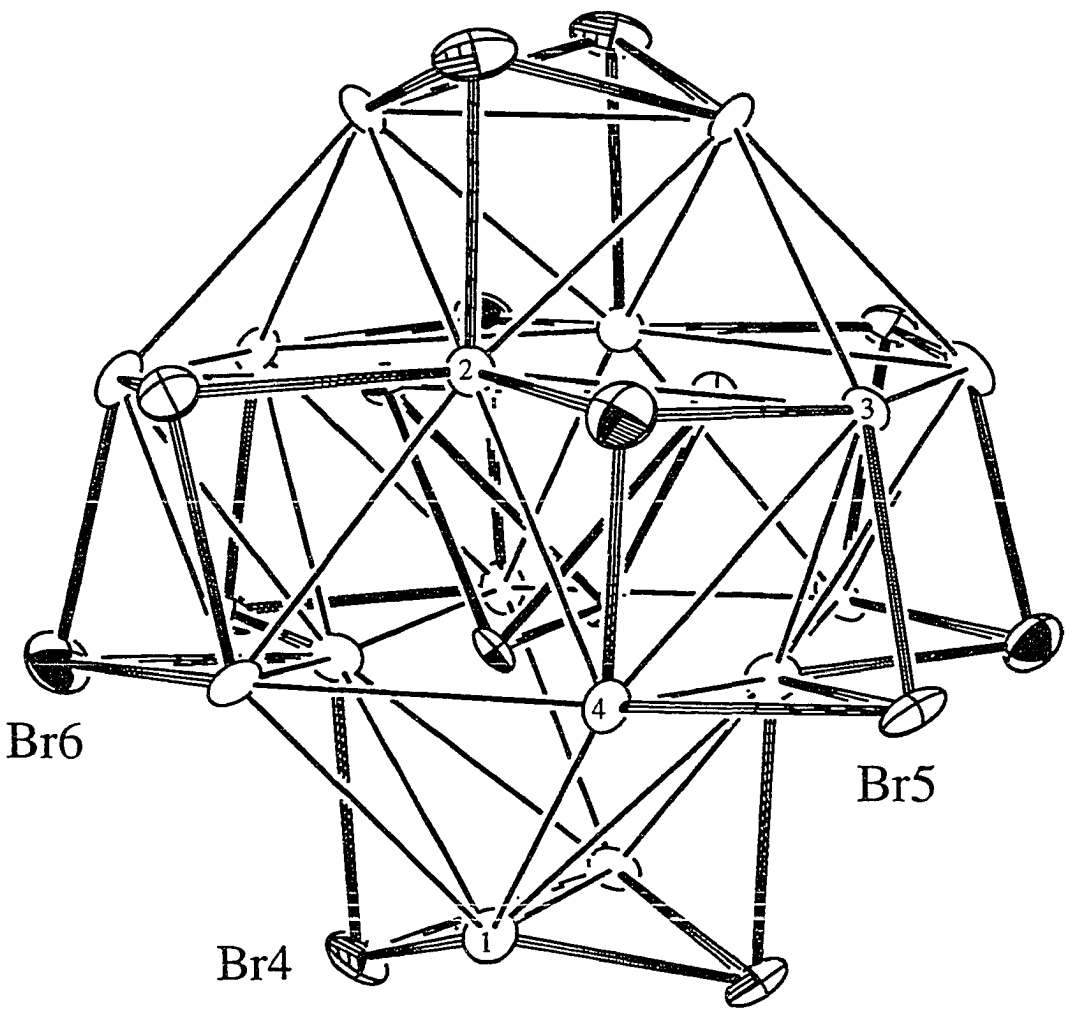

Figure 18. [0$\bar{1}$0] view of the bonding modes adopted by Br4, Br5, and Br6. The halogens cap triangular faces (Y1-Y2-Y1, Y2-Y3-Y4, and Y2'-Y3-Y4, respectively) within Y hexagons on only one cluster. $\vec{a}$ is horizontal, $\vec{c}$ is vertical.

$Y_{16}Br_{20}Ru_4$ all the Br atoms capping faces around the cluster's waist form intercluster bridges. The Y-Br-Y capping angles range from 78.6(2)° to 82.0(2)°; the range of angles is smaller than observed in $Y_{16}Br_{24}Ir_4$ (76.5°–82.6°), corresponding to a more consistent bonding mode in $Y_{20}Br_{36}Ir_4$. A second Br functionality is depicted in Figure 19, where Br2 and Br3 atoms maintain $Br^{i\text{-}a}$ bonding to the truncated corners of the Y tetrahedron. Four Br2 atoms bridge the Y3-Y4 edges while also bonding exo to Y4 atoms in four neighboring clusters. Similarly, Br3 atoms bridge the four Y1-Y4 edges and bond exo to Y1 atoms in four neighboring clusters. The functionalities of Br2 and Br3 atoms are identical to those seen for Br4 and Br5 atoms in $Y_{16}Br_{24}Ir_4$, respectively. Figure 20 illustrates the environments of the remaining Br and Y atoms. Four Br1 atoms bridge the Y1-Y3 edge (the third edge of the Y1-Y3-Y4 triangular face) and also bond exo to Y5, the atoms that forms the $YBr^{ch}_{4/2}Br^{cl}_{2/2}$ chains, in a $Br^{i\text{-}a}$ type connection. The four Br7 atoms also bridge between the clusters and chains, bonding exo ($Br^{a\text{-}a}$) to both Y3 and Y5. Atoms Br8 and Br9 are involved exclusively in $YBr^{ch}_{4/2}Br^{cl}_{2/2}$ intrachain bonding, bridging between adjacent Y5 atoms via $Br^{a\text{-}a}$ connections as shown in Figure 21a. The Br9 atoms bridge Y5 atoms that form "dimers" parallel to the a- or b-directions; a two-fold rotation axis perpendicular to $\vec{c}$ passes through the center of these "dimers". The Br8 atoms bridge between "dimers", which are related to each other by an inversion center located midway between diagonal Y5 atoms.

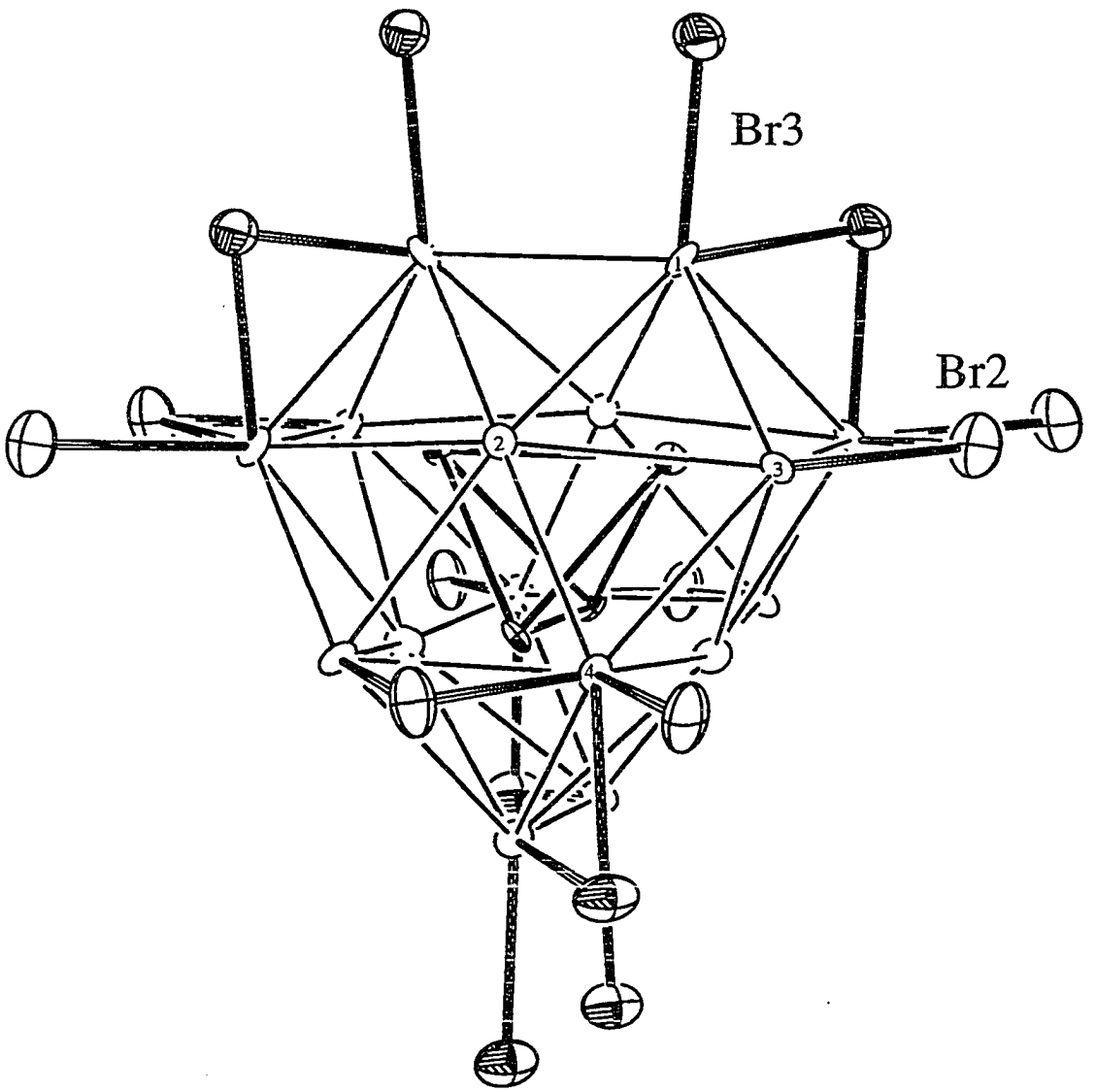

Figure 19. ~[0$\bar{1}$0] view of the bonding modes adopted by Br2 and Br3 atoms, which bridge the Y3-Y4 and Y1-Y4 edges, respectively, while bonding exo to Y vertices in adjacent clusters. $\vec{a}$ is horizontal, $\vec{c}$ is vertical.

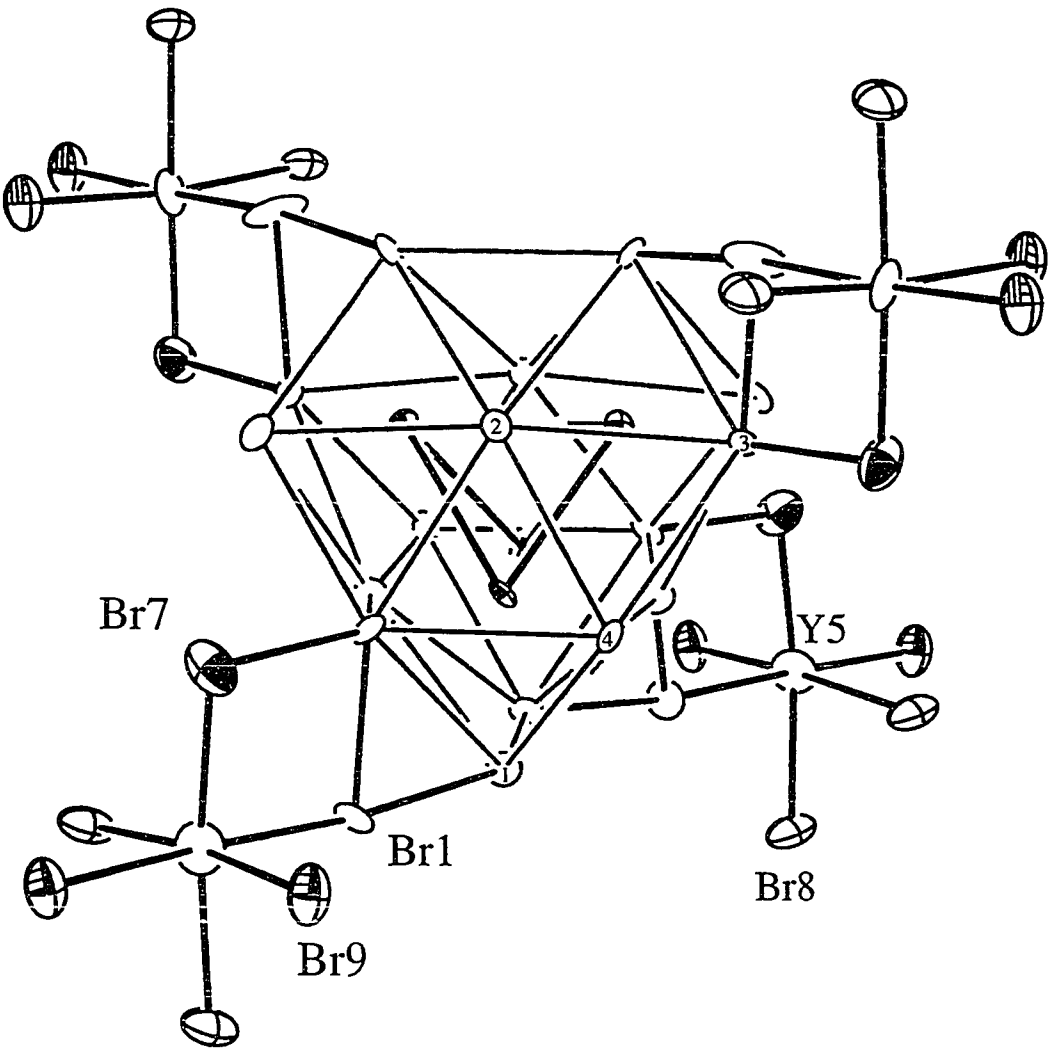

Figure 20. ~[0$\bar{1}$0] view of the bonding modes of Y5, Br1, Br7, Br8, and Br9, which make up the $YBr^{ch}_{4/2}Br^{cl}_{2/2}$ chains. Br1 bridges the Y1-Y3 edge while bonding to Y5, while Br7 is exo (outer) to both the Y3 vertice and the Y5 atom. Br8 and Br9 bond exclusively within the chain. $\vec{a}$ is horizontal, $\vec{c}$ is vertical.

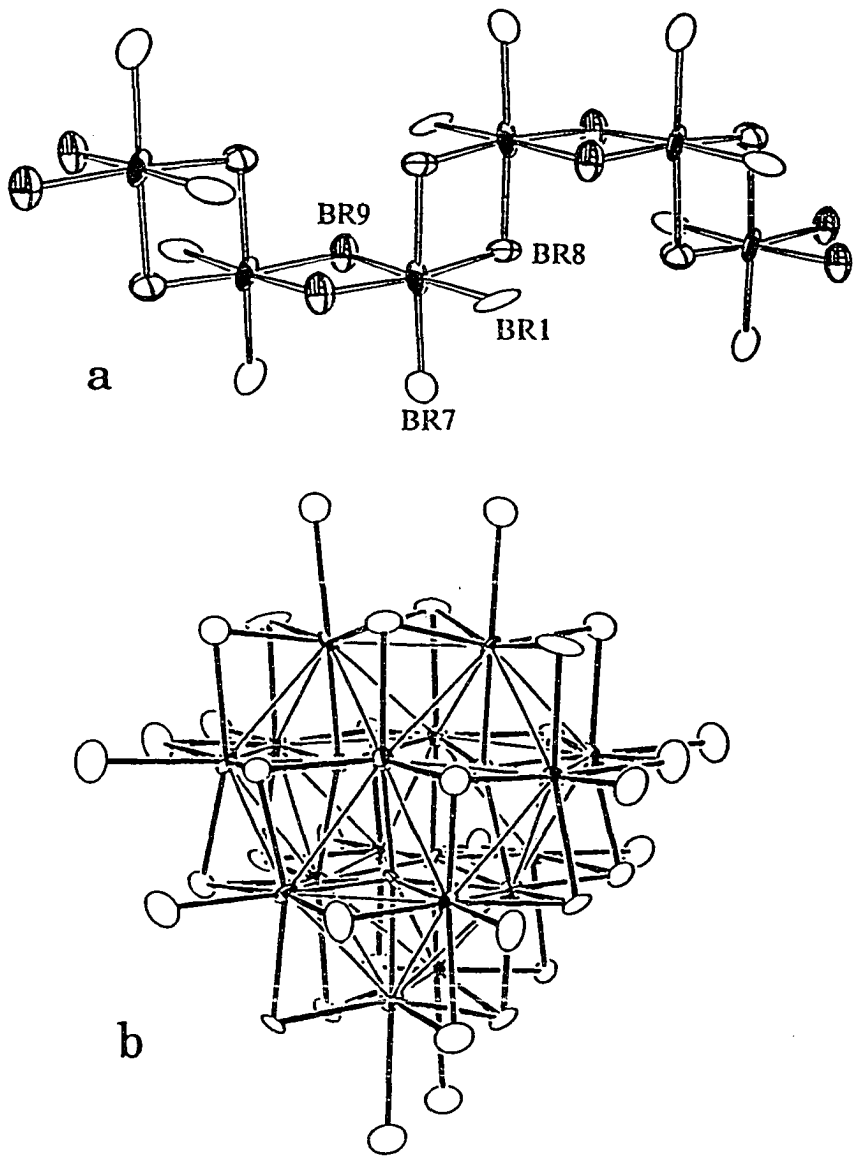

Figure 21. a) the $YBr^{ch}_{4/2}Br^{cl}_{2/2}$ chain, viewed as edge-sharing Y_2Br_{10} "dimers". Br8 bridges diagonally between dimers, while Br9 bridges horizontally within dimers. b) ~[0$\bar{1}$0] view of a $Y_{16}Ir_4$ cluster and the 36 surrounding Br atoms. Y quarter-shaded, Br open, Ir crossed. $\vec{a}$ is horizontal, $\vec{c}$ is vertical in both pictures.

Each $Y_{16}Ir_4$ cluster is surrounded by a total of 36 Br atoms, as shown in Figure 21b; the figure emphasizes the Y-Br and Y-Ir octahedral bonding network. The bonding arrangement of the seven crystallographically unique Br atoms encompassing these clusters is identical to that seen in $Y_{16}Br_{20}Ru_4$ and $Y_{16}Br_{24}Ir_4$. The Y-Br bond distances around the cluster range from 2.85(1) Å to 3.133(9) Å, with an average value of 2.94 Å. This average Y-Br distance is the same as that observed in $Y_{16}Br_{24}Ir_4$, which exhibits a slightly larger range of Y-Br distances, and is slightly smaller than found in $Y_{16}Br_{20}Ru_4$. The Y-Br distances in the $YBr^{ch}_{4/2}Br^{cl}_{2/2}$ chains are shorter, with an average value of 2.79 Å, corresponding to more basic Br^{a-a} connections. Only the Y5-Br1 bond, bridging to a cluster edge, exhibits a longer distance, more typical of the Y-Br distances observed around the cluster.

When all coordinating Br atoms are considered, as in Figure 21b, it is clear that the $Y_{16}Br_{36}Ir_4$ cluster unit can be derived from $M_6X^i_{12}X^a_6$ clusters, where condensation of the four Y_6Ir units necessitates increased sharing of the halogens; atoms designated Br^i and Br^a in M_6X_{18} clusters must now function both as inner and outer ligands, resulting in the observed three-fold inner edge-bridging (or tricapping) bonding mode. Also, one inner edge-bridging halogen site of the M_6X_{18} unit is now occupied instead by an Ir atom. Accordingly, the clusters possess structural characteristics commonly seen in M_6X_{18}-based compounds. Due to the relative sizes of Y and Br, the metal atoms (Y1, Y3, and Y4) are withdrawn from the Br^i_4 planes on the periphery of the cluster; in

$Y_{20}Br_{36}Ir_4$, Br^i-Y-Br^i angles range from 158.4(3)° to 162.4(3)°, comparable to the angles observed in $Zr_6I_{14}C$.[27] This trend is not observed for Y2; the geometry around Y2 is altered by the condensation of the Y_6Ir octahedra. Systematic changes in Y-Br bond lengths tend to be affected less by the bonding mode, e.g. Br^i vs. Br^a, as observed in many Zr_6X_{18}-based cluster phases, than by the position of the halogen relative to interstitial atoms (Ir). For each Y cluster atom, the longest Y-Br distance is *trans* to the Ir atom and is also in an exo (outer) position, suggesting that the Ir atom may be more effective than the halogen at interacting with the orbitals on Y.

At its most basic level, the structure of $Y_{20}Br_{36}Ir_4$ consists of distorted cubic-close-packed layers of Br and Ir atoms, with Y atoms occupying pseudo-octahedral holes between the layers. These close-packed layers lie parallel to (13 4 34), (13 4 $\overline{34}$), (4 $\overline{13}$ 34), and (4 $\overline{13}$ $\overline{34}$) planes, which correspond to the orientations of the four triangular faces of the Ir tetrahedron. The Y atoms form clusters by occupying sites adjacent to groups of Ir atoms. Other nearby octahedral holes between Br and Ir layers are also occupied by isolated Y atoms, resulting in the formation of $YBr^{ch}_{4/2}Br^{cl}_{2/2}$ infinite chains. A view parallel to these layers containing one cluster and the surrounding Br atoms plus nearby YBr_6 fragments is pictured in Figure 22. The Ir atoms are positioned slightly out of the close-packed layer closer toward each other. Similarly, the layers of Y atoms are shifted slightly toward the cluster center. These differences in interlayer spacing are offset by shifts within the layers, so that suitable bond

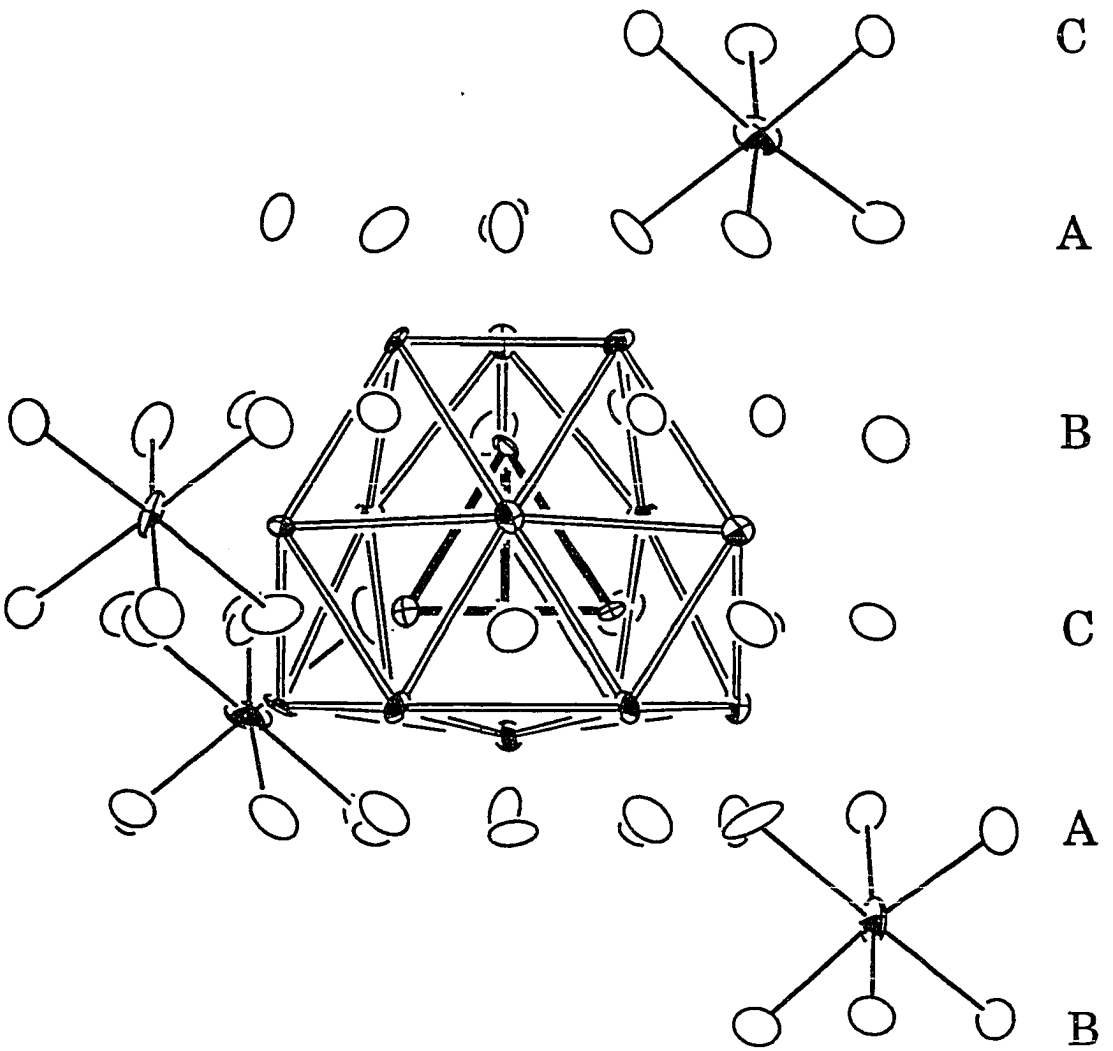

Figure 22. The $Y_{16}Ir_4$ cluster with surrounding Br atoms and adjacent $YBr_{6/2}$ octahedra viewed along the close-packed layers. Y quarter-shaded, Br open, Ir crossed.

distances and angles with the Br and Ir atoms are maintained. The shortest Br-Br contacts of 3.60(1) Å occur between Br6 atoms in adjacent close-packed layers, which cap Y triangles in hexagonal faces of neighboring clusters within the a-b plane. All other Br-Br contacts are larger than 3.70 Å, the sum of van der Waals radii. The Y5 atoms that center the YBr_6 octahedra occupy sites between each close-packed layer and are arranged in a pseudo-tetrahedral fashion around the clusters.

Each $Y_{16}Ir_4$ cluster is connected to eight neighboring clusters and four $YBr^{ch}_{4/2}Br^{cl}_{2/2}$ chains through Br bridges. Figure 23 depicts the cluster arrangement within the a-b plane at z=1/8. Each cluster is bridged to four others via $Br2^{i\text{-}a}$ and $Br2^{a\text{-}i}$ connections, creating a square network. The smallest intercluster Y-Y distance within this plane is 4.65 Å between Y4 atoms. Each cluster is related to the next by a unit cell translation of ±a and ±b and is oriented equivalently. Other symmetry-related layers of this type are located at z=3/8, 5/8, and 7/8; each layer is related to the others by alternating a- and b-glide planes. The second layer is shifted halfway along $\vec{a}$, then reflected through a mirror plane perpendicular to $\vec{c}$ at z=1/4. The resultant cluster layer is shifted by (1/2,0,1/4) from the first, with each cluster rotated by 90° around $\vec{c}$ with respect to the first layer. Similarly, a b-glide at z=1/2 relates the second layer to the third. Four such layers of clusters are included in the unit cell. This vertical stacking pattern also creates rows of clusters aligned alternately (along $\vec{c}$) within planes parallel to (100) and (010).

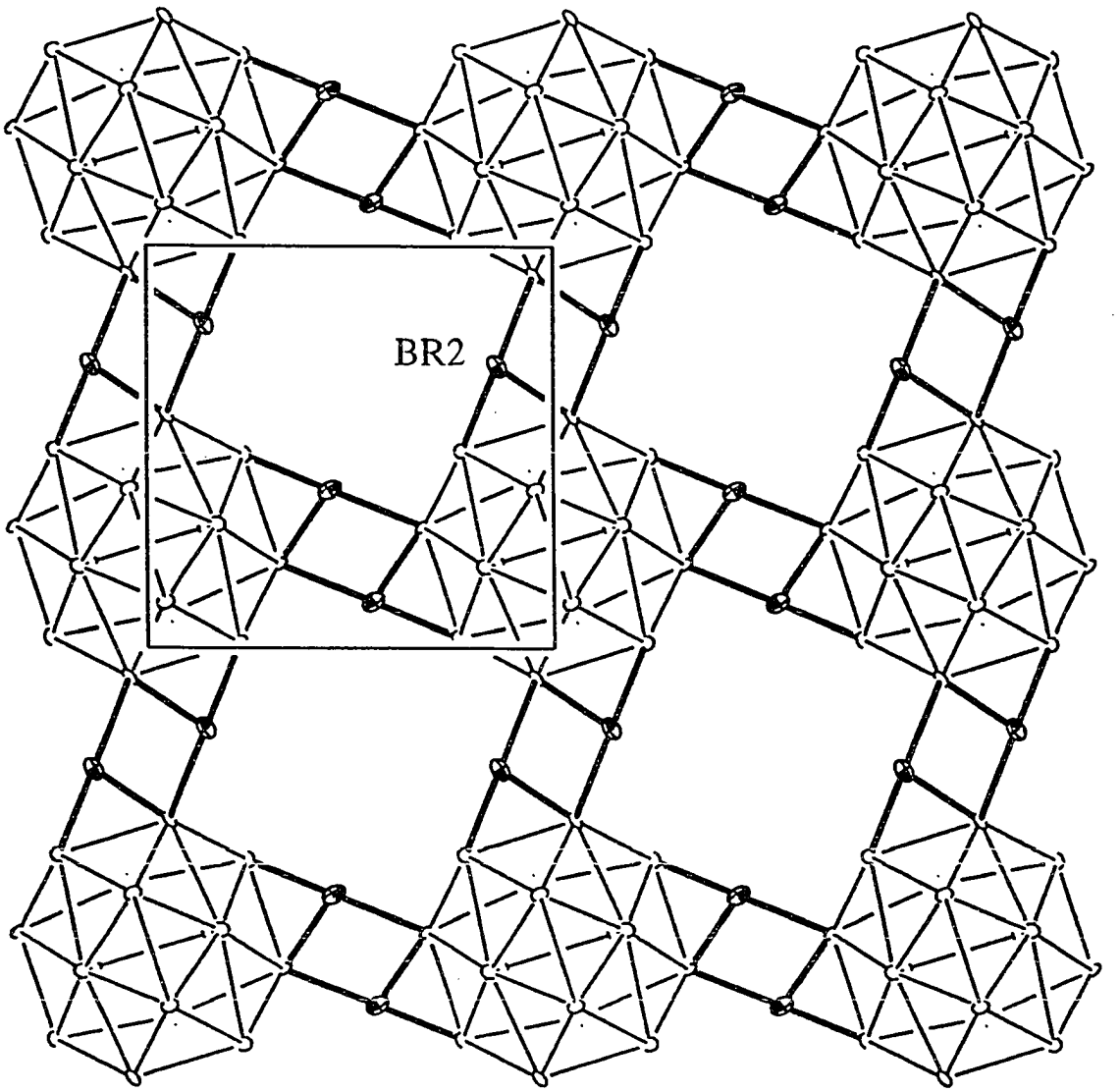

Figure 23. [00$\bar{1}$] view of the a-b plane of $Y_{20}Br_{36}Ir_4$ at z=1/8, illustrating the square cluster network. Br2 atoms bridge along $\vec{a}$ (horizontal) and $\vec{b}$ (vertical).

These square cluster layer networks are not isolated but are interconnected through two types of halogen bridges, the first connecting the clusters to $YBr^{ch}_{4/2}Br^{cl}_{2/2}$ chains via Br1 and Br7 atoms. These chains are positioned at z~0, 1/4, 1/2, and 3/4, and run between the cluster layers in the a-b plane alternately parallel to $\vec{a}$ and then $\vec{b}$; at z~0, the chains parallel $\vec{b}$, while at z~1/4 they run along $\vec{a}$. Figure 24 shows a [00$\bar{1}$] view of the cluster layer at z=1/8, with $YBr^{ch}_{4/2}Br^{cl}_{2/2}$ chains at z~1/4 running near clusters along $\vec{a}$. There are two chains below and two chains above each $Y_{16}Ir_4$ cluster; the chains are arranged in approximately tetrahedral fashion about the clusters. Figure 25 offers another view of the cluster-chain connections. The zigzag arrangement along the chain occurs in the c-direction, such that one Y_2Br_{10} "dimer" is "down" (along $\vec{c}$) and the next one is "up". Each dimer is connected to two clusters, one on each side of the chain, which will be referred to as "left" and "right". Consequently, the positions of clusters encountered as one goes along the chain are ...down-left, down-right, up-left, up-right,... . The Y5-Y5 distances along the chain are 4.05 Å and 4.08 Å within and between dimers, respectively, too long for significant bonding interactions. The shortest Y-Y distance between clusters and chains is 4.28 Å between Y5 and Y3.

The second type of interlayer connection is via Br3 atoms as shown in Figure 26a. These atoms bridge each cluster to four neighboring clusters in adjacent layers in a pseudo-tetrahedral manner and are symmetry-related by a $\bar{4}$ rotation around $\vec{c}$, as were the clusters in $Y_{16}Br_{20}Ru_4$. The intercluster Br3

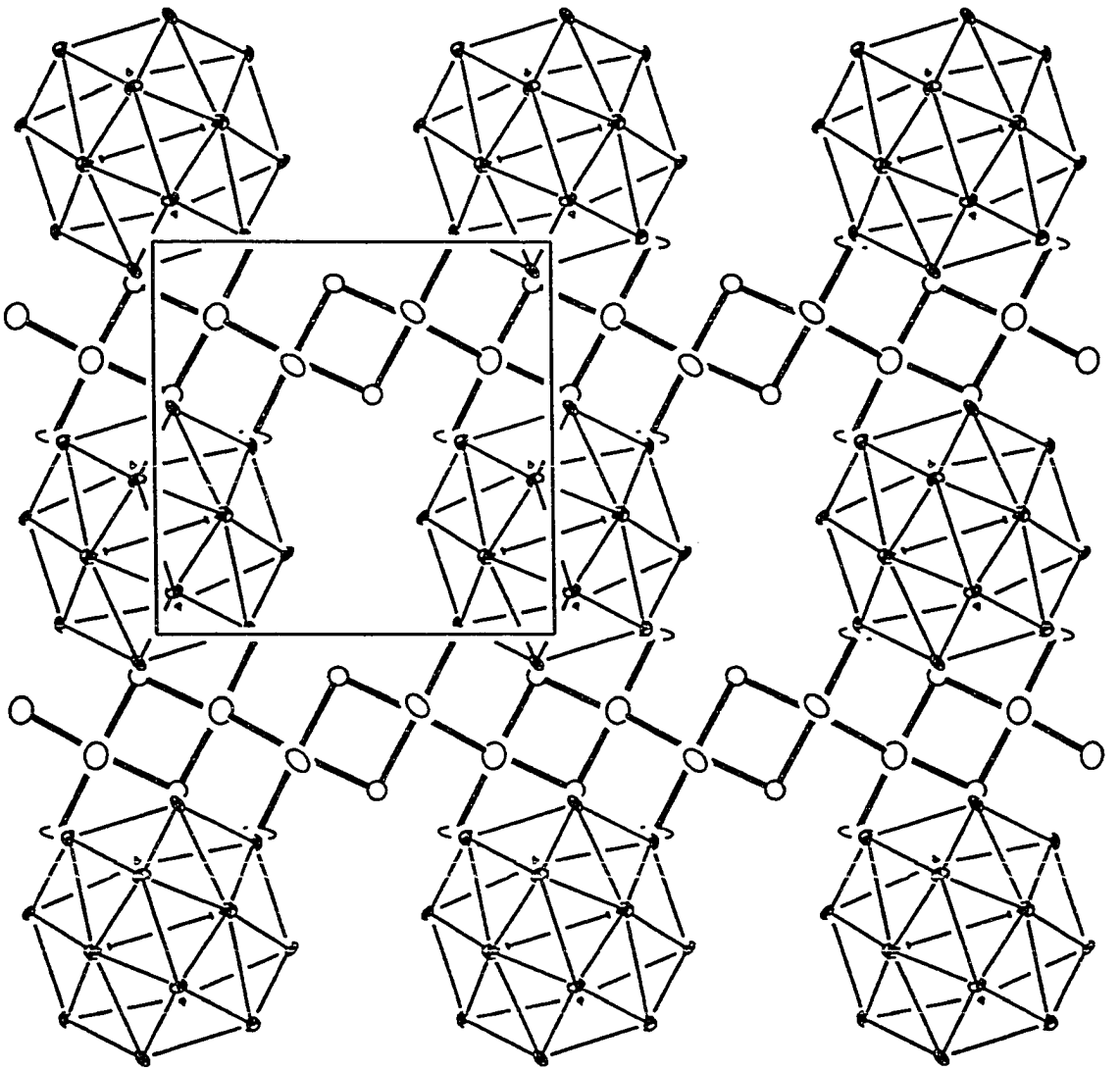

Figure 24. [00$\bar{1}$] view of the cluster layer at z=1/8, with $YBr^{ch}_{4/2}Br^{cl}_{2/2}$ chains at z~1/4 running along $\vec{a}$ (horizontal). $\vec{b}$ is vertical.

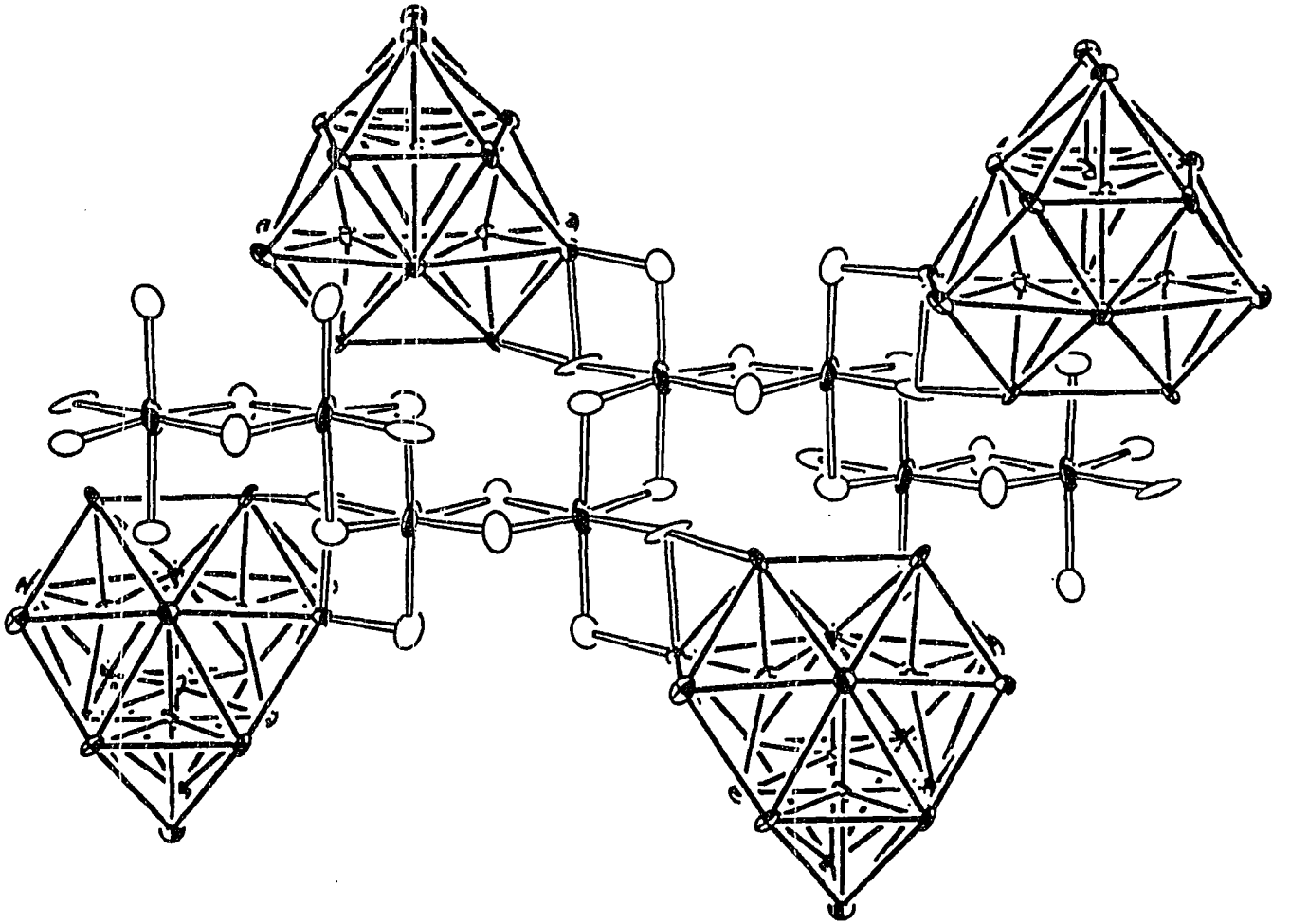

Figure 25. Illustration of the cluster-chain connectivity along the $YBr^{ch}_{4/2}Br^{cl}_{2/2}$ chain. Clusters are connected alternately on both sides of as well as above and below the chain. $\vec{c}$ is vertical.

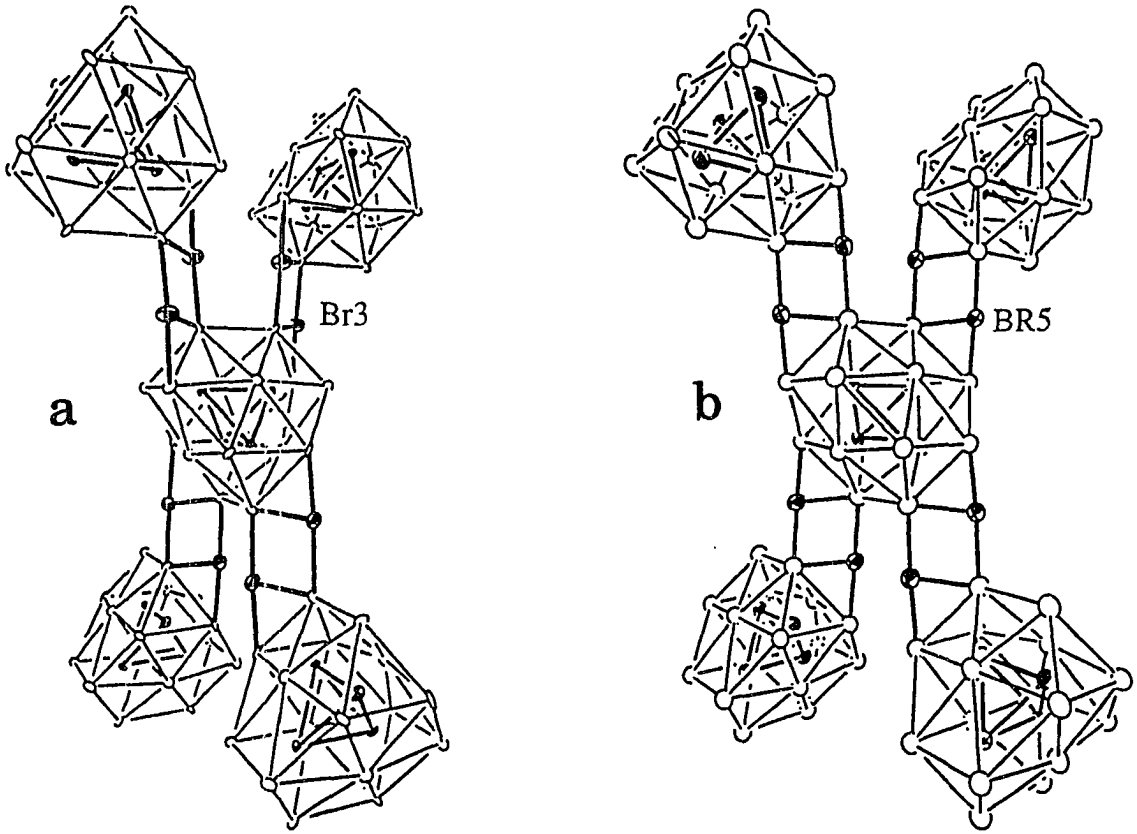

Figure 26. Comparison of interlayer halogen bridges along $\vec{c}$ via a) Br3 atoms in $Y_{20}Br_{36}Ir_4$, and b) Br5 atoms in $Y_{16}Br_{24}Ir_4$. The upper two clusters are bridged through different edges on the truncated corners of the Y tetrahedron, while the lower connections are identical. The clusters in $Y_{20}Br_{36}Ir_4$ are related by a $\bar{4}$ rotational axis, which is not present in $Y_{16}Br_{24}Ir_4$.

bridge connects one edge of the truncated corners of the Y tetrahedra (defined by Y1, Y3, and Y4) to the (Y1-Y1) edge of a neighboring cluster in a manner nearly identical to that exhibited by Br5 in $Y_{16}Br_{24}Ir_4$, pictured in Figure 26b. A comparison of Figures 26a and 26b reveals that the two lower intercluster bridges are identical, but the upper halogen bridges connect to different edges on the (Y1-Y3-Y4) truncated corner of the tetrahedron. The Y-Y intercluster distance along this bridge in $Y_{20}Br_{36}Ir_4$ is 4.56 Å between Y1 atoms, only slightly longer than that observed in $Y_{16}Br_{24}Ir_4$ (4.51 Å).

In addition to the many structural similarities noted between $Y_{20}Br_{36}Ir_4$ and $Y_{16}Br_{24}Ir_4$ or $Y_{16}Br_{20}Ru_4$, dimensional relationships based on cluster packing and intercluster bridging also exist. There is a strong relationship between the cluster packing in the a-b planes of $Y_{20}Br_{36}Ir_4$ and $Y_{16}Br_{20}Ru_4$. The a-b planes of both these phases contain rows of clusters that form square networks. As seen in Figure 27, it is possible to obtain the network found in $Y_{20}Br_{36}Ir_4$ directly from that of $Y_{16}Br_{20}Ru_4$. Pictured on the left side of the figure is the square network of $Y_{16}Ru_4$ clusters at z=3/4, along with the intercluster bridges in the a-b plane via tricapping Br1 and the edge-bridging Br2 that are involved in interlayer bonding. Rotating each cluster and the connected halogens clockwise by ~28° around $\vec{c}$ (perpendicular to the plane of the paper) results in the cluster orientations and intercluster halogen bridges present in $Y_{20}Br_{36}Ir_4$. As seen in the $Y_{20}Br_{36}Ir_4$ layer (z=1/8) on the right, the formerly interlayer-bridging Br atoms (Br2 in $Y_{16}Br_{20}Ru_4$) now bridge clusters within one layer, while the

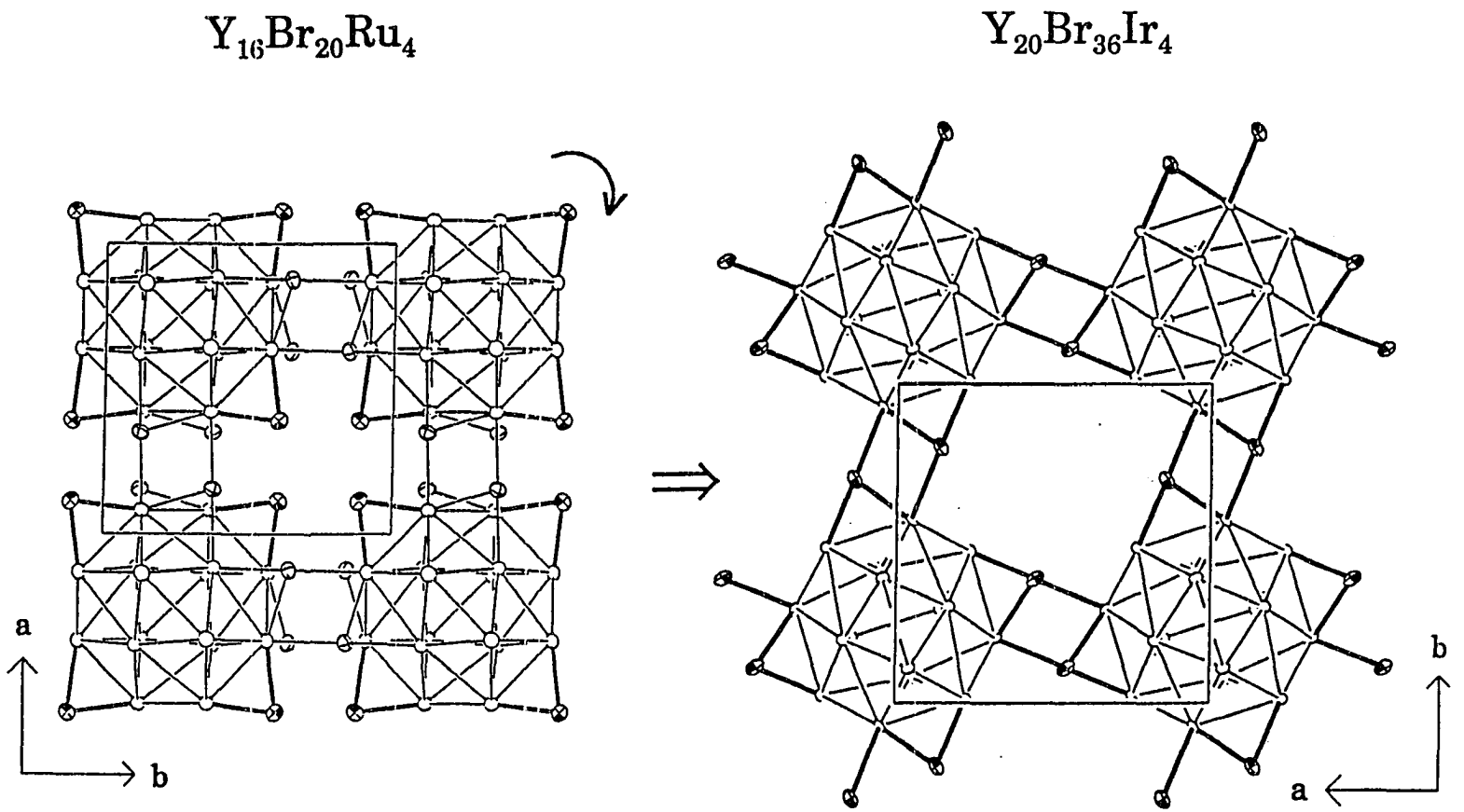

Figure 27. The structural relationship between the a-b planes of $Y_{16}Br_{20}Ru_4$ (left) and $Y_{20}Br_{36}Ir_4$ (right). Clockwise rotation of each of the $Y_{16}Ru_4$ clusters and surrounding Br atoms by ~28° results in the cluster orientation found in $Y_{20}Br_{36}Ir_4$.

tricapping Br atoms (Br1 in $Y_{16}Br_{20}Ru_4$) do not participate in intercluster bonding. This new cluster orientation and the resultant $Br^{i\text{-}a}$ and $Br^{a\text{-}i}$ bonding modes cause a 1 Å expansion of the unit cell from ~11.7 Å in $Y_{16}Br_{20}Ru_4$ to ~12.7 Å in $Y_{20}Br_{36}Ir_4$. A second relationship exists between the unit cell lengths along $\vec{c}$ of $Y_{20}Br_{36}Ir_4$ and $Y_{16}Br_{24}Ir_4$, due to the similarity in interlayer Br bridges discussed earlier. The unit cells of both phases include four cluster layers and four interlayer halogen bridges. Consequently, the c-axis lengths of the two phases are very similar.

Magnetic susceptibility measurement

Based on the formula $Y_{20}Br_{36}Ir_4$, each $Y_{16}Ir_4$ cluster formally has 60 electrons available for metal-metal bonding, as was the case for $Y_{16}(Br,I)_{20}Ru_4$ and $Y_{16}Br_{24}Ir_4$. This 60 electron count seems to correspond to a very stable closed-shell orbital configuration, apparently present in all the $Y_{16}Z_4$-containing phases. The addition of isolated Y atoms to the phase does not change the overall electron count; enough additional Br atoms were also incorporated into the structure to "soak up" the extra electrons with Y-Br bonding. To confirm this experimentally, magnetic susceptibility measurements were performed on a powdered sample of >80% $Y_{20}Br_{36}Ir_4$, as judged from Guinier powder pattern. Also present were small amounts of YBr_3 and $AlBr_3$. The data, presented in Figure 28, exhibit nearly temperature-independent paramagnetism, after addition of a substantial diamagnetic core correction (-1.736×10^{-3} emu/mol). The presence of a supposed Curie tail at T< 60K is most likely due to a

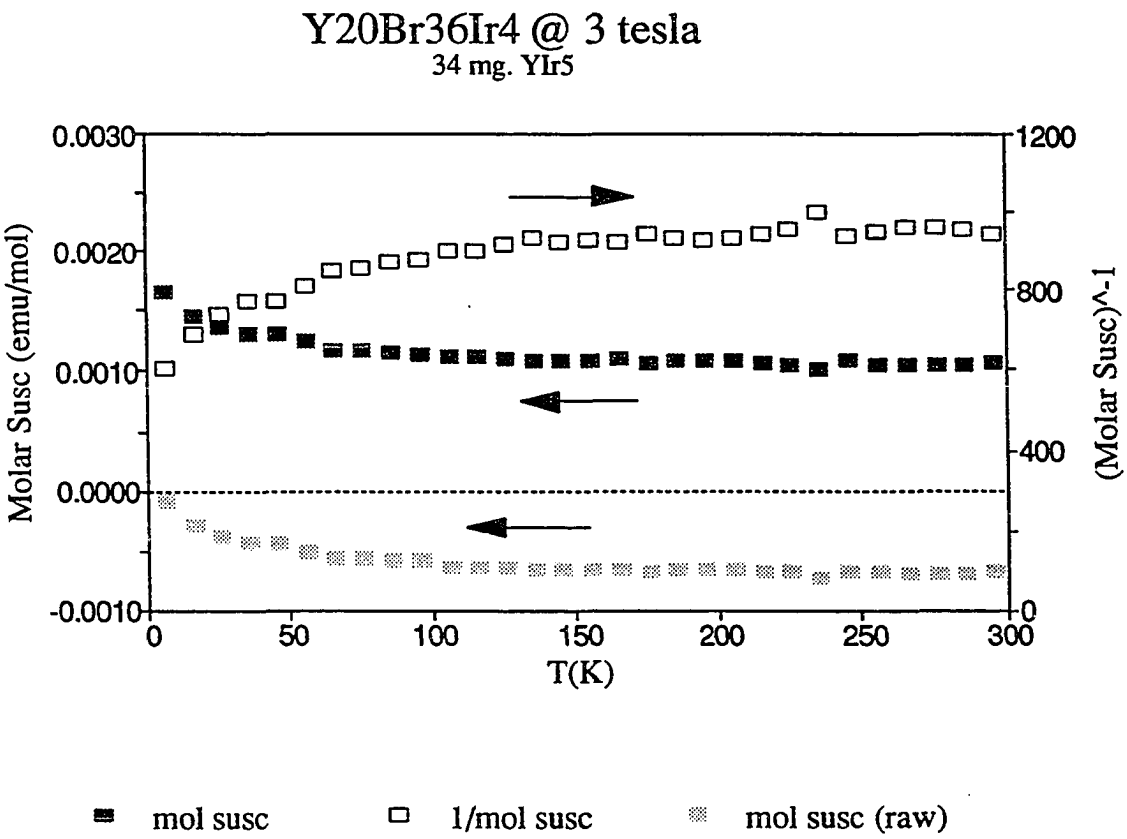

Figure 28. A plot of the magnetic susceptibility as a function of temperature for $Y_{20}Br_{36}Ir_4$ at 3 T. The magnitude of the diamagnetic core correction is indicated.

paramagnetic impurity. Although the compound might be expected to exhibit diamagnetism, the observed behavior is not inconsistent with a closed-shell configuration. Similar temperature-independent paramagnetism has often been observed in metal halide cluster compounds.[90] This characteristic magnetic behavior can be attributed to intrinsic van Vleck paramagnetism,[91] which results from a mixing of excited state wave functions with those of the ground state in the presence of a magnetic field. In this phase, the molar susceptibility at 300 K is 1.06 x 10^{-3} emu/mol.

Other synthetic attempts

In addition to the Y–Br–Ru and Y–Br–Ir systems, several reactions were attempted with other prospective interstitial elements. While some syntheses produced new phases based on Guinier powder pattern results, their structural characterization was not possible due to the lack of suitable single crystals. Exploratory synthesis over a temperature range of 900° C to 980° C in the Cr, Mn, and Re systems resulted in the formation of intermetallic phases (Re–Y) and/or unreacted metal (Cr, Mn, Y) along with YOBr and the starting material YBr_3. Reactions loaded with Pt (~Y_3Br_3Pt) produced a new phase, which formed as shiny, golden, hard chunks but whose powder pattern did not match any of the known intermetallic phases. XPS measurements confirmed the presence of Pt in the material and ruled out Nb contamination from the reaction container. In metal-rich reactions (~Y_2Br_2Fe) with Fe as an interstitial, a new phase was formed as black needles. The powder pattern resembled those displayed by

layered compounds of the type Gd_2Cl_2C[45] and Gd_2Br_2C,[97] but some of the important characteristic lines of these structure types were not observed. Reactions with Ni as an interstitial produced a moderate yield (~40%) of black rods and chunks of a phase whose powder pattern resembled that of $Y_6I_{10}Ru$; several strong lines seemed consistent with this structure type, but many weaker lines were absent. No single crystals of any of these phases were obtained.

$Sc_{20-x}Br_{28}(Os,Ru,Fe,Mn)_4$ and Related Phases

The stability and versatility of the $M_{16}Z_4$ unit is apparent from the variety of structure types that contain the unit and the range of elements incorporated into the oligomeric clusters. Several different rare-earth metals have been shown to form $M_{16}Z_4$ clusters interstitially stabilized by elements from group 7 through group 9 of the periodic table and coordinated by either Br or I ligands. The most prolific of the known structures that contain $M_{16}Z_4$ clusters was first discovered for $Gd_{20}I_{28}Mn_4$[63] and has since been observed in the La–I system[98] and the Sc–Br system stabilized by a variety of interstitial elements.

Prior to this study, the Sc–Br–Z systems were unexplored, with previous research efforts focusing on the chloride and iodide systems. Several novel reduced Sc chloride phases were prepared, including Sc_4Cl_6B, Sc_5Cl_8C, $Sc_7Cl_{10}C_2$, and $Sc_7Cl_{12}Z$ (Z = B, C, N)[17,99]. The iodide system also provided new and unique compounds including $Sc_6I_{11}C_2$[53] and $Sc_7I_{12}Z$ (Z = B, C, Co, Ni).[100] The smaller halogen (Cl) stabilized compounds exhibited more structural diversity than was

seen for I, while the iodides were able to incorporate 3d transition metals as interstitials. It seemed probable that new phases would exist with an intermediately sized halogen, which might exhibit new structures as well, as was the case for Y_4Br_4Os.[41] With this goal in mind, exploratory synthesis incorporating a wide range of interstitials was initiated.

Synthesis

Initial reactions in the Sc–Br–Z systems were very encouraging in that many new phases were prepared, even though several of these remain uncharacterized. Synthetic attempts concentrated largely on incorporating transition metals as interstitials; reactions were loaded with a variety of transition metals, twelve in all, as well as C and B. The reactions were heated gradually up to the chosen reaction temperature over a period of several days in an attempt to minimize the number of crystal nuclei formed and thereby obtain large, high quality single crystals. ScOBr was observed in all reaction products in the form of light pink transparent blades which were often attached to the reaction tube wall; the use of higher temperatures or reloading reaction products for further reaction resulted in a larger amount of the phase.

Reactions loaded with Os as an interstitial yielded five new phases, based on Guinier powder pattern results; formation of these compounds was dependent on both composition and reaction temperature. A reaction loaded as Sc_4Br_5Os and heated at 950° C for 2 weeks yielded approximately equal parts of $Sc_{20-x}Br_{28}Os_4$ and an unidentified phase, referred to as "S5", which has an estimated

composition near Sc_4Br_4Os. The two phases have very distinctive crystal habits; $Sc_{20-x}Br_{28}Os_4$ forms as black cubes or bricks, while "S5" appears as long fibrous black needles. A less reduced reaction composition ($Sc_6Br_{11}Os$) heated at the same temperature yielded mostly $Sc_{20-x}Br_{28}Os_4$ and $ScBr_3$ with just a trace of "S5". Several reactions were loaded with the composition $Sc_{19}Br_{28}Os_4$ and heated over a series of different temperatures for 20 days or more; at 975° C, the products were "S5" and $ScBr_3$, while equilibrations at 900° C and 850° C gave a nearly quantitative yield of $Sc_{20-x}Br_{28}Os_4$ with a minute trace of "S5" (identified visually in the sample), and a reaction heated at 800° C yielded only $Sc_{20-x}Br_{28}Os_4$. More reduced stoichiometries produced two different phases; a reaction loaded as Sc_3Br_2Os and heated at 850° C for 26 days consisted of ~50% $Sc_{16}Br_{20}Os_4$ (isostructural with $Y_{16}Br_{20}Ru_4$ based on the powder pattern), with minor amounts of a second unknown, "SOs6", and $Sc_{11}Os_4$. Heating a similarly metal-rich reaction at 950° C for two weeks again yielded "S5" along with "SOs6" and $Sc_{11}Os_4$. Addition of NaBr to the reaction (in the composition $NaSc_4Br_4Os$) produced, in addition to intermetallics and Na–Sc–Br ternary phases, a fifth phase in the form of black, matted needles and fibers, which exhibited an intense broad low angle line in the powder pattern and was stable at both 840° C and 950° C. The lattice parameters of $Sc_{16}Br_{20}Os_4$ as determined based on 34 Guinier powder pattern lines indexed to a tetragonal cell with a=11.116(1) Å, and c=16.124 Å.

The Sc–Br–Ru system seems to contain four phases, one of which has been structurally characterized. A reaction loaded as Sc_4Br_5Ru and heated to 900° C produced well-formed cubes of $Sc_{20-x}Br_{28}Ru_4$ in addition to $ScBr_3$ and an unidentified phase. Reactions loaded as $Sc_{19}Br_{28}Ru_4$ produced >85% $Sc_{20-x}Br_{28}Ru_4$ when heated at 900° C, but heating at 975° C decomposed the phase to the starting materials. More metal-rich compositions heated at 950° C produced moderate amounts (~30%) of two different unidentified phases in addition to $Sc_{20-x}Br_{28}Ru_4$. Reactions loaded with alkali metal ($NaSc_4Br_4Ru$) gave only $ScBr_3$ and Na–Sc–Br ternary phases as products.

Exploratory synthesis in the Sc–Br–Fe system resulted in the preparation of two new phases, $Sc_{20-x}Br_{28}Fe_4$ and $Sc_{16}Br_{20}Fe_4$, which both contain $Sc_{16}Fe_4$ clusters. A reaction loaded as $Sc_{19}Br_{28}Fe_4$ and heated at 950° C for 20 days gave >90% of $Sc_{20-x}Br_{28}Fe_4$. Reactions loaded more metal-rich (ranging from Sc_4Br_5Fe to $Sc_2Br_2Fe_2$) yielded a mixture of mostly $Sc_{20-x}Br_{28}Fe_4$ with a small amount (≤20%) of $Sc_{16}Br_{20}Fe_4$ (isostructural with $Y_{16}Br_{20}Ru_4$) and, in the most reduced cases, Fe–Sc inter-metallic phases. Addition of NaBr to the reaction ($NaSc_4Br_4Fe$) produced a 60% yield of $Sc_{16}Br_{20}Fe_4$ along with Sc metal and Na–Sc–Br ternary phases when heated at 840° C for 24 day; further heating of this reaction product at 950° for 20 more days caused the cluster phase to decompose to $ScBr_3$ and Fe. As was seen in the Y–Br–Z systems (for $Y_{16}Br_{24}Ir_4$), the presence of alkali metals in the reaction results in the formation of Na–Sc–Br ternary phases, which presumably act as a flux to enhance the

formation of one cluster phase over that of another. Based on 22 Guinier powder pattern lines, the lattice parameters of $Sc_{16}Br_{20}Fe_4$ index to a tetragonal cell with a=10.996(1) Å, c=16.021(4) Å, slightly smaller than observed for the Os analogue.

After the preparation of $Sc_{20-x}Br_{28}(Os,Ru,Fe)_4$, attempts were made to synthesize the analogous Mn phase. Reactions loaded as Sc_5Br_7Mn were heated for 20 days or more at temperatures ranging from 725° C to 950° C. Reactions heated at 800° C or 850° C produced a moderate (~35%) to small amount of black crystalline $Sc_{20}Br_{28}Mn_4$, a small amount of Mn_2Sc, and a large quantity of black fibrous material (commonly resembling "mouse fur") whose powder pattern matched that reported for Sc_2Br_3.[101] Reactions heated at both higher and lower temperatures resulted in only Sc_2Br_3 and Mn_2Sc. Addition of NaBr (loaded as $NaSc_4Br_4Mn$) to a reaction heated at 840° C for 25 days yielded only $ScBr_3$, Mn metal and Na–Sc–Br ternary phases.

Preliminary reactions in the Sc–Br–Ir system have produced three new phases. A reaction loaded as $Sc_6Br_{11}Ir$ and heated at 950° C for two weeks produced (~25%) thin black needles along with both $ScBr_3$ and IrSc. This new Ir-containing phase, designated "S5'", exhibited a powder pattern very similar to that observed for S5 (Os system), except with the line positions slightly shifted. The yield of S5' increased to 50% in a reaction with the loaded composition of Sc_4Br_5Ir and heated in the same manner. Again, this material formed as thin black needles in the presence of IrSc and a small amount (~10%) of $ScBr_3$. Oscillation photographs of a selection of these fibrous crystals

indicated a cell length of ~9 Å along the needle direction, but the crystal quality was poor; all the spots were badly streaked. A reaction loaded slightly more metal-rich (Sc_4Br_4Ir), when heated at 800° C for 20 days, gave S5' and a second unidentified phase in nearly equal yield, suggesting that the reaction temperature was a significant factor. A third unknown phase was formed when NaBr was added to the reaction (loaded as $NaSc_4Br_4Ir$). The powder pattern of this phase matched that exhibited by an unknown in the analogous Os reaction, with the lines shifted to slightly lower angles than in the Os case. Unfortunately, no good single crystals of either of these phases were obtained.

Reactions involving Co and Ni metal as a source of interstitial produced the phases $Sc_7Br_{12}Co$ and $Sc_7Br_{12}Ni$ in moderate to high yield. A reaction loaded as Sc_4Br_4Co and heated at 950° C for two weeks gave a high yield of $Sc_7Br_{12}Co$, with $CoSc_2$ and CoSc as products also, while heating a stoichiometric reaction ($Sc_7Br_{12}Co$) at 850° C for 26 days gave a slightly lower yield of $Sc_7Br_{12}Co$, with leftover $ScBr_3$ and an unidentified phase. Reactions loaded as Sc_4Br_5Ni and $Sc_7Br_{12}Ni$ and heated at 850° C for over 25 days both yielded $Sc_7Br_{12}Br$; the former reaction also contained a moderate (30%) amount of intermetallics (NiSc, $NiSc_2$), while the latter contained small amounts of both $ScBr_3$ and NiSc. The lattice parameters of $Sc_7Br_{12}Co$ (space group $R\bar{3}$) indexed to a cell with a=13.795(1) Å, c=9.585(1) Å, based on 27 Guinier powder pattern lines. Cell parameters of the analogous Ni phase are a=13.795(2) Å, c=9.493(1) Å, obtained from 23 Guinier powder pattern lines. The length of the a-axis is identical for

both phases, while the c-parameter is slightly larger for the Co phase as expected based on the atomic radii. The c/a ratios of these two phases are similar to those observed in the isostructural (Sc) iodide phases, whose clusters also possess both 18 and 19 electron counts.

Attempts to incorporate other transition metals were less successful. Reactions with Z = Cr, Cu, Rh, and Pt at 850° C or higher yielded mostly $ScBr_3$ and intermetallics or unreacted (Z) metal and occasionally Sc_2Br_3. A reaction with Pt (loaded Sc_4Br_5Pt) was heated at 775° C and produced >50% of an unknown phase in addition to PtSc. A reaction loaded Sc_4Br_5Re and heated at 850° C for 10 weeks gave a new phase that formed as black fibrous needles (mouse fur) and exhibited two low angle lines in the Guinier powder pattern. When heated at 975° C for 20 days, this phase decomposed to $ScBr_3$ and Re_2Sc along with a second unknown phase.

A few attempts to incorporate main group elements were also made. Reactions with compositions near Sc_4Br_5C were heated at 900° C and yielded $Sc_7Br_{12}C$[92] and three other unidentified phases, which again grew as black fibrous material. Reactions loaded in similar ratios with B as a prospective interstitial resulted in two new phases, which form as black powder at both 850° C and 950° C, along with $ScBr_3$ and ScB_2. One of these phases exhibits a powder pattern that closely resembles that of $Sc_6I_{11}C_2$.[53]

Structure determinations

A black cube picked from a reaction loaded as Sc_5Br_7Os was used for the

single crystal structure determination of $Sc_{20-x}Br_{28}Os_4$. A summary of data collection and refinement parameters is given in Table 18. Data collection was performed at room temperature on a Enraf Nonius CAD-4 automated diffractometer using Mo Kα radiation. A random search located reflections that indexed to a primitive cubic cell. The diffractometer programs identified the Laue class as $m\bar{3}m$. A hemisphere (±h, k, ±l) of data was collected between the 2θ limits of 1° and 50°, followed by measurement of three psi scans which exhibited a transmission range of 0.418–1.000.

Structure solution began with data reduction, which included Lorentz-polarization corrections and an empirical absorption correction based on an averaged transmission curve. Intensity statistics strongly indicated a noncentrosymmetric space group. No extinction conditions were present in the data, so the acentric space group $P\bar{4}3m$ was chosen for the refinement. Direct methods (SHELXS-86) readily provided a solution containing three Sc atoms, three Br atoms and one Os atom. Isotropic refinement of the model resulted in a reasonable R-value, but the thermal parameters were very small and even went negative for the Os atom. Anisotropic refinement gave R=0.032 and R_w=0.035 but did not solve the temperature factor problem. After application of a spherical 2θ-dependent absorption correction and subsequent data reduction with the CHES program,[93] the thermal parameters were more reasonable and isotropic refinement gave R and R_w values of 0.038. However, the resultant thermal parameter of Sc3 was over three times larger than those of the other Sc

Table 18. Crystallographic data for $Sc_{18.9(1)}Br_{28}Os_4$

Crystal data	
Formula	$Sc_{4.72(3)}Br_7Os$
Space group, Z	$P\bar{4}3m$, 4
a (Å)[a]	11.0032(3)
V (Å^3)	1332.2(1)
D_{calc} (g/cm^3)	4.795
μ (Mo Kα, cm^{-1})	325.52
Data collection	
Crystal dimensions, mm	0.20 x 0.20 x 0.20
Diffractometer	Rigaku AFC6R
Radiation, wavelength (Å)	Mo Kα, 0.71069
Scan mode	ω
Octant measured	±h, k, ±l
$2\theta_{max}$, deg.	50
Refinement	
No. of measured reflections	4981
No. of independent refl.	489
No. of indep. refl. ($I \geq 3\sigma_I$)	422
No. of variables	33
Transmission coeff. range	0.418 - 1.000
Secondary extinction coeff.	9(3) x 10^{-9}
R_{avg} (I>0)	0.066
R, R_w	0.0347, 0.0338
Largest residual peak, e/Å^3	1.44 (1.00 Å from Os), -1.10

[a] Guinier cell constants from 32 lines.

atoms; refinement of the multiplicity of this site with the B fixed indicated that the position was less than fully occupied (the occupancy differed from 100% by over 6σ). By refining the thermal parameter and the multiplicity of this atom, the isotropic refinement converged at R=0.0374, R_w= 0.0352. Anisotropic refinement proceeded smoothly and the last cycle converged with R=0.0347 and R_w=0.0338. The final occupancy of Sc3 refined to 72(3)%, giving a composition of $Sc_{18.9(1)}Br_{28}Os_4$. The largest positive and negative peaks in the final difference Fourier map were 1.44 e/Å^3, located 1.00 Å from Os, and -1.10 e/Å^3. Table 19 lists the positional and anisotropic thermal parameters for the phase. The powder pattern calculated from the model is in excellent agreement with the observed powder pattern. Lattice parameters were determined based on 45 Guinier powder pattern lines.

The structure determination of $Sc_{20-x}Br_{28}Ru_4$ was accomplished with a crystal from a reaction loaded as Sc_4Br_5Ru. Table 20 lists important data collection and refinement parameters. Room temperature data were collected on a Rigaku AFC6R diffractometer. A random search procedure located 24 peaks that indexed to a primitive cubic cell. The diffractometer programs identified the Laue class as $m\bar{3}m$. An octant (h, k, l) of data was collected between the 2θ limits of 1° and 70°, followed by measurement of three psi scans which resulted in a transmission range of 0.516–1.000.

After data reduction including Lorentz-polarization corrections and an empirical absorption correction based on the averaged transmission curve, the

Table 19. Positional and thermal parameters for $Sc_{18.9(1)}Br_{28}Os_4$

Atom	Type	x	y	z	B_{eq}	U_{11}	U_{22}	U_{33}	U_{12}	U_{13}	U_{23}
Os	4e	0.0973(1)	x	x	1.1782(4)	0.014921(5)	U_{11}	U_{11}	-0.0006(5)	U_{12}	U_{12}
Sc1	12i	0.1169(3)	x	0.3286(4)	1.4(1)	0.021(2)	U_{11}	0.013(2)	0.002(2)	-0.001(1)	U_{13}
Sc2	4e	-0.1386(5)	x	x	1.552(2)	0.01965(3)	U_{11}	U_{11}	0.002(2)	U_{12}	U_{12}
Sc3[1]	4e	0.3840(4)	x	x	1.714(4)	0.02170(5)	U_{11}	U_{11}	-0.001(3)	U_{12}	U_{12}
Br1	12i	0.1274(1)	x	0.6027(2)	1.55(6)	0.0201(9)	U_{11}	0.019(1)	-0.001(3)	0.0007(8)	U_{13}
Br2	12i	0.3651(1)	x	0.1259(2)	1.88(7)	0.022(1)	U_{11}	0.029(2)	0.001(1)	0.0026(8)	U_{13}
Br3	4e	-0.3735(3)	x	x	2.55(1)	0.03231(2)	U_{11}	U_{11}	-0.001(1)	U_{12}	U_{12}

[1] Occupancy of Sc3 was refined to 0.72(3)

Table 20. Crystallographic data for $Sc_{18.96(8)}Br_{28}Ru_4$

Crystal data	
Formula	$Sc_{4.74(2)}Br_7Ru$
Space group, Z	$P\bar{4}3m$, 4
a (Å)[a]	10.9897(5)
V (Å^3)	1327.26(6)
D_{calc} (g/cm^3)	4.3709
μ (Mo Kα, cm^{-1})	242.24
Data collection	
Crystal dimensions, mm	0.17 x 0.22 x 0.25
Diffractometer	Rigaku AFC6R
Radiation, wavelength (Å)	Mo Kα, 0.71069
Scan mode	ω
Octant measured	h, k, l
$2\theta_{max}$, deg.	70
Refinement	
No. of measured reflections	3338
No. of independent refl.	653
No. of indep. refl. ($I \geq 3\sigma_I$)	394
No. of variables	33
Transmission coeff. range	0.871 - 1.095
Secondary extinction coeff.	1.8(1) x 10^{-7}
R_{avg} ($I>0$, $I \geq 3\sigma_I$)	0.235, 0.076
R, R_w	0.0420, 0.0375
Largest residual peak, e/Å^3	3.26 (2.28 Å from Br1), -2.26

[a] Guinier cell constants from 28 lines.

data with I>0 were averaged in $P\bar{4}3m$. Using the atomic positions of $Sc_{20-x}Br_{28}Os_4$ as an initial model, the isotropic refinement proceeded smoothly to values of R=0.054 and R_w= 0.066. As seen in $Sc_{20-x}Br_{28}Os_4$, the thermal parameter for Sc3 refined to a value three to four times larger than the thermal parameters of the other Sc atoms. Refinement of the multiplicity of this position while fixing the thermal parameter indicated that the site was partially occupied (the occupancy differed from 100% by 5σ). By refining the multiplicity and thermal parameter of this atom, the multiplicity settled near 79% occupancy and gave more reasonable Sc thermal parameters, although the B for Sc3 was still larger than for the other two Sc atoms. Isotropic refinement with this new multiplicity converged with an R=0.051 and R_w=0.062. Anisotropic refinement was uneventful; the last cycle converged at R=0.043 and R_w=0.056. Refinement after application of a DIFABS absorption correction gave slightly better results, with R=0.042 and R_w= 0.0375 and a final refined composition of $Sc_{18.96(8)}Br_{28}Ru_4$. The largest positive and negative peaks in the final difference Fourier calculation were 3.26 e/Å^3, located 2.28 Å from Br1, and -2.26 e/Å^3; the largest peaks, which were located at higher symmetry sites, did not stand out considerably from the background. Rather, there was a relatively steady decrease observed in the intensity of the difference peaks. Table 21 lists the positional and anisotropic thermal parameters for this phase. The powder pattern calculated from the model is in excellent agreement with the observed

Table 21. Positional and thermal parameters for $Sc_{19.0(1)}Br_{28}Ru_4$

Atom	Type	x	y	z	B_{eq}	U_{11}	U_{22}	U_{33}	U_{12}	U_{13}	U_{23}
Ru	4e	0.0990(1)	x	x	0.3099(4)	0.003925(5)	U_{11}	U_{11}	-0.0003(5)	U_{12}	U_{12}
Sc1	12i	0.1171(2)	x	0.3284(3)	0.57(6)	0.008(1)	U_{11}	0.005(1)	0.000(1)	0.0024(8)	U_{13}
Sc2	4e	-0.1381(3)	x	x	0.376(1)	0.00477(1)	U_{11}	U_{11}	-0.001(1)	U_{12}	U_{12}
Sc3[1]	4e	0.3821(4)	x	x	0.915(2)	0.01159(2)	U_{11}	U_{11}	-0.002(2)	U_{12}	U_{12}
Br1	12i	0.1282(1)	x	0.6031(2)	0.83(4)	0.0123(6)	U_{11}	0.0070(9)	-0.0006(7)	0.0016(4)	U_{13}
Br2	12i	0.3643(1)	x	0.1246(2)	1.12(4)	0.0120(6)	U_{11}	0.018(1)	-0.0012(7)	0.0042(6)	U_{13}
Br3	4e	-0.3739(2)	x	x	1.785(1)	0.02260(1)	U_{11}	U_{11}	-0.0028(9)	U_{12}	U_{12}

[1] Occupancy of Sc3 was refined to 0.74(2)

powder pattern. Lattice parameters were calculated with the LATT program from 28 Guinier powder pattern lines.

A single crystal study of $Sc_{20-x}Br_{28}Mn_4$ was performed on a black crystal taken from a reaction loaded as Sc_5Br_7Mn. Table 22 lists important data collection and refinement parameters. The data were collected on an Enraf-Nonius CAD-4 diffractometer at room temperature. A random search procedure located reflections that indexed to a primitive cubic cell; the Laue class was determined to be $m\bar{3}m$. One octant of data was collected between the 2θ limits of 4° and 56°, followed by measurement of three psi scans which displayed a transmission range of 0.474-1.000. Following data reduction and the application of an empirical absorption correction based on the averaged transmission curve, the data with I>0 were averaged in $P\bar{4}3m$ to yield R_{avg}=0.094. The positional parameters for $Sc_{20-x}Br_{28}Os_4$ were used as an initial model. Isotropic refinement gave an R of 0.047 and R_w of 0.054 with a somewhat large thermal parameter for Sc3 (twice as large as for the other Sc atoms). Refinement of the multiplicity of Sc3 with the thermal parameter fixed resulted in a smaller occupancy of the position, but still within 3σ of 100% implying that the site should be fully occupied. However, refinement of the multiplicity and B together reduced the R to 0.045 and 0.052 and resulted in 89(2)% occupancy of the position with the B value still notably larger than those of Sc1 or Sc2 atoms. Anisotropic refinement with the occupancy fixed at 100% proceeded smoothly to yield an R= 0.040 and R_w=0.043. Anisotropic refinement with the Sc3 multiplicity varied

Table 22. Crystallographic data for $Sc_{19.56(8)}Br_{28}Mn_4$

Crystal data	
Formula	$Sc_{4.89(2)}Br_7Mn$
Space group, Z	$P\bar{4}3m$, 4
a (Å)[a]	10.941(9)
V (Å^3)	1310(1)
D_{calc} (g/cm^3)	4.227
μ (Mo Kα, cm^{-1})	244.1
Data collection	
Crystal dimensions, mm	0.28 x 0.27 x 0.19
Diffractometer	Enraf Nonius CAD-4
Radiation, wavelength (Å)	Mo Kα, 0.71069
Scan mode	ω
Octant measured	h, k, l
$2\theta_{max}$, deg.	56
Refinement	
No. of measured reflections	1820
No. of independent refl.	438
No. of indep. refl. ($I \geq 3\sigma_I$)	304
No. of variables	33
Transmission coeff. range	0.474 - 1.000
Secondary extinction coeff.	7.1(4) x 10^{-7}
R_{avg} ($I>0$, $I \geq 3\sigma_I$)	0.094, 0.061
R, R_w	0.0371, 0.0432
Largest residual peak, e/Å^3	1.78 (0.87 Å from Sc3), -1.55

[a] Guinier cell constants from 13 lines.

also gave R= 0.037 and R_w= 0.043. The largest positive and negative peaks in the difference Fourier calculation were 1.78 e/Å^3, located 0.87 Å away from Sc3, and -1.55 e/Å^3. Positional and anisotropic thermal parameters are given in Table 23. It is difficult to judge whether the partial occupancy is truly significant or is just an artifact of the refinement, especially considering the proximity of the largest residual electron density peak to Sc3. Sc is the lightest element in the structure, and the Sc3 atom would be expected to have a larger thermal parameter just based on its environment within the structure. If the partial occupancy is real, the composition of the phase is $Sc_{19.56(8)}Br_{28}Mn_4$, which is closer to the parent Gd compound than was observed for the Os and Ru phases. The powder pattern calculated from the structure model agrees very well with the observed powder pattern. Lattice parameters were determined from 13 lines in a multiphase Guinier powder pattern.

The lattice parameters and cell volume of the four $Sc_{20-x}Br_{28}Z_4$ phases follow the trend Os>Ru>>Mn>Fe as predicted by Pauling's single bond radii. A summary of bond distances and angles for the Os, Ru, and Mn phases is listed in Tables 24, 25, and 26.

Structure description

The structure of $Sc_{20-x}Br_{28}Z_4$, as for $Gd_{20}I_{28}Mn_4$, is built of two basic units, the first being $Sc_{16}Z_4$ oligomeric clusters similar to those seen in the previous sections. The second unit consists of a Sc_4Br_8 fragment, made up of a tetrahedron of Sc atoms that are coordinated by Br atoms. The $Sc_{16}Z_4$ clusters are

Table 23. Positional and thermal parameters for $Sc_{19.56(8)}Br_{28}Mn_4$

Atom	Type	x	y	z	B_{eq}	U_{11}	U_{22}	U_{33}	U_{12}	U_{13}	U_{23}
Mn	4e	0.0900(3)	x	x	1.348(1)	0.01706(2)	U_{11}	U_{11}	0.003(1)	U_{12}	U_{12}
Sc1	12i	0.1162(3)	x	0.3246(3)	1.04(7)	0.015(1)	U_{11}	0.009(2)	0.003(2)	0.002(1)	U_{13}
Sc2	4e	-0.1429(4)	x	x	1.422(2)	0.01800(2)	U_{11}	U_{11}	0.007(2)	U_{12}	U_{12}
Sc3[i]	4e	0.3839(4)	x	x	1.698(2)	0.02149(3)	U_{11}	U_{11}	0.002(2)	U_{12}	U_{12}
Br1	12i	0.1282(1)	x	0.6017(2)	1.13(4)	0.0159(7)	U_{11}	0.011(1)	-0.0003(9)	0.0022(5)	U_{13}
Br2	12i	0.3650(1)	x	0.1260(2)	1.47(4)	0.0174(7)	U_{11}	0.021(1)	0.0011(8)	0.0049(7)	U_{13}
Br3	4e	-0.3705(2)	x	x	1.833(1)	0.02319(1)	U_{11}	U_{11}	-0.002(1)	U_{12}	U_{12}

[i] Occupancy of Sc3 was refined to 0.89(2)%

Table 24. Important bond distances in $Sc_{20-x}Br_{28}Z_4$ phases

		$Sc_{20-x}Br_{28}Os_4$	$Sc_{20-x}Br_{28}Ru_4$	$Sc_{20-x}Br_{28}Mn_4$
Z-Z	(x3)	3.029(3)	3.077(4)	2.787(9)
Z-Sc1	(x3)	2.562(5)	2.537(4)	2.598(5)
Z-Sc2	(x3)	2.675(8)	2.676(5)	2.676(5)
Sc1-Sc1	(x2)	3.293(8)	3.284(5)	3.223(7)
Sc1-Sc1		3.64(1)	3.641(7)	3.597(8)
Sc1-Sc2	(x2)	3.512(4)	3.506(3)	3.475(4)
Sc1-Z		2.562(5)	2.537(4)	2.598(5)
Sc1-Br1	(x2)	2.795(4)	2.801(3)	2.796(4)
Sc1-Br1		3.021(5)	3.024(3)	3.038(4)
Sc1-Br2	(x2)	2.762(5)	2.747(3)	2.759(4)
Sc2-Sc1	(x6)	3.512(4)	3.506(3)	3.475(4)
Sc2-Sc2[b]	(x3)	4.31(2)	4.29(1)	4.42(1)
Sc2-Z	(x3)	2.675(8)	2.676(5)	2.676(6)
Sc2-Br1	(x3)	2.851(6)	2.848(4)	2.804(5)
Sc3-Sc3	(x3)	3.61(2)	3.66(1)	3.59(1)
Sc3-Br2	(x3)	2.855(9)	2.843(6)	2.836(7)
Sc3-Br3	(x3)	2.673(7)	2.684(5)	2.695(6)
Br1-Sc1		3.021(5)	3.024(3)	3.038(4)
Br1-Sc1	(x2)	2.795(4)	2.801(3)	2.796(4)
Br1-Sc2		2.851(6)	2.848(4)	2.804(5)
Br2-Sc1	(x2)	2.762(5)	2.747(3)	2.759(4)
Br2-Sc3		2.855(9)	2.843(6)	2.836(7)
Br3-Sc3	(x3)	2.673(7)	2.684(5)	2.695(6)
Br1-Br1[a]	(x2)	3.601(5)	3.616(3)	3.581(4)
Br1-Br2[a]	(x2)	3.699(2)	3.692(2)	3.664(3)
$\bar{d}_{Sc\text{-}Sc}$[b]		3.468	3.462	3.420

a Br-Br distances shorter than 3.70 Å are listed.
b Non-bonding Sc-Sc distances not included in cluster bond average.

Table 25. Important bond angles in $Sc_{20-x}Br_{28}Z_4$ phases

	$Sc_{20-x}Br_{28}Os_4$	$Sc_{20-x}Br_{28}Ru_4$	$Sc_{20-x}Br_{28}Mn_4$
Z-Z-Sc1	96.8(1)	96.38(9)	99.0(1)
Z-Z-Sc2	103.9(1)	103.1(1)	107.8(2)
Sc1-Z-Sc1	80.0(2)	80.7(1)	76.7(2)
Sc1-Z-Sc2	84.2(1)	84.50(7)	82.4(1)
Sc1-Z-Sc2	159.3(2)	160.5(2)	153.2(3)
Sc2-Z-Sc2	107.5(2)	106.7(1)	111.4(1)
$Sc1^{eq}$-$Sc1^{ax}$-$Sc2^{eq}$	98.4(2)	98.3(1)	99.9(1)
$Sc1^{eq}$-$Sc1^{ax}$-$Sc2^{eq}$	62.04(8)	62.08(6)	62.37(6)
$Sc1^{ax}$-$Sc1^{ax}$-$Sc2^{eq}$	58.79(7)	58.72(5)	58.83(6)
$Sc1^{ax}$-$Sc2^{eq}$-$Sc2^{eq}$	55.9(2)	55.8(1)	55.3(1)
Sc1-Sc2-Sc1	62.4(2)	62.6(1)	62.3(1)
Sc1-Sc2-Sc1	117.55(9)	117.63(6)	116.51(7)
Sc1-Sc2-Sc1	161.5(3)	161.8(2)	157.9(2)
Sc1-Br1-Sc1	81.2(2)	81.1(1)	80.1(1)
Sc1-Br1-Sc2	76.9(2)	76.7(1)	76.7(1)
Sc1-Br1-Sc1	103.4(1)	103.17(8)	104.17(9)
Sc1-Br1-Sc2	179.6(2)	179.9(1)	178.8(2)
Sc1-Br2-Sc1	73.2(2)	73.4(1)	71.5(1)
Sc1-Br2-Sc3	96.8(2)	96.2(1)	97.0(1)
Sc3-Br3-Sc3	85.0(3)	86.1(2)	83.6(2)

ax and eq refer to axial and equatorial positions around an octahedral coordination site.

Table 26. Angles around Sc atoms in $Sc_{20-x}Br_{28}Z_4$ phases

	$Sc_{20-x}Br_{28}Os_4$	$Sc_{20-x}Br_{28}Ru_4$	$Sc_{20-x}Br_{28}Mn_4$
Z-Sc1-Br1	176.3(2)	176.9(1)	174.5(2)
Z-Sc1-Br1	101.0(1)	101.2(1)	100.6(1)
Z-Sc1-Br2	103.3(1)	102.89(9)	105.7(1)
Br1-Sc1-Br1	76.4(1)	76.63(8)	75.59(9)
Br1-Sc1-Br2	79.4(1)	79.37(8)	78.23(9)
Br1-Sc1-Br1	90.3(2)	90.61(1)	90.3(1)
Br1-Sc1-Br2	155.5(2)	155.8(1)	153.5(1)
Br1-Sc1-Br2	87.38(9)	86.99(5)	86.83(6)
Br2-Sc1-Br2	84.7(2)	85.4(1)	84.1(1)
Z-Sc2-Z	69.0(2)	70.2(2)	62.7(3)
Z-Sc2-Br1	162.6(3)	163.7(2)	157.6(3)
Z-Sc2-Br1	96.98(7)	96.71(5)	98.52(8)
Br1-Sc2-Br1	94.9(2)	94.3(1)	96.4(2)
Br2-Sc3-Br2	81.4(3)	81.9(2)	81.4(2)
Br2-Sc3-Br3	170.6(4)	171.7(3)	169.7(3)
Br2-Sc3-Br3	91.5(4)	91.88(6)	90.86(6)
Br3-Sc3-Br3	94.8(3)	93.8(2)	96.0(2)

encompassed by Br atoms in the same manner (locally) as seen in the previous phases. Geometrical changes within the $Sc_{16}Z_4$ cluster unit are observed as Z (and the electron count) is varied.

It is interesting to consider the nonstoichiometry observed (75% occupied) in the Sc_4 position of the Fe, Ru, and Os phases. This seems to result from an electronic compromise made by the cluster unit to approach the preferred 60 cluster bonding electrons found in all related clusters. Removal of one-fourth of the Sc atoms in this tetrahedron reduces the number of electrons available for cluster bonding from 64 to 61. The structure of $Gd_{20}I_{28}Mn_4$ displayed disorder of this same M_4 site as well as some of the coordinating halogens. The reported cubic structure could be modelled by twinning of a rhombohedral structure.[63] There is no direct evidence for a rhombohedral distortion in the $Sc_{20-x}Br_{28}Z_4$ structures based on the refinement in a cubic system nor from an attempted refinement of $Sc_{20-x}Br_{28}Mn_4$ in space group R3m. Nevertheless, the similarity between the Sc and Gd phases leaves open the possibility that the correct symmetry is less than cubic. A slight rhombohedral distortion of the cell might result in ordering of the atoms within the Sc_4 tetrahedra.

The primitive cubic cell of $Sc_{20-x}Br_{28}Z_4$, shown in Figure 29, contains one $Sc_{16}Z_4$ oligomer, centered at the origin, and one Sc_4 tetrahedron, located at the body center. This figure and all other pictures in this section were drawn with positional and anisotropic thermal parameters from $Sc_{20-x}Br_{28}Mn_4$. The Sc atoms in the oligomer form a tetra-capped truncated tetrahedron, which encloses a Z_4

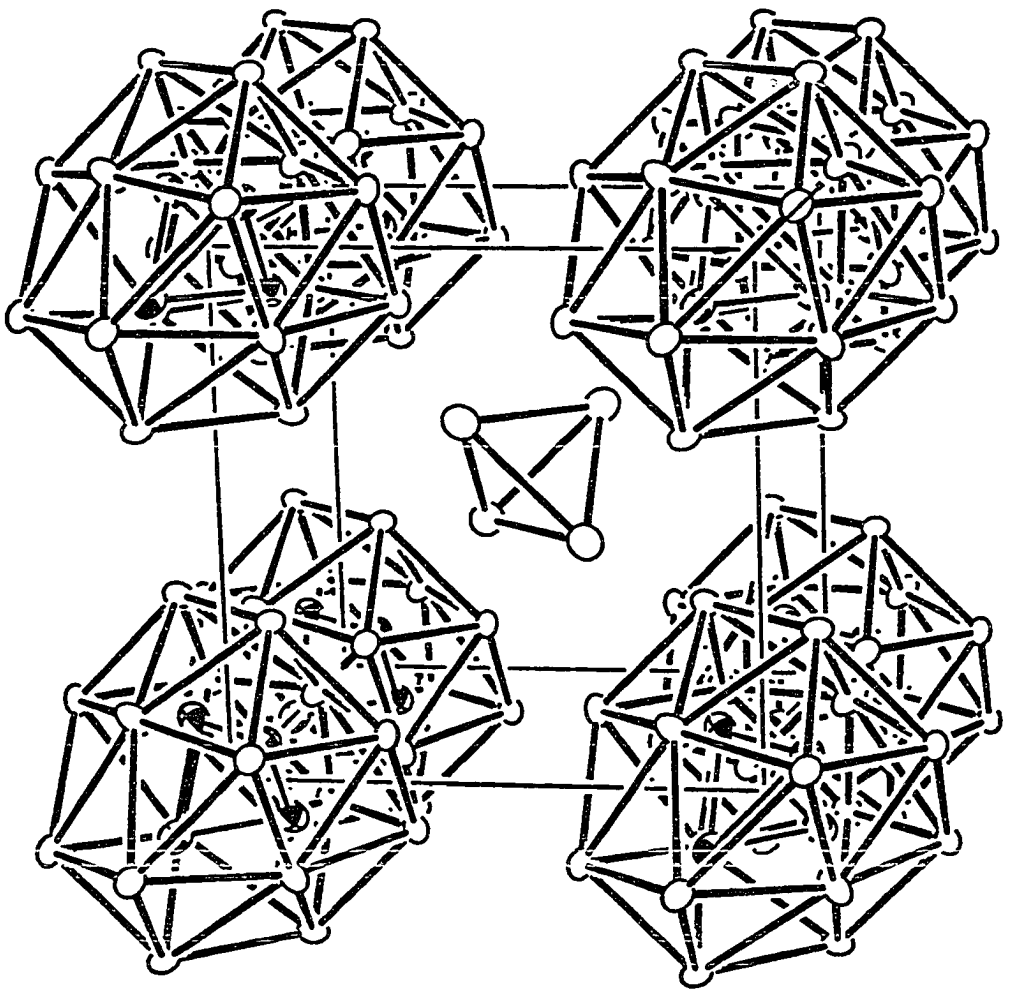

Figure 29. [$\bar{1}$00] view of the cubic unit cell of $Sc_{20-x}Br_{28}Z_4$, with oligomeric clusters at the corners and a Sc_4 tetrahedron at the body center of the cube. Br atoms are omitted for clarity. Sc is open; Z is quarter-shaded.

tetrahedron oriented coincident with the outer truncated tetrahedron. The cluster can also be described as a tetramer of distorted Sc_6Z octahedra, which are fused together through pairwise condensation of two edge-sharing octahedra. These "octahedra" are distorted into trigonal antiprisms composed of two sizes of Sc triangles. The interstitial atoms are markedly shifted out of the centers of the "octahedra" towards the oligomer center. Both clusters possess $\bar{4}3m$ (T_d) symmetry, the highest symmetry observed in any of the oligomeric clusters found to date. The larger clusters contain two crystallographically unique Sc atoms, as shown in Figure 30. The Sc1 atoms, each of which is coordinated to five other Sc atoms, make up the truncated tetrahedron, while six-coordinate Sc2 atoms cap the four pseudo-hexagonal faces. The clusters are oriented within the unit cell such that a three-fold axis along the body diagonal passes through the pseudo-hexagonal faces and Sc1-Sc1-Sc1 triangular faces of the cluster. The smaller Sc_4 tetrahedron is oriented with the four corners of the polyhedron pointing towards the truncated corners of four of the oligomers.

Bond distances between metal atoms within the compounds are similar to those observed in other reduced rare-earth metal halide compounds. The Sc-Sc distances range from ~3.22 Å (Pauling bond order of 0.27) to ~3.66 Å (Pauling bond order of 0.05), with the shortest values corresponding to the edges of the Sc1-Sc1-Sc1 triangular faces. An intermediate value (~3.50Å) is observed within the nominally hexagonal faces (Sc2-Sc1), and the largest values are found between pairs of apical Sc1 atoms as well as between Sc3 atoms in the Sc_4

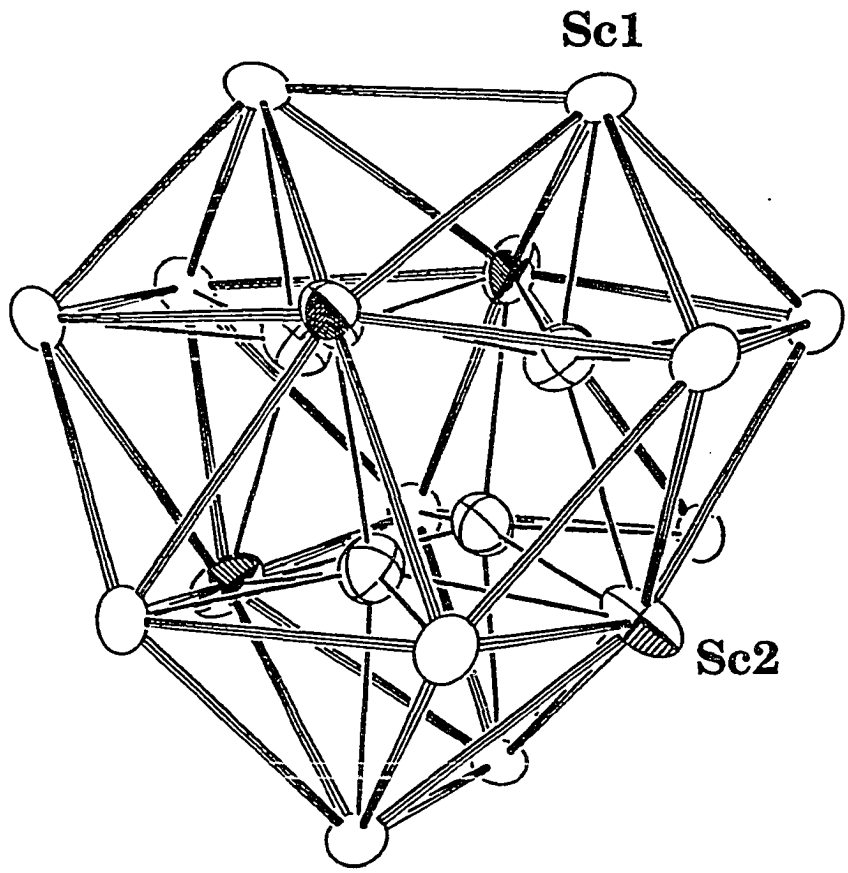

Figure 30. A ~[$\bar{1}$00] view of the $Sc_{16}Z_4$ cluster unit, which possesses $\bar{4}$3m (T_d) symmetry. The polyhedron is made up of two crystallographically unique Sc atoms, Sc1 (open) and Sc2 (quarter-shaded).

tetrahedron. The average Sc-Sc distance in the clusters is ~3.45 Å, which is comparable to the distances observed in $Sc_7I_{12}Co$ of 3.39 Å and 3.49 Å. The Sc-Z distances vary from 2.537(4) Å to 2.676(5) Å, with the largest range observed in $Sc_{20-x}Br_{28}Ru_4$. The Sc1-Z distances are distinctly shorter than the Sc2-Z distances; the interstitial atoms lie closer to the atoms in the Sc1-Sc1-Sc1 triangular face than to those in the Sc2-Sc2-Sc2 triangles. Generally, the Sc-Z distances are slightly smaller than the sum of Pauling's single bond metallic radii; this feature has been observed in other cluster phases as well. The only exception to this in these oligomers is in $Sc_{20-x}Br_{28}Mn_4$, where the Sc2-Mn distance is actually 0.05 Å longer than the sum of single bond radii.

The basic geometry of the $Sc_{16}Z_4$ clusters lies intermediate between that observed for the $Y_{16}Z_4$ and $Gd_{16}Mn_4$ clusters. As in the $Gd_{16}Mn_4$ cluster, the Sc1-Sc1-Sc1 triangular faces display markedly shorter distances (by >0.2 Å) than the other Sc1-Sc1 or Sc1-Sc2 distances within the cluster. The Sc2-Sc2 (non-bonding) distances are also larger relative to the average cluster Sc-Sc distance than the comparable values in the Y-containing clusters. In addition, the interstitial atoms form a much smaller tetrahedron than is found in the $Y_{16}Z_4$ clusters. However, the smaller size of the Sc balances this effect, so that the Sc1-Z-Sc2 *trans* angle (~160°) is more similar to those found in the Y clusters (~164°) than to that in the highly distorted $Gd_{16}Mn_4$ (148°).

Other variations in geometry are observed when the identity of Z is changed. The observed size change of the Z_4 tetrahedron is not proportional to

that expected based on Pauling's single bond radii. Contrary to the expected trend of $d_{Os-Os} > d_{Ru-Ru} > d_{Mn-Mn}$, the Ru_4 tetrahedron exhibits the largest distances of 3.077 Å, which correspond to a Pauling bond order of 0.11. The Os-Os distance of 3.029(3) Å is next largest and corresponds to a bond order of 0.14. The Mn-Mn distance of 2.787(9) Å is the smallest and corresponds to a bond order of 0.19 Å. Clearly, all three of these distances are short enough to signify important Z-Z interactions. The Sc-Sc distances within the clusters decrease slightly on going from the Os to Ru phases, with notably smaller Sc-Sc distances found in the Mn phase, which is consistent with that expected based on interstitial size considerations. The bond angles in the Os and Ru phases are similar to each other and, in many cases, are different from those seen in the Mn phase. Deviation of the Z-Z-Sc1 and Z-Z-Sc2 angles from 90° provides a measure of how far the interstitial is shifted out of the centers of the M_6Z "octahedra". Both $Sc_{20-x}Br_{28}Os_4$ and $Sc_{20-x}Br_{28}Ru_4$ display larger Z-Z-Sc1 angles (by ~5°) and larger Z-Z-Sc2 angles (by 2-3°) than those observed in $Y_{16}Br_{20}Ru_4$. The distortion in $Sc_{20-x}Br_{28}Mn_4$ is even more pronounced; the angles are 5-7° larger than observed in $Y_{16}Br_{20}Ru_4$. Accordingly, the other angles around the Z atoms are more distorted in $Sc_{20-x}Br_{28}Mn_4$ than in $Sc_{20-x}Br_{28}Os_4$, $Sc_{20-x}Br_{28}Ru_4$, or $Y_{16}Br_{20}Ru_4$.

The halogens adopt three distinct modes of connectivity to the Sc atoms, corresponding to their three crystallographically different positions. The Br1 atoms, pictured in Figure 31a, cap three Sc1-Sc1-Sc2 triangular faces in each pseudo-hexagonal face of the cluster and also bond exo to Sc1 atoms in the

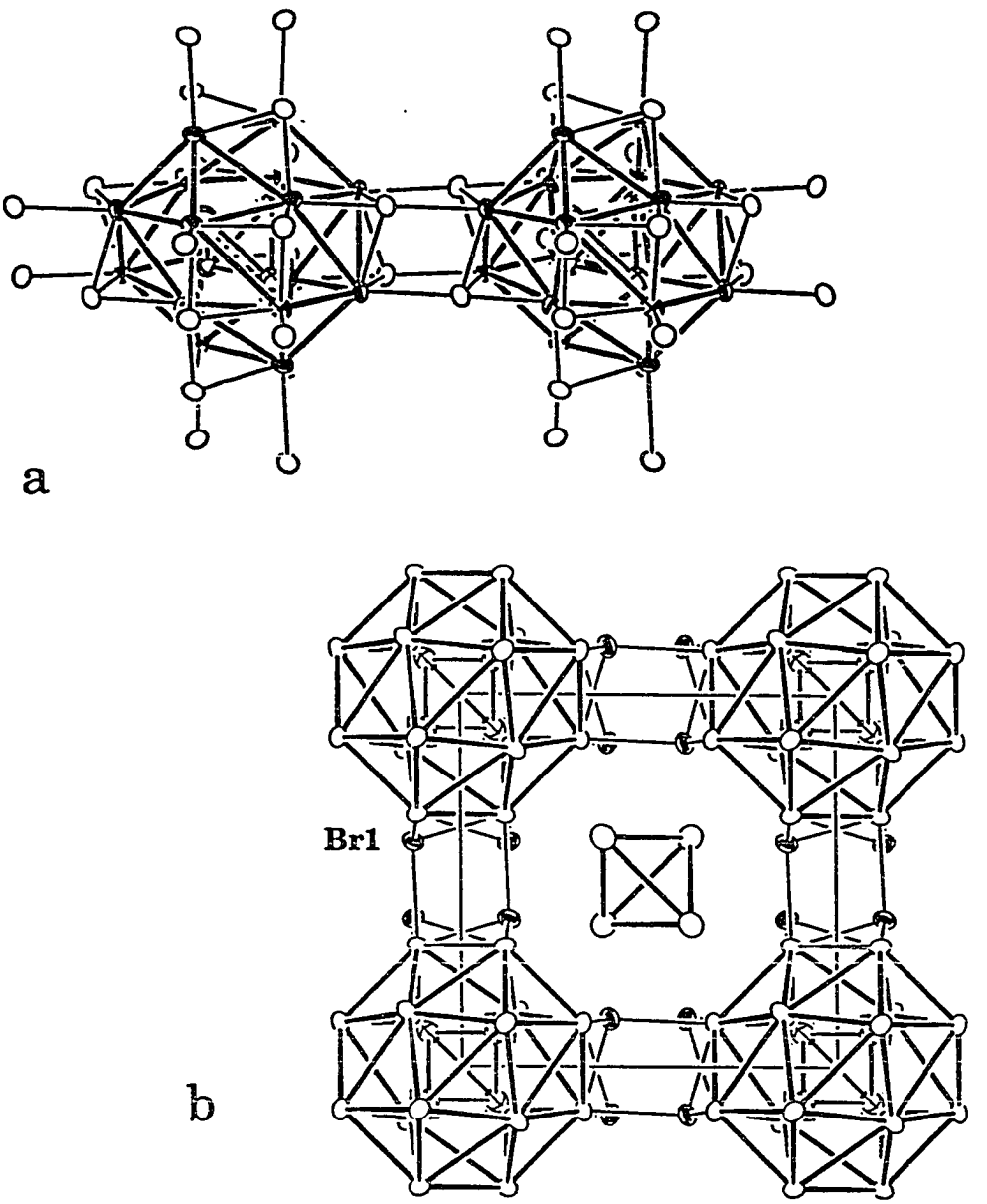

Figure 31. a) The bonding mode adopted by Br1 atoms, which cap three of the six Sc1-Sc1-Sc2 triangular faces on each hexagonal face of the cluster. b) The square network formed via Br1 interconnections. The same square network was observed in $Y_{16}Br_{20}Ru_4$.

adjacent clusters. Each oligomer is connected in this fashion to six neighboring oligomers, which are related by a unit cell translation of ±a, ±b, or ±c. This bonding mode is nearly identical to that displayed by Br1 atoms in $Y_{16}Br_{20}Ru_4$ (compare Figures 31a and 2b), the only difference being that these connections occur in all three crystallographic directions due to the cubic symmetry, whereas they only occur along $\vec{a}$ and $\vec{b}$ in $Y_{16}Br_{20}Ru_4$. Accordingly, the clusters form the same type of square network, pictured in Figure 31b, as seen in $Y_{16}Br_{20}Ru_4$, but extended in all three dimensions. The shortest Sc-Sc contacts between neighboring oligomers is 4.61 Å between Sc1 atoms. The second bonding mode connects the oligomeric clusters to the Sc_4 tetrahedra, as illustrated in Figure 32. Three Br2 atoms bridge the Sc1-Sc1 edges in the Sc1-Sc1-Sc1 triangular faces while simultaneously bonding to 75% of a Sc3 atom in the Sc_4 tetrahedron. Four Sc_4 tetrahedra are connected to each oligomeric cluster and are arranged in a tetrahedral manner around the cluster. Similarly, four clusters are connected to and arranged in a tetrahedral fashion about each Sc_4 unit. The closest Sc-Sc contacts between the oligomers and the Sc_4 tetrahedra are 4.19 Å between Sc1 and Sc3 atoms. The last halogen functionality is shown in Figure 33, where Br3 atoms cap the four Sc3-Sc3-Sc3 triangular faces of the Sc_4 tetrahedron, the two atom types together forming a distorted cube of Sc3 and Br3 atoms.

Each $Sc_{16}Z_4$ cluster is surrounded by thirty-six Br atoms, as shown in Figure 34, where emphasis is placed on the octahedral coordination of the Sc

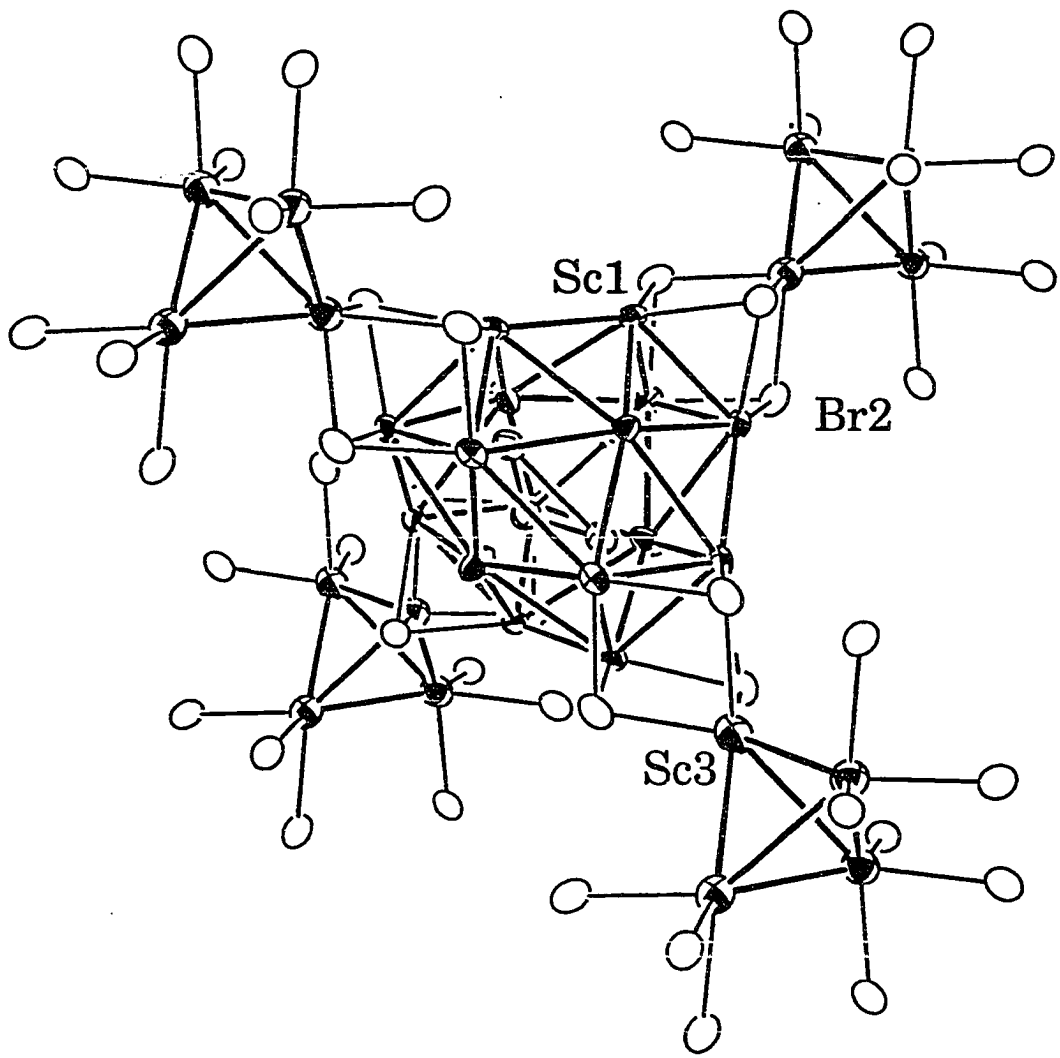

Figure 32. Illustration of the Br2 bonding mode, which bridges Sc1-Sc1 edges of the oligomer while bonding to a Sc3 atom in the Sc_4 fragment. Four Sc_4 tetrahedra surround each oligomer in a tetrahedral manner.

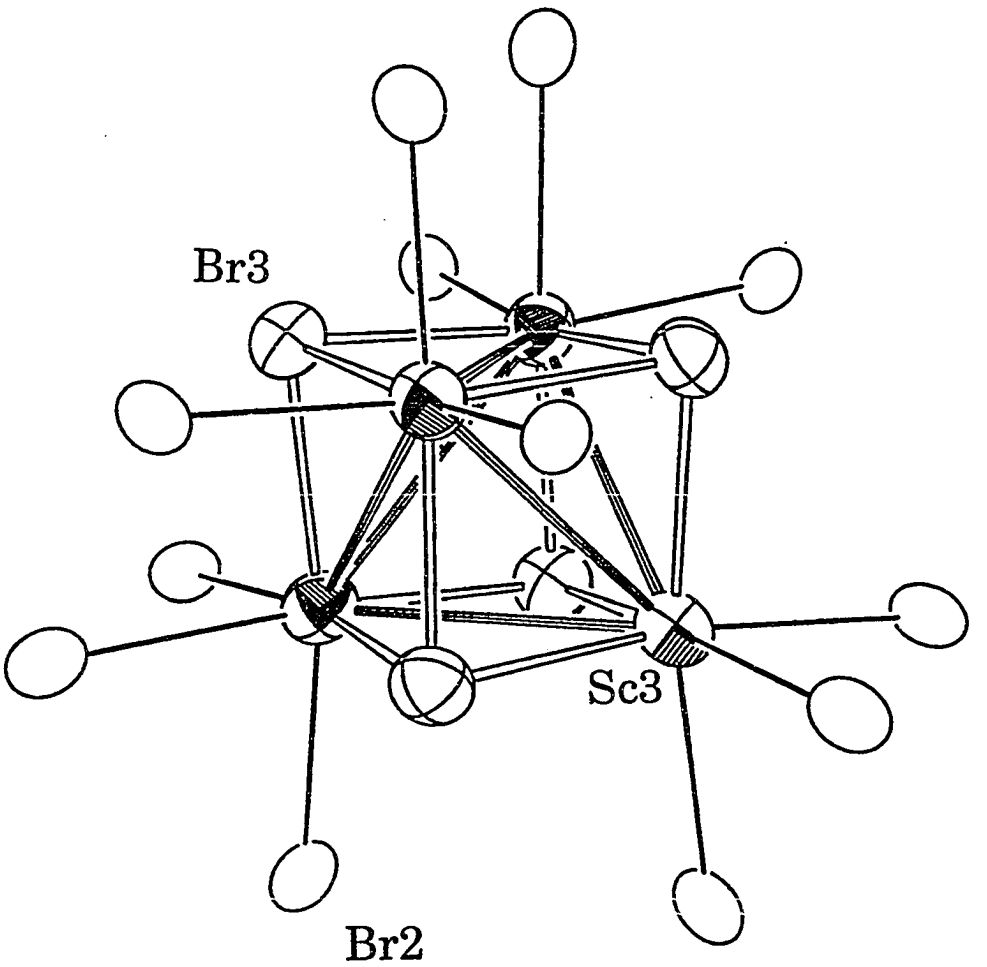

Figure 33. The Sc_4Br_8 fragment, composed of Sc3 tetrahedra coordinated by Br3 atoms, which cap the four Sc3 triangular faces, and Br2 atoms, which bridge between the Sc tetrahedra and the oligomeric clusters.

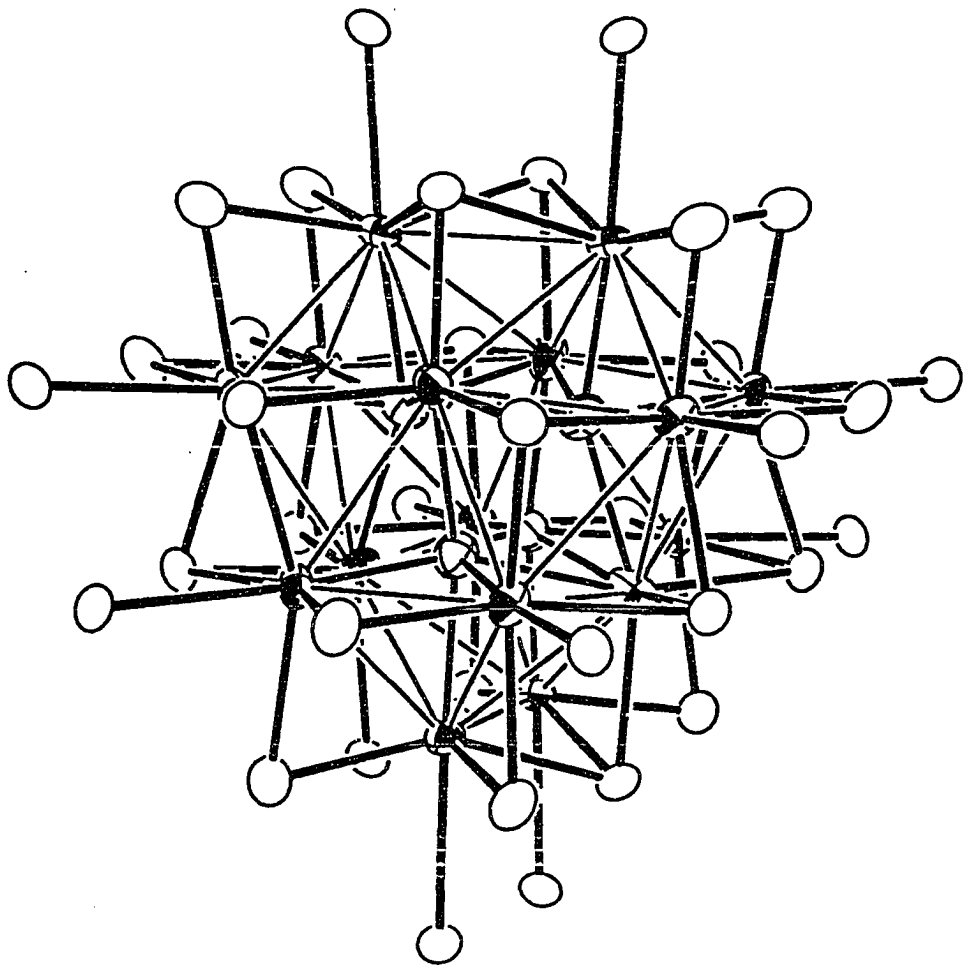

Figure 34. A $Sc_{16}Z_4$ cluster with its 36 atom coordination sphere, where heavy bonds emphasize the octahedral environment of the Sc atoms. Sc is quarter-shaded, Br is open, Z is crossed.

atoms. The coordination sphere of Br atoms surrounds and isolates each cluster in the same manner seen in the other oligomer-containing cluster phases. The Sc-Br bond distances around the clusters range from ~2.75 Å to ~3.04 Å, with the average Sc-Br distance around the clusters of 2.831 Å, 2.828 Å, and 2.825Å for the Os, Ru, and Mn phases, respectively. These values are larger than the sum of crystal radii for Sc^{+3} (CN=6) and Br^{-1} of 2.705 Å, a feature typical of rare-earth metal halide compounds. The edge-bridging Br2 atoms exhibit the shortest Sc-Br distances around the clusters, while the Br1 atoms exo to Sc1 vertices, which are *trans* to the interstitial atoms, are the longest. The Sc3-Br2 distances around the Sc_4 tetrahedra are near the average Sc-Br distance on the cluster. The Sc3-Br3 distances are even shorter than the sum of crystal radii; the Sc3 atoms exhibit Sc-Br distances typical of isolated Sc^{+3} ions. Due to the relative sizes of Sc and Br, the metal atoms are withdrawn from the Br^{i}_{4} square planes on the periphery of the cluster; the Br1-Sc1-Br2 *trans* angles are between 153° and 156°, which are smaller by ~5° than was observed in $Y_{20}Br_{36}Ir_4$.

The halogen and interstitial atoms together form approximately cubic-close-packed layers, with the Sc atoms occupying pseudo-octahedral holes between the layers. These close-packed layers lie parallel to the (111), ($\bar{1}$11), ($\bar{1}\bar{1}$1), and (11$\bar{1}$) planes, which correspond to the four triangular faces of the Z_4 tetrahedron. The Sc atoms form clusters by occupying the 16 sites adjacent to groups of Z atoms. Other Sc atoms, in groups of four, occupy nearby octahedral sites formed only by Br atoms, yielding Sc_4Z_8 fragments. A view parallel to these

close-packed layers containing one cluster and the surrounding Sc_4 fragments along with all the coordinating Br atoms is pictured in Figure 35. As was seen in the $Y_{16}Z_4$ clusters, the Z atoms are slightly displaced from the close-packed layers toward each other, while the Sc atoms in the cluster are more noticably shifted towards the cluster center. The Sc atoms that make up the Sc_4 tetrahedra do not appear to be shifted, but instead lie halfway between the close-packed layers. The shortest observed Br-Br contacts of 3.601(5) Å occur both within and between Br1 atoms in adjacent close-packed layers.

Magnetic susceptibility measurement

All of the $M_{16}Z_4$ clusters found in the Y and Gd systems have 60 electrons available for metal-metal bonding. This electron count corresponds to a closed-shell orbital configuration for both $Y_{16}Br_{20}Ru_4$[62] and $Gd_{20}I_{28}Mn_4$,[63] based on extended Hückel calculations. The discovery of the $Sc_{20-x}Br_{28}Z_4$ phases, in which the electron count deviates from the "optimal" 60 electrons, suggests that the orbital configuration has changed in some way, for either structural reasons, electronic reasons (eg. relative electronegativity), or both. Based on the single crystal results, the electron count for $Sc_{19}Br_{28}Z_4$ Z = Os, Ru is 61 electrons. If this extra unpaired electron is localized on the cluster, the material should exhibit temperature-dependent paramagnetic behavior. To test this, magnetic susceptibility measurements were performed on powdered samples of $Sc_{19}Br_{28}Os_4$, $Sc_{19}Br_{28}Ru_4$, and $Sc_{20-x}Br_{28}Fe_4$ judged single phase based on Guinier powder patterns. The data for $Sc_{19}Br_{28}Os_4$, measured at both 0.1 and 3 Tesla

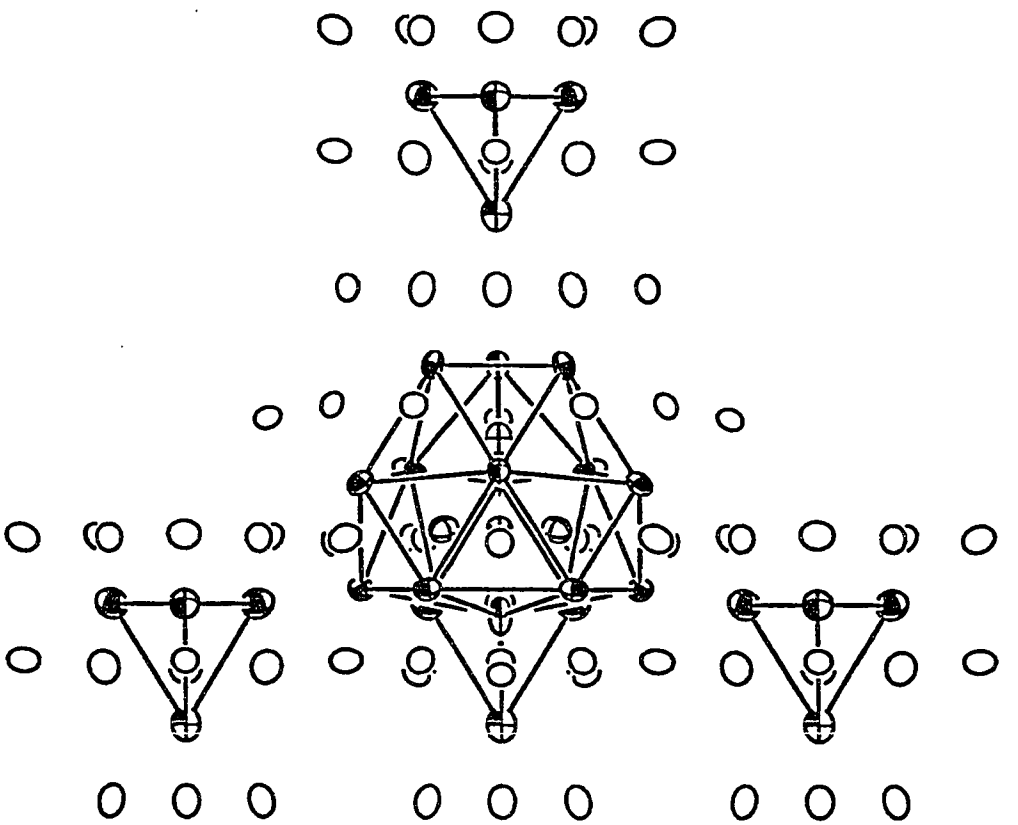

Figure 35. A $Sc_{16}Z_4$ cluster and neighboring Sc4 fragments along with coordinating Br atoms viewed parallel to the pseudo-close-packed layers. Sc is quarter-shaded; Br is open; Ru is crossed.

and presented in Figure 36, exhibits Curie-Weiss behavior above 100 K, presumably combined with van Vleck temperature-independent paramagnetism (TIP). At ~60 K, the sample undergoes what appears to be antiferromagnetic ordering, followed by a second transition at ~20 K. Analysis of the data (measured at 3 Tesla) for T > 100 K with a nonlinear least squares program provided a TIP term of 0.0008(2) emu/mol along with a μ_{eff}=2.0(1)μ_B, which is similar to the expected value of 1.73μ_B for one unpaired, spin-only, localized electron. Similar behavior, as shown in Figure 37, was observed at 0.1 and 3 Tesla for $Sc_{19}Br_{28}Ru_4$, which, along with van Vleck TIP, displays Curie-Weiss behavior for T > ~130 K with deviation at lower temperatures. Again, a weak antiferromagnetic ordering seems to occur at ~60K. Analysis of the data (measured at 3 Tesla) for T > 130 K yielded a μ_{eff} = 2.1(1)μ_B and a TIP contribution of 0.0043(2) emu/mol. The increase in the magnitude of the molar susceptibility at lower field strength suggests that a small amount of a ferromagnetic impurity is present in the sample. The data for $Sc_{20-x}Br_{28}Fe_4$ at 3 Tesla are presented in Figure 38. The data follows Curie-Weiss behavior for T > 100 K, and again deviates at lower temperatures, and also displays a van Vleck TIP contribution. Data analysis indicated μ_{eff}=2.0(4)μ_B, with a TIP term of 0.0077(5) emu/mol. The transition at ~60 K corresponds to a much weaker interaction in this Fe analogue than was displayed in the Os phase, but an inflection point in the susceptibility vs. T curve is still observed.

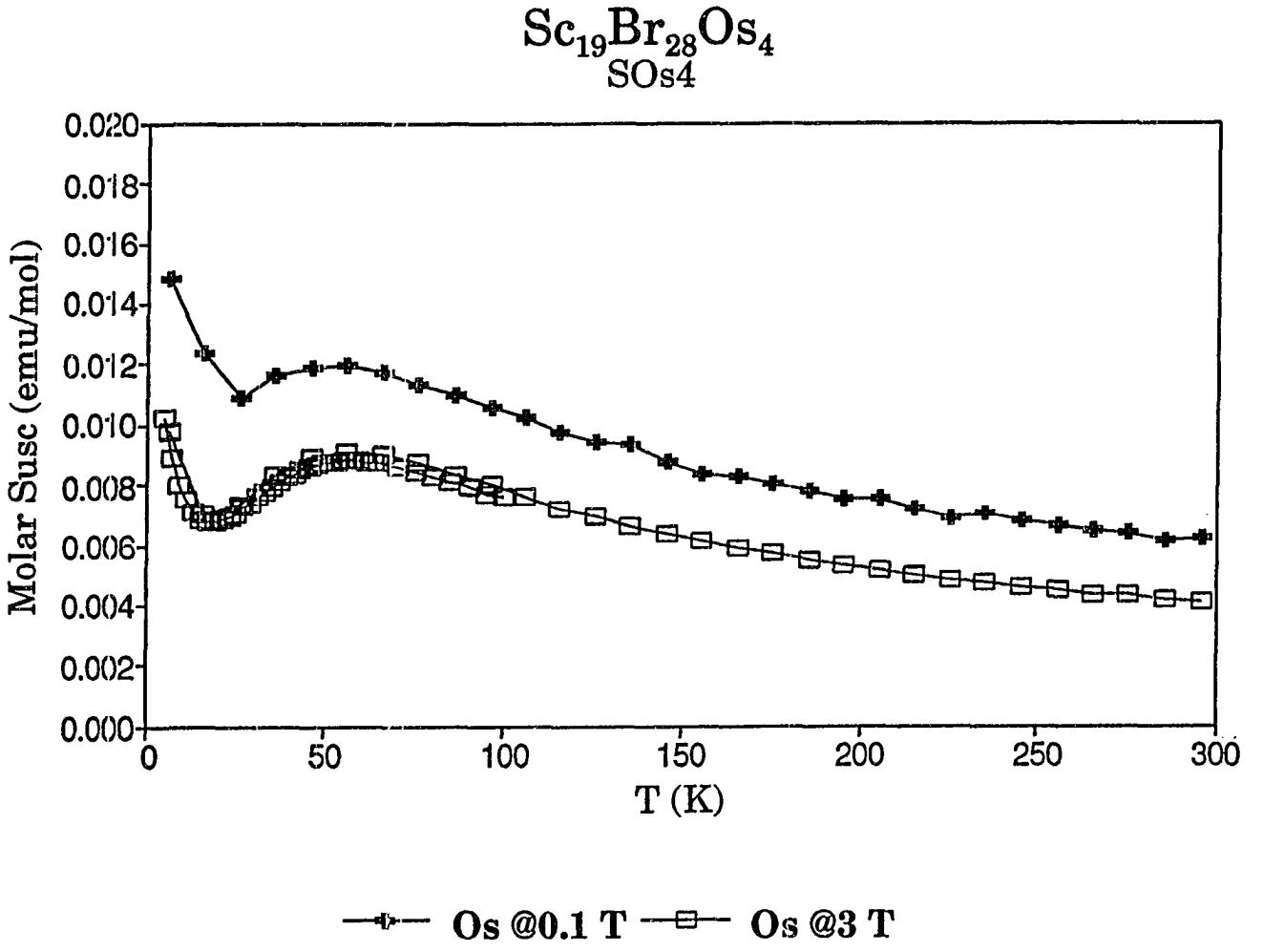

Figure 36. A plot of the magnetic susceptibility of $Sc_{20-x}Br_{28}Os_4$ as a function of temperature at field strengths of 0.1 and 3 Tesla. The compound is paramagnetic with $\mu_{eff}=2.0(1)\mu_B$.

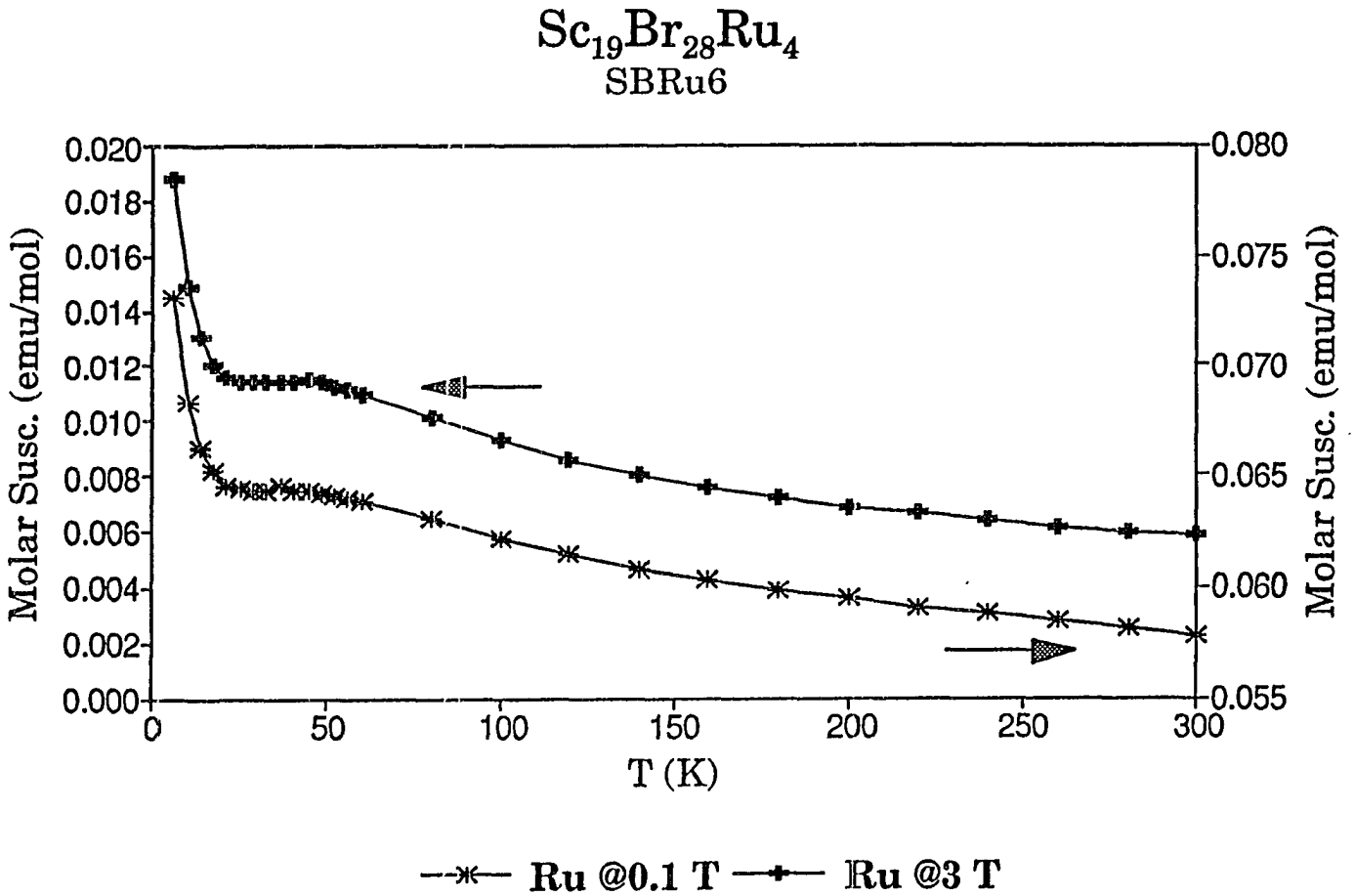

Figure 37. A plot of the magnetic susceptibility of $Sc_{20-x}Br_{28}Ru_4$ as a function of temperature at field strengths of 0.1 and 3 Tesla. The compound is paramagnetic with μ_{eff}=2.1(1)μ_B.

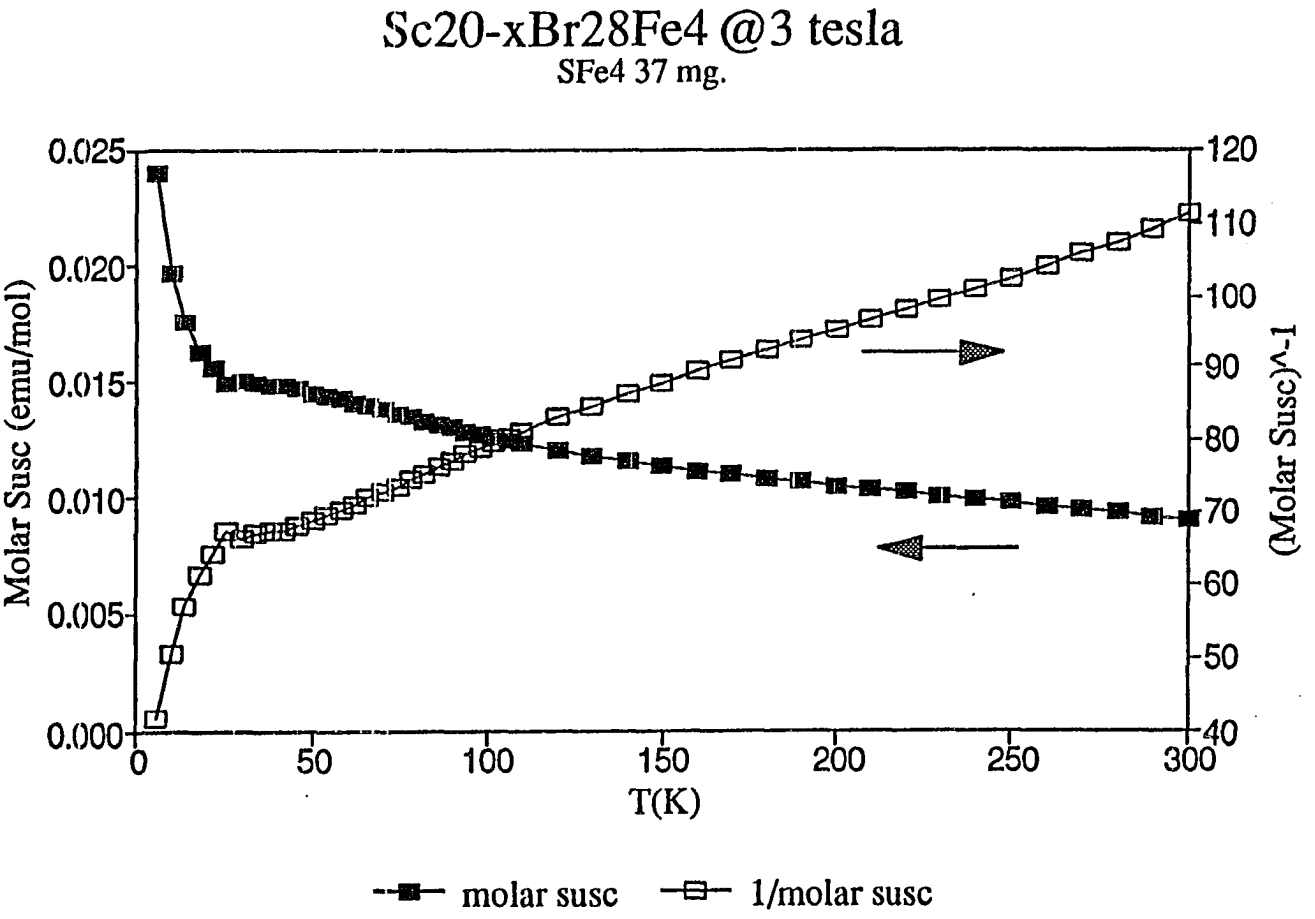

Figure 38. A plot of the magnetic susceptibility of $Sc_{20-x}Br_{28}Fe_4$ as a function of temperature at field strengths of 3 Tesla. The compound is paramagnetic with $\mu_{eff}=2.0(4)\mu_B$.

These results indicate that the three phases are paramagnetic and contain one unpaired, localized electron, whose signal is combined with a van Vleck temperature-independent paramagnetic term, as observed in other oligomeric phases and some transiton metal cluster phases.[90,91] Additionally, the phases, particularly $Sc_{20-x}Br_{28}Os_4$, undergo a transition at low temperatures, which causes a change in the compound's magnetic properties. The data, while behaving similar to that predicted by the Curie-Weiss law at high temperatures, deviates from Curie-Weiss at temperatures less than 100 K.

Results of the measurement of the hysteresis curves of $Sc_{20-x}Br_{28}Os_4$ at 50 K and $Sc_{20-x}Br_{28}Ru_4$ at 60 K as a function of applied field are given in Figures 39 and 40. The Os phase exhibits a linear relationship between magnetization and field, as expected of a paramagnetic phase, and no significant hysteresis. The Ru phase shows almost no hysteresis, but a plot of magnetization vs. field displays a small S-shape near low field strengths; this could be caused by the presence of a ferromagnetic impurity in the paramagnetic sample.

$Pr_8Br_{13}N_3O$

The presence of adventitious impurities such as C and N was an important factor in the early syntheses of reduced rare-earth metal halides. Without the stabilization provided by interstitial atoms, cluster phases generally do not form. Of course, now interstitials are added by design, in attempts to form new phases as well as to electronically modify known phases. However, the

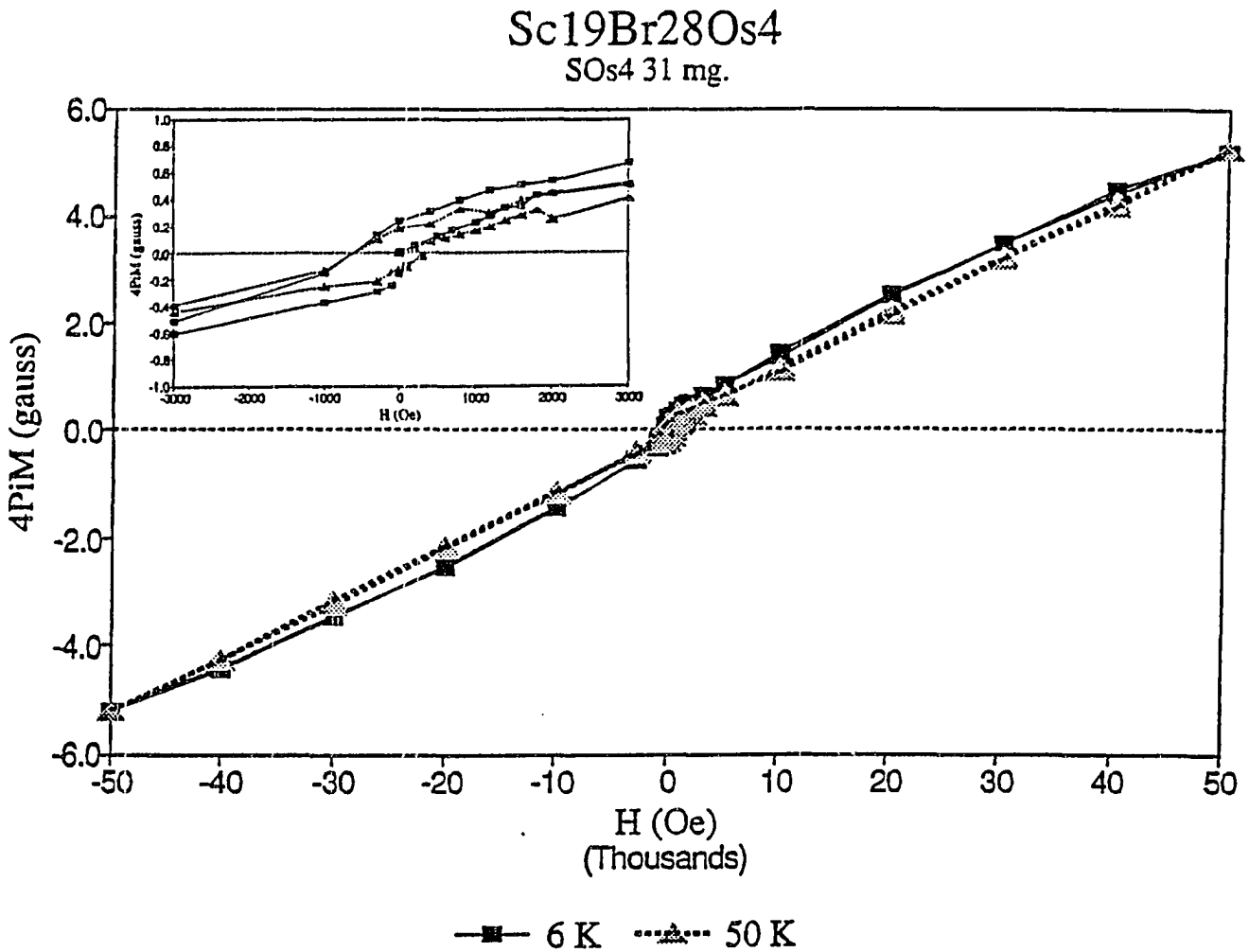

Figure 39. Plot of the magnetization of $Sc_{20-x}Br_{28}Os_4$ as a function of field strength at 50 K. The data exhibit a linear relationship, characteristic of paramagnetic material.

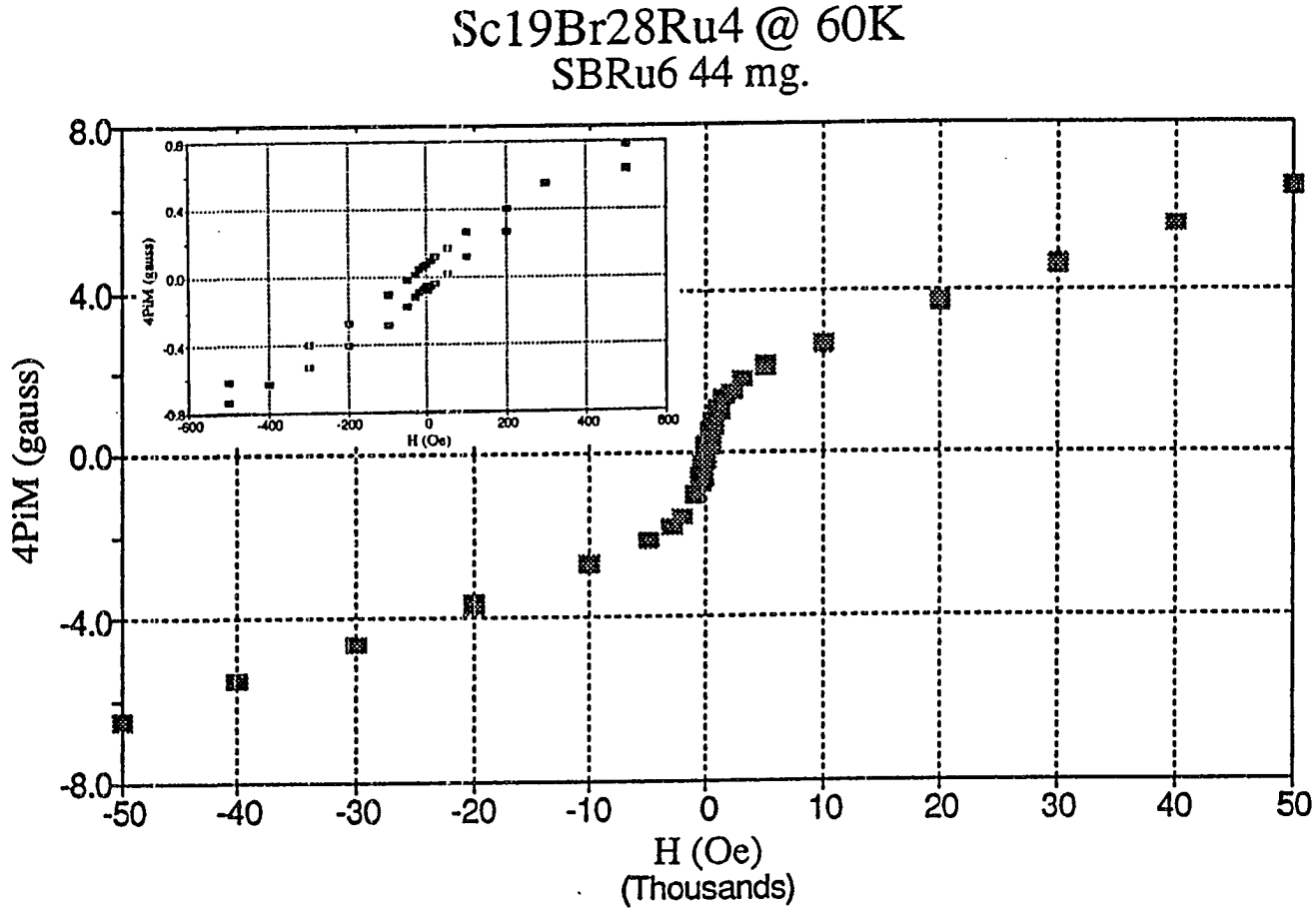

Figure 40. Plot of the magnetization of $Sc_{20-x}Br_{28}Ru_4$ as a function of field strength at 60 K.

discovery of this new structure type proves that the phenomenon of the "adventitious" interstitial can still provide new and unexpected materials.

Synthesis

The title compound was obtained from a reaction loaded as $Pr_2Br_2Mn_2$ and heated at 950°C for 20 days then slow cooled. The product consisted of Pr_2Br_5, PrOBr, plus a source of unidentified lines, and it also contained a small number of block-shaped black crystals. A few black crystals of the same phase with identical cell parameters were also obtained from a reaction loaded as Pr_2Br_2Fe and heated similarly, implying that the phase did not contain Mn or Fe. A single crystal X-ray diffraction study showed that the compound crystallized in a new structure type and had the formula $Pr_8Br_{13}Z_4$; Z was a light element that refined best as N. The powder pattern calculated from this structure model did not match any lines in the observed powder patterns of these two reactions. The likely sources for adventitious impurities included N from the dry box atmosphere and O from slight hydrolysis of the reagents ($PrBr_3$) or other impurities from the Mn, Fe, or Pr metal. A 3:1 ratio of N:O would result in the valence compound $Pr_8Br_{13}N_3O$. A combination of C and O could also provide a valence compound.

To determine the identity of the light interstitial element, a series of reactions incorporating C, N, and O was loaded. Starting materials were $PrBr_3$, Pr, Pr_6O_{11}, PrN, and amorphous C. Reactions loaded as $Pr_8Br_{13}Z_4$ with only O, only C, or as O and C (2.5:1.5 ratio) as interstitials and heated at 950°C for 20

days did not yield this new phase. Reactions loaded with $PrBr_3$ and PrN in ratios of 1:0.9 ($Pr_{8.4}Br_{13.3}N_4$) and 1:1 ($Pr_{7.6}Br_{10.9}N_4$) and heated similarly resulted in black crystals and chunks as a product, which ground to a light gray powder. The material from both of these reactions included a small amount (10-15%) of PrN and traces (<10% each) of PrOBr and $Pr_8Br_{13}Z_4$, with an unidentified major phase. A third reaction loaded with the $PrBr_3$:PrN ratio of 1:0.7 ($Pr_8Br_{11}N_{3.3}$) and heated at 950°C for 20 days resulted in ~ 30% yield of $Pr_8Br_{13}Z_4$ along with ~10% PrOBr and a majority of the unknown phase seen in the previous reactions. The yield of $Pr_8Br_{13}Z_4$ increased as the ratio of $PrBr_3$:PrN increased. The amount of PrOBr also showed this trend, suggesting that the $PrBr_3$ was not O-free; slight hydrolysis occurs within a few months even when stored in the dry box. As no more PrN was readily available, two of these reactions were ground and reloaded with either C or Pr_6O_{11} added, to give the loaded compositions of $Pr_8Br_{13}N_3O$ and $Pr_8Br_{13}N_3C$ and heated at 950° for 20 days. Based on Guinier powder pattern results, both of these reactions produced $Pr_8Br_{13}Z_4$, the former reaction in a high yield (~75%) while the latter resulted in smaller amounts (~30%) of the phase. Previous experience in reloading reaction products of rare-earth metal halides has shown that a significant increase in the O-containing phases (typically MOBr) is observed in the final product. Thus, the lesser amount of $Pr_8Br_{13}Z_4$ found in the reaction loaded with a mixture of C and N could have resulted from O contamination of the sample. A reaction loaded with a mixture of N (as PrN) and C in a 1:3 ratio yielded a small amount (~10%) of

the phase as well, again presumably stabilized by a small amount of O impurity. The high yield of $Pr_8Br_{13}Z_4$ in the reaction loaded as $Pr_8Br_{13}N_3O$ strongly suggests that this is the identity of the phase. Further synthetic attempts with freshly sublimed $PrBr_3$, PrN, and Pr should be carried out to clarify this.

Attempts at incorporation of the main-group element B into Pr-Br cluster phases at 850° C resulted in the formation of Pr_3Br_3B, which is isostructural with cubic Pr_3Br_3Z (Z = Co, Os, Rh, Ir, Pt).[32] Based on 18 Guinier powder pattern lines, the lattice parameter of the cubic cell is a=11.6333(8) Å.

Structure determination

The shiny black crystal used for the single crystal study of $Pr_8Br_{13}N_3O$ was obtained from a reaction loaded as $Pr_2Br_2Mn_2$ and heated at 950°C for 20 days before slow cooling. Data collection was performed at room temperature on a Rigaku AFC6R automated diffractometer using Mo Kα radiation. A random search located 18 reflections with an average intensity of 7,600 counts which indexed to a triclinic cell by the diffractometer software, a=11.737(5), b=15.508(8), c=8.347(3), α=105.60(4), β=110.82(3), γ=93.71(4), that was confirmed by axial photos. A hemisphere (h,±k,±l) of data was collected between the 2θ limits of 2 and 50°; the other hemisphere (-h,±k,±l) was collected between the 2θ limits of 2 and 46°. After data collection, three psi scans were measured, which exhibited a transmission range of 0.301 to 1.000. Important data collection and refinement parameters are listed in Table 27.

Table 27. Crystallographic data for $Pr_8Br_{13}N_3O$

Crystal data	
Formula	$Pr_4Br_{6.5}N_2$
Space group, Z	C2/c, 8
a (Å)[a]	21.967(8)
b (Å)	8.355(2)
c (Å)	16.889(7)
β (deg.)	119.40(3)
V (Å^3)	2701(3)
D_{calc} (g/cm^3)	5.465
μ (Mo Kα, cm^{-1})	331.67
Data collection	
Crystal dimensions, mm	0.19 x 0.17 x 0.14
Diffractometer	Rigaku AFC6R
Radiation, wavelength (Å)	Mo Kα, 0.71069
Scan mode	ω
Octant measured, $2\theta_{max}$	-h,±k,±l to 50°, h,±k,±l to 46°
Refinement	
No. of measured reflections	8339
No. of independent reflections	2829
No. of indep. reflections ($I \geq 3\sigma_I$)	1794
No. of variables	105
Transmission coefficient range	0.831–1.097
Secondary extinction coefficient	7.4(4) x 10^{-8}
R_{avg} (I>0)	0.070
R, R_w	0.0290, 0.0310
Largest residual peak, e/Å^3	1.65 (0.96 Å from Br5), -1.65

[a] Guinier cell constants from 22 lines.

Structure solution began with data reduction, which included Lorentz-polarization corrections and an empirical absorption correction based on an averaged transmission curve. Intensity statistics strongly indicated a centro-symmetric space group. Data averaging in $P\bar{1}$ resulted in an R_{avg} of 5% for all data. Direct methods (SHELXS-86) provided a reasonable solution containing four Pr atoms and 13 Br atoms; after the addition of four light atoms located in a difference Fourier map, the model refined isotropically to R=6.1%, R_w=6.3%. ORTEP drawings of the compound seemed to indicate the presence of higher symmetry. When the atomic positions were tested for the presence of higher symmetry, a glide plane was detected which related the atoms; the true symmetry of the cell was C-centered monoclinic with a=21.96 Å, b=8.35 Å, c=16.89 Å, and β=119.4°. After transforming the data to this higher symmetry cell, the equivalent starting model was again obtained with the direct methods procedure of SHELXS-86, and the refinement proceded uneventfully. Isotropic refinement of all atoms plus the secondary extinction coefficient resulted in a value of R=0.055 and R_w=0.060. Anisotropic refinement of the Pr and Br lowered the R to 0.0324 and R_w to 0.0341; the thermal parameters were generally well-behaved, but two Br atoms had aspect ratios near four. Application of a DIFABS absorption correction gave a final R of 0.0291 and R_w of 0.0310, but only changed the anisotropic thermal parameters slightly. The light atoms were refined isotropically as N and had very similar thermal parameters; there was no indication of the presence of ordered O, but X-ray techniques are relatively

insensitive to such small differences in electron density. The largest positive and negative peaks in the final difference Fourier calculation were 1.65 e/Å^3, located 0.96 Å from Br5, and -1.65 e/Å^3. The calculated structure factors of all reflections agreed with those calculated from the model to within less than $5\sigma_F$. Positional and anisotropic thermal parameters are listed in Tables 28 and 29.

The powder pattern calculated from the structure model agrees very well with that observed for the product of a reaction loaded as $Pr_8Br_{13}N_3O$. Lattice parameters were calculated with the LATT program based on the positions of 22 Guinier powder pattern lines.

Structure description

The structure of $Pr_8Br_{13}N_3O$ may be described as being built of condensed Pr_6 octahedral chains which have been distorted to Pr_4 tetrahedra sharing opposite edges, forming isolated $Pr_{4/2}$ infinite chains. Each tetrahedron is centered by either N or O, while the Br atoms sheath as well as interconnect the chains. The unit cell projection along $\vec{b}$ in Figure 41 reveals that the separated chains stack along $\vec{b}$ and extend infinitely within the a-b plane at heights of z=0, 1/2, and 1. These chains do not parallel $\vec{a}$, but instead run along the face diagonals of the unit cell. The chains within the a-b plane at z=0, pictured in Figure 42a, extend along the [1$\bar{1}$0] direction. The chains at a height of z=1/2, shown in Figure 42b, run along [110] and are related to those at z=0 and 1 by a c-glide perpendicular to $\vec{b}$.

Table 28. Positional and equivalent isotropic thermal parameters for $Pr_8Br_{13}N_3O$

Atom	Type	x	y	z	B_{eq}
Pr1	8f	0.36848(3)	0.42542(8)	0.05601(5)	0.72(2)
Pr2	8f	0.07310(3)	0.32246(8)	0.43956(5)	0.85(2)
Pr3	8f	0.43593(3)	0.46492(8)	0.38449(5)	0.82(2)
Pr4	8f	0.22955(3)	0.27525(8)	0.38641(5)	0.78(2)
Br1	8f	0.20065(6)	0.0970(2)	0.13995(9)	1.23(5)
Br2	8f	0.31381(6)	0.4386(2)	0.18406(9)	1.04(4)
Br3	8f	0.34922(6)	0.1512(2)	0.36200(9)	1.08(4)
Br4	8f	0.46523(6)	0.1726(2)	0.0283(1)	1.64(5)
Br5	8f	0.32270(7)	0.0759(2)	0.0620(1)	2.06(5)
Br6	8f	0.07420(7)	0.3005(2)	0.2273(1)	2.30(5)
Br7	4e	0	0.8686(3)	1/4	1.80(7)
N1	8f	0.0472(4)	0.067(1)	0.4641(7)	0.7(2)
N2	8f	0.1767(5)	0.187(1)	0.4696(7)	0.7(2)

Table 29. Anisotropic thermal parameters for $Pr_8Br_{13}N_3O$

Atom	U_{11}	U_{22}	U_{33}	U_{12}	U_{13}	U_{23}
Pr1	0.0118(3)	0.0089(4)	0.0080(4)	-0.0007(3)	0.0059(3)	0.0003(3)
Pr2	0.0113(3)	0.0075(4)	0.0127(4)	0.0008(3)	0.0054(3)	0.0009(3)
Pr3	0.0079(3)	0.0140(4)	0.0076(4)	-0.0011(3)	0.0027(3)	-0.0006(3)
Pr4	0.0103(3)	0.0126(4)	0.0070(4)	-0.0004(3)	0.0043(3)	-0.0001(3)
Br1	0.0150(6)	0.0221(7)	0.0099(7)	-0.0058(5)	0.0062(5)	-0.0026(6)
Br2	0.0157(6)	0.0160(6)	0.0099(7)	0.0000(5)	0.0081(5)	0.0009(5)
Br3	0.0130(6)	0.0166(7)	0.0105(7)	-0.0009(5)	0.0049(5)	-0.0028(5)
Br4	0.0187(6)	0.0135(7)	0.036(1)	-0.0027(5)	0.0176(6)	-0.0043(6)
Br5	0.0343(7)	0.0126(7)	0.048(1)	-0.0025(6)	0.0326(7)	-0.0005(7)
Br6	0.0169(6)	0.0287(8)	0.026(1)	0.0021(6)	-0.0013(6)	0.0027(7)
Br7	0.0152(9)	0.040(1)	0.012(1)	0	0.0057(8)	0
N1	0.009(2)					
N2	0.009(2)					

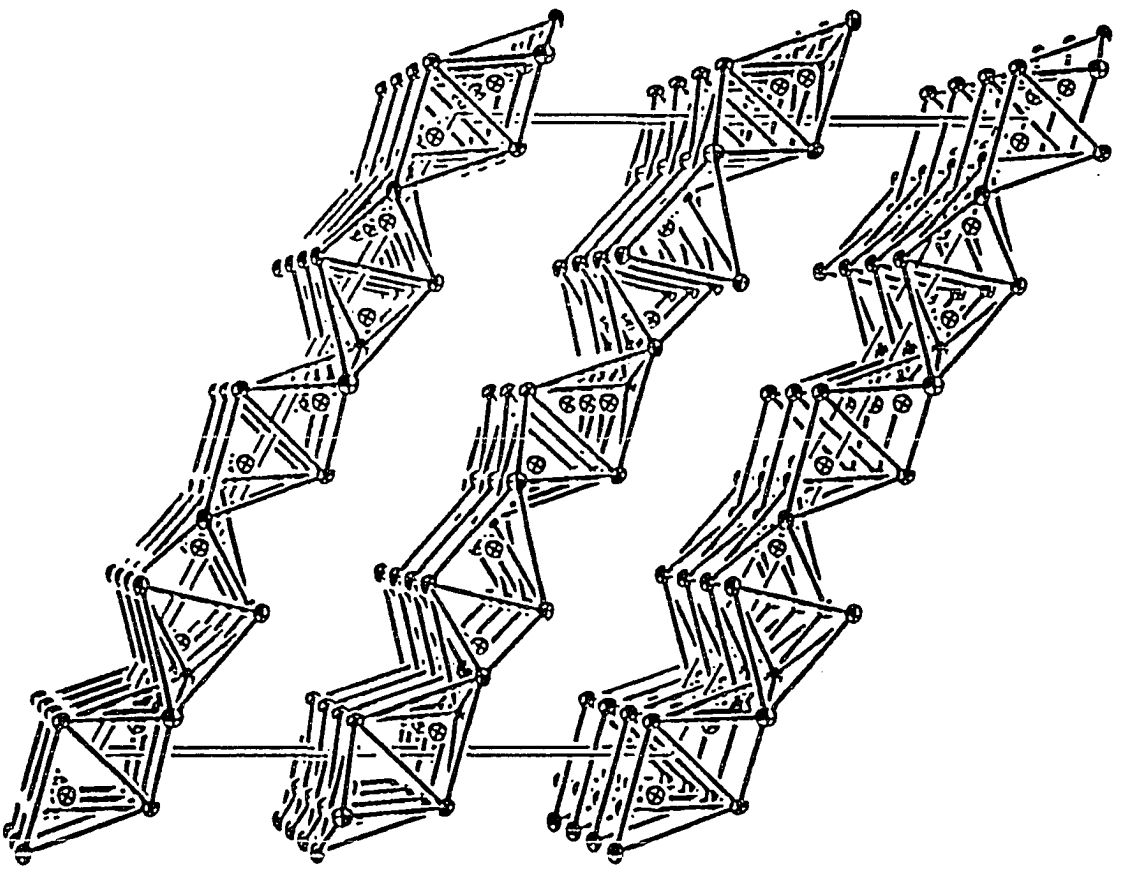

Figure 41. Unit cell projection along [0$\bar{1}$0] illustrating the chains of edge-sharing $Pr_{4/2}$ tetrahedra that extend infinitely in the a-b plane at z=0, 1/2, and 1. $\vec{c}$ is horizontal, $\vec{a}$ is ~vertical.

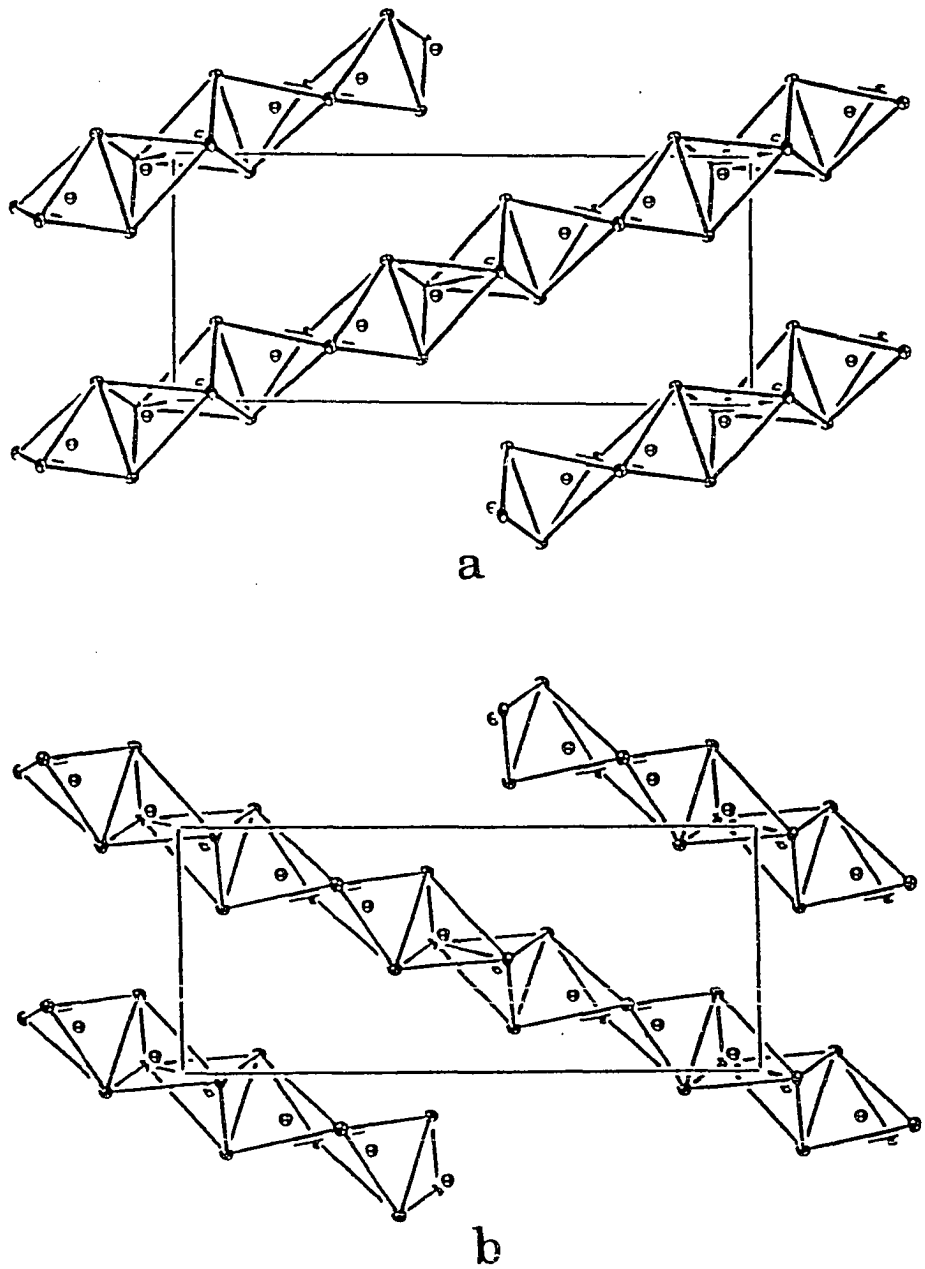

Figure 42. [00$\bar{1}$] view of the infinite chains within the a-b planes located at a) at z=0, where the chains extend along the [1$\bar{1}$0] direction and b) at z=1/2 with the chains running along the [110] direction. $\vec{a}$ is horizontal, $\vec{c}$ is vertical.

The chains of edge-sharing tetrahedra are composed of four crystallographically distinct Pr atoms and two unique light atom sites, as depicted in Figure 43a. This view clearly shows two types of octahedra, which are elongated so much that a *trans* bond forms. The first such type of octahedron is composed of Pr1, Pr2 and Pr4 atoms enclosing two N2 atoms, and the second is formed by Pr1, Pr2 and Pr3 atoms containing two N1 atoms. These octahedra, each of which degenerate into two tetrahedra, share Pr1-Pr2 edges forming an infinite zigzag chain. The interstitial atoms which are enclosed within one octahedron are related by an inversion center, located in the middle of each of these "octahedra". The Pr-Pr distances, listed along with other important bond distances and angles in Tables 30 and 31, range from 3.510(2) Å to 4.023(1)Å. The shared edges (Pr1-Pr2, Pr3-Pr3, Pr4-Pr4) of the tetrahedra are very short, with an average length of 3.53 Å. This distance is even shorter than that observed in Pr metal (3.64 Å),[89] yet the presence of metal-metal bonding is unlikely; powdering a shiny "black" crystal of $Pr_8Br_{13}N_3O$ resulted in a nearly white material, indicating that the material should be a valence compound dominated by Pr-(N,O) and Pr-Br interactions. The Pr-(N,O) distances range from 2.299(9) Å to 2.41(1) Å with an average of 2.34 Å for both N1 and N2 atoms. This average value is very close to the sum of crystal radii,[94] 2.35 Å, for N^{-3}, and Pr^{+3}, and is comparable to the M-Z distances observed in both α-Gd_2Cl_3N[58] (~2.27 Å) and Sm_4OCl_6[60] (~2.37 Å) when the appropriate size differences of the metals are considered. The environments of the N1 and N2

Table 30. Important bond distances in $Pr_8Br_{13}N_3O$

Pr1	–	Pr2[a]	3.544(1)	Pr2	–	Pr1[a]	3.544(1)	Pr3	–	Pr1	3.955(2)
	–	Pr3	3.955(2)		–	Pr3	4.015(1)		–	Pr1	3.917(2)
	–	Pr3	3.917(2)		–	Pr3	3.901(2)		–	Pr2	4.015(1)
	–	Pr4	4.023(1)		–	Pr4	3.975(2)		–	Pr2	3.901(2)
	–	Pr4	3.898(2)		–	Pr4	3.948(2)		–	Pr3[a]	3.565(2)
Pr4	–	Pr1	4.023(1)	N1	–	Pr1	2.359(9)	N2	–	Pr1	2.35(1)
	–	Pr1	3.898(2)		–	Pr2	2.30(1)		–	Pr2	2.361(9)
	–	Pr2	3.975(2)		–	Pr3	2.299(9)		–	Pr4	2.34(1)
	–	Pr2	3.948(2)		–	Pr3	2.41(1)		–	Pr4	2.31(1)
	–	Pr4[a]	3.510(2)								
Pr1	–	Br1	2.891(2)	Pr2	–	Br3	2.929(2)	Pr3	–	Br1	3.029(2)
	–	Br2	2.946(2)		–	Br4	3.164(2)		–	Br2	3.129(2)
	–	Br4	3.190(2)		–	Br4	3.369(2)		–	Br3	3.152(2)
	–	Br5	3.107(2)		–	Br5	3.127(2)		–	Br4	3.116(2)
	–	Br7	3.164(2)		–	Br6	3.081(2)		–	Br6	3.326(2)
	–	N1	2.359(9)		–	N1	2.30(1)		–	Br7	3.306(1)
	–	N2	2.35(1)		–	N2	2.361(9)		–	N1	2.299(9)
Pr4	–	Br1	3.232(2)	Br1	–	Pr1	2.891(2)		–	N1	2.41(1)
	–	Br2	3.020(2)		–	Pr3	3.029(2)	Br3	–	Pr2	2.929(2)
	–	Br3	3.036(2)		–	Pr4	3.232(2)		–	Pr3	3.152(2)
	–	Br5	3.061(2)	Br2	–	Pr1	2.946(2)		–	Pr4	3.036(2)
	–	Br6	3.148(2)		–	Pr2	3.129(2)	Br4	–	Pr1	3.190(2)
	–	N2	2.34(1)		–	Pr4	3.020(2)		–	Pr2	3.164(2)
	–	N2	2.31(1)						–	Pr3	3.116(2)
Br5	–	Pr1	3.107(2)	Br6	–	Pr2	3.081(2)	Br7	–	Pr1 (x2)	3.164(2)
	–	Pr2	3.127(2)		–	Pr3	3.326(2)		–	Pr3 (x2)	3.306(1)
	–	Pr4	3.061(2)		–	Pr4	3.148(2)				
N1	–	N1	3.08(2)	Br1	–	Br2[b]	3.615(2)	Br2	–	Br3	3.621(2)
	–	N2	2.97(1)	Br1	–	Br2	3.408(2)	Br3	–	Br4	3.559(2)
N2	–	N2	3.05(2)	Br1	–	Br3	3.592(3)	Br4	–	Br4	3.606(3)
				Br1	–	Br5	3.524(2)	Br4	–	Br5	3.540(2)

a Length of shared tetrahedral edge.
b Only Br-Br distances ≤3.70 Å, sum of van der Waals radii, are listed.

Table 31. Selected bond angles in $Pr_8Br_{13}N_3O$

Pr2-Pr1-Pr3	62.40(2)	Pr1-Pr3-Pr2	102.26(3)	Pr1-Br4-Pr3	76.79(4)
Pr2-Pr1-Pr3	64.88(2)	Pr1-Pr3-Pr3	63.62(4)	Pr2-Br4-Pr3	145.68(6)
Pr2-Pr1-Pr4	63.01(3)	Pr2-Pr3-Pr2	126.49(3)	Pr1-Br5-Pr2	112.72(5)
Pr3-Pr1-Pr3	63.88(3)	Pr2-Pr3-Pr3	61.61(3)	Pr1-Br5-Pr4	162.43(6)
Pr3-Pr1-Pr4	53.85(4)	Pr2-Pr3-Pr3	64.88(3)	Pr2-Br5-Pr4	79.93(4)
Pr3-Pr1-Pr4	75.69(3)	Pr1-Pr4-Pr1	127.41(3)	Pr2-Br6-Pr3	77.50(4)
Pr3-Pr1-Pr4	116.50(3)	Pr1-Pr4-Pr2	52.61(2)	Pr2-Br6-Pr4	175.22(7)
Pr3-Pr1-Pr4	121.79(3)	Pr1-Pr4-Pr2	101.09(3)	Pr3-Br6-Pr3	99.82(5)
Pr3-Pr1-Pr4	119.94(3)	Pr1-Pr4-Pr4	61.88(3)	Pr1-Br7-Pr1	162.73(8)
Pr4-Pr1-Pr4	52.59(3)	Pr1-Pr4-Pr2	102.84(3)	Pr1-Br7-Pr3 (x2)	101.22(4)
Pr1-Pr2-Pr3	63.97(3)	Pr1-Pr4-Pr2	53.71(3)	Pr1-Br7-Pr3 (x2)	74.47(4)
Pr1-Pr2-Pr3	62.05(3)	Pr1-Pr4-Pr4	65.54(4)	Pr3-Br7-Pr3	151.81(8)
Pr1-Pr2-Pr4	64.38(2)	Pr2-Pr4-Pr2	127.41(3)	Pr1-N1-Pr2	99.1(4)
Pr1-Pr2-Pr4	62.41(2)	Pr2-Pr4-Pr4	63.31(4)	Pr1-N1-Pr3	114.4(4)
Pr3-Pr2-Pr3	53.51(3)	Pr2-Pr4-Pr4	64.09(4)	Pr1-N1-Pr3	112.0(4)
Pr3-Pr2-Pr4	120.51(3)	Pr1-Br1-Pr3	83.80(5)	Pr1-N1-Pr3	121.7(4)
Pr3-Pr2-Pr4	116.33(3)	Pr1-Br1-Pr4	78.85(4)	Pr1-N1-Pr3	111.8(4)
Pr3-Pr2-Pr4	118.94(3)	Pr3-Br1-Pr4	100.58(4)	Pr1-N1-Pr3	98.3(4)
Pr3-Pr2-Pr4	75.73(3)	Pr1-Br2-Pr3	110.78(5)	Pr1-N2-Pr2	97.5(3)
Pr4-Pr2-Pr4	52.59(3)	Pr1-Br2-Pr4	84.77(4)	Pr1-N2-Pr4	118.1(4)
Pr1-Pr3-Pr1	126.15(4)	Pr3-Br2-Pr4	107.34(4)	Pr1-N2-Pr4	113.3(4)
Pr1-Pr3-Pr2	99.58(3)	Pr2-Br3-Pr3	79.71(4)	Pr1-N2-Pr4	115.5(4)
Pr1-Pr3-Pr2	53.63(3)	Pr2-Br3-Pr4	82.87(5)	Pr1-N2-Pr4	98.1(3)
Pr1-Pr3-Pr3	62.52(4)	Pr3-Br3-Pr4	102.24(4)		
Pr1-Pr3-Pr2	53.07(2)	Pr1-Br4-Pr2	109.54(5)		

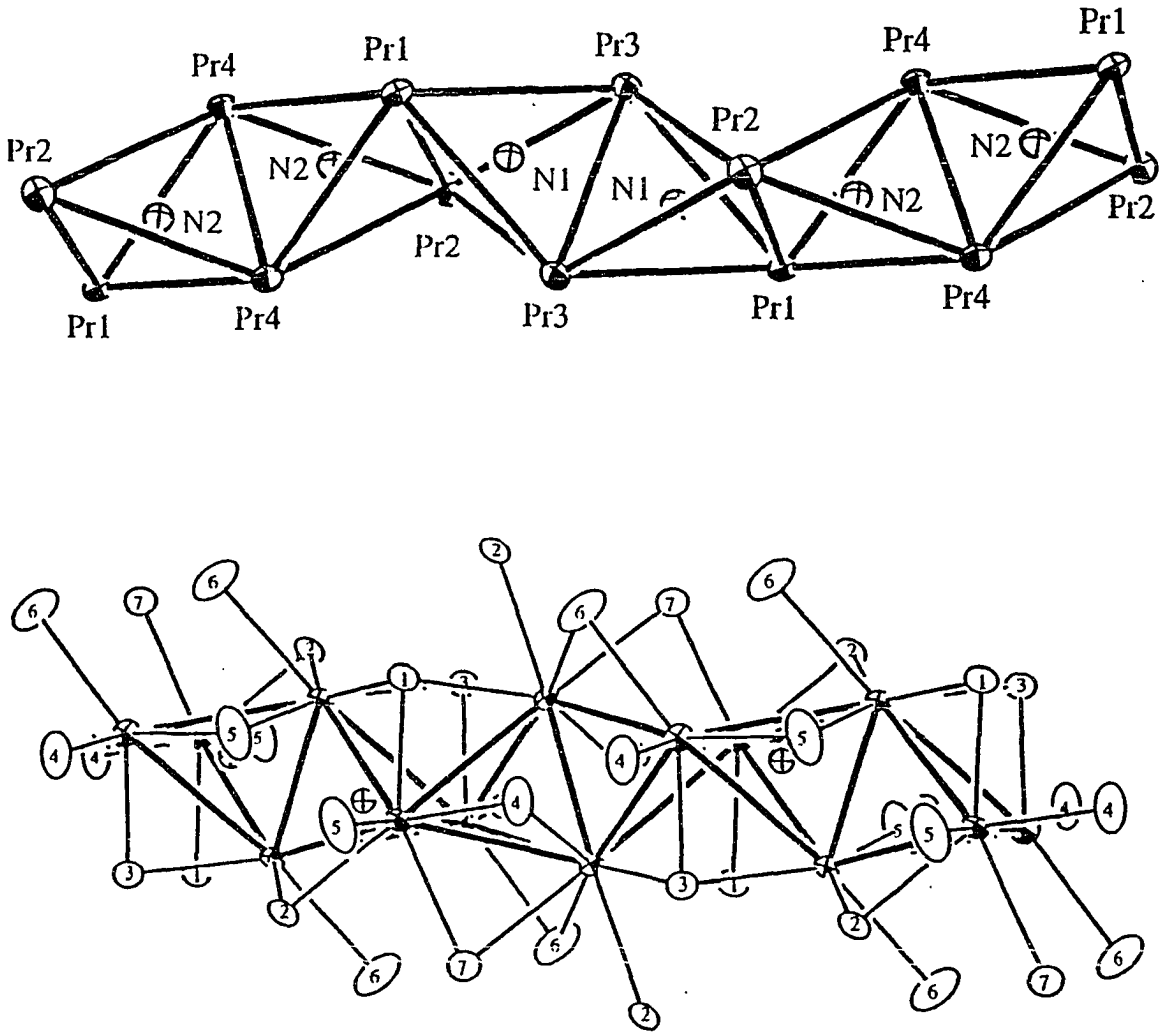

Figure 43. a) Illustration of the zigzag chains of edge-sharing "octahedra" that distort to form Pr tetrahedra, which are centered by (N,O). b) The halogen coordination around the chain composed of Br atoms bridging edges of Pr_4 tetrahedra and occupying sites exo to each Pr vertex.

sites are very similar, the only difference being a slightly wider range of observed Pr-N distances and Pr-N-Pr angles for N1 compared to N2. This may indicate that the N1 site is occupied by both O and N, resulting in a more geometry, but the results are not conclusive.

The zigzag chains of tetrahedra are surrounded by seven crystallographically unique Br atoms, which bridge the four open edges of each tetrahedron and occupy sites exo to the four Pr atoms, as shown in Figure 43b in a view slightly rotated from that in Figure 43a. The halogens exhibit four basic functionalities: $Br^{i\text{-}i}$ to one chain, $Br^{i\text{-}a}$ and $Br^{a\text{-}i}$ between chains in the same orientation (and height along $\vec{c}$), $Br^{i\text{-}i}$ to two chains, and $Br^{i\text{-}a}$ and $Br^{a\text{-}i}$ between chains in different orientations (and different heights along $\vec{c}$). The first functionality is shown in Figure 43b, where three-bonded Br1 and Br3 atoms simultaneously bridge two edges, the Pr1-Pr3 and Pr1-Pr4 edges and the Pr2-Pr3 and Pr2-Pr4 edges, respectively. The Pr-Br-Pr angles to the edge-bridged atoms are near 80°, while the third angle is 100° or greater. Also, one of the three Pr-Br bond distances is much longer (by at least 0.12 Å) than the other two. The second halogen functionality, illustrated in Figure 44, interconnects the $Pr_{4/2}$ chains within the a-b plane at z=0 and 1/2. The Br4 atoms bridge the Pr1-Pr3 edge while bonding exo to a Pr2 vertex in the neighboring chain. Meanwhile, Br5 atoms bridge the Pr2-Pr4 edge and bond exo to the Pr1 vertex in the adjacent chain. The third and fourth halogen functionalities are shown in Figure 45, which portrays Br interconnections between a chain at z=0 and one

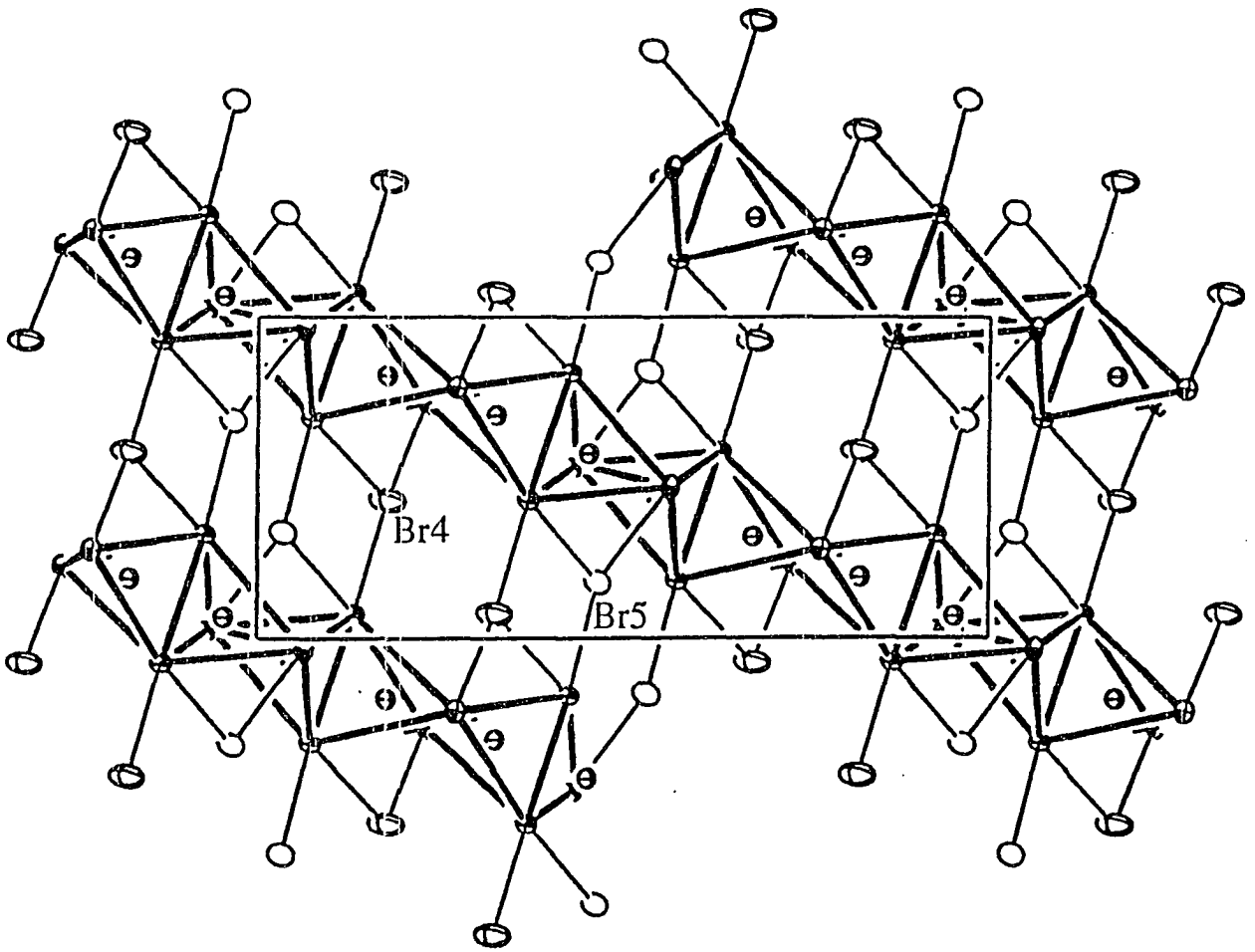

Figure 44. [00$\bar{1}$] view of the Br atoms interconnecting chains in the same orientations (within the a-b plane). Br4 and Br5 atoms bridge one edge of a tetrahedron while bonding exo to a Pr vertex in the adjacent chain. $\vec{a}$ is horizontal, $\vec{c}$ is vertical.

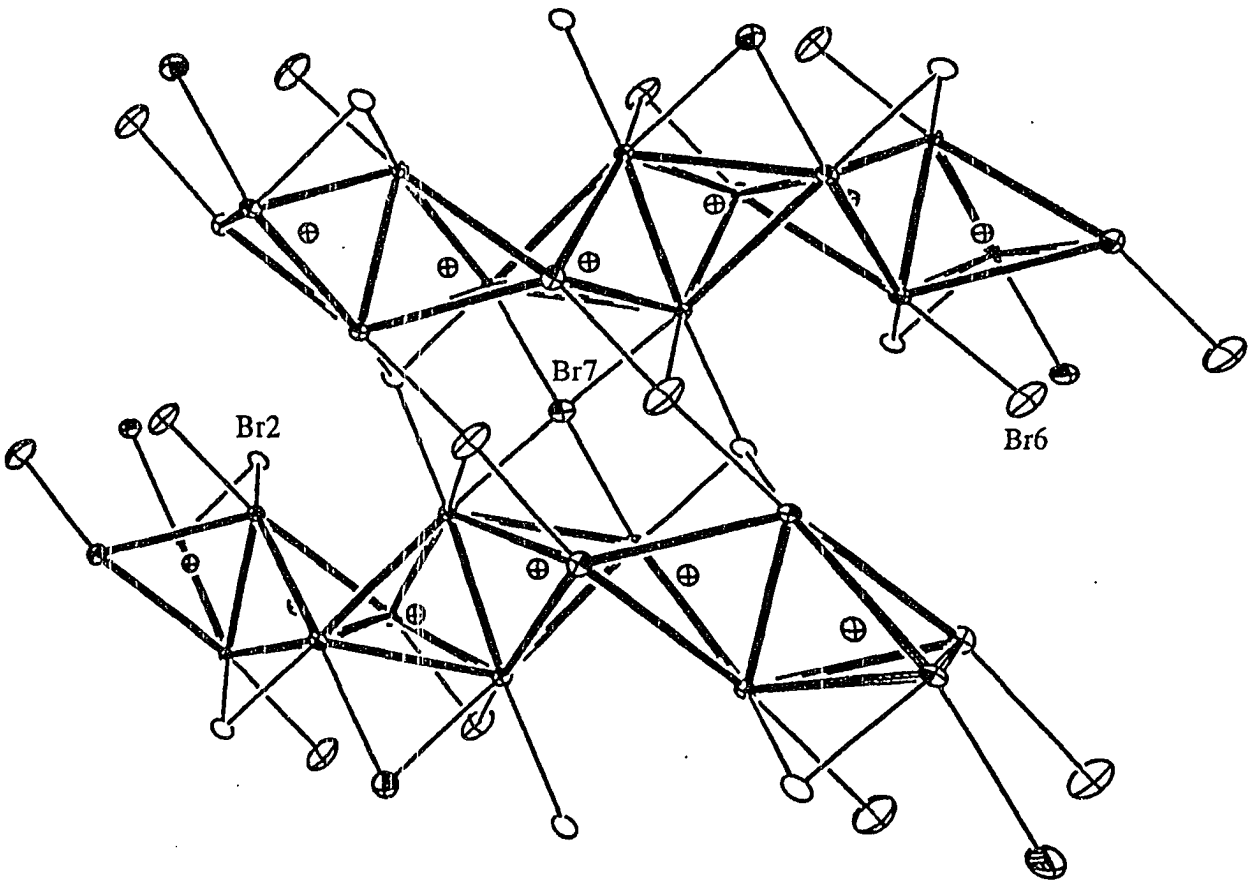

Figure 45. Representation of the halogen interconnections between a chain at z=0 and one at z=1/2. Br2 and Br6 atoms bridge edges and also bond exo to Pr in the neighboring chain, while Br7 bonds inner to both chains. $\vec{c}$ is vertical.

at z=1/2 in the center of the picture. The Br2 atoms are bridging the Pr1-Pr4 edges while bonding exo to a Pr3 vertex in the adjacent chain. Similarly, Br6 atoms bridge the Pr2-Pr3 edge of one tetrahedra while bonding exo to a Pr4 vertex in the tetrahedral chain below or above the first (along $\vec{a}$). The Pr-Br^{i-i}-Pr angles (for edge-bridging Br atoms) fall between 74° to 85°, where the most acute value is exhibited by Br7 atoms. The Pr-Br bond distances do not show a regular trend based on Br functionalities.

The coordination environments of the trivalent Pr atoms are rather irregular. The Pr1, Pr2, and Pr4 atoms are coordinated by a total of seven Br and (N,O) atoms forming a monocapped trigonal prism, illustrated for Pr1 in Figure 46a. Pr3 is surrounded by a total of eight Br and (N,O) atoms that constitute a bi-capped trigonal prism, as seen in Figure 46b. Both of these geometries are observed in the binary Pr_2Br_5, which has been formulated as $(Pr^{+3})_2(Br^-)_5(e^-)$. The Pr-Br bond distances range from 2.891(2) Å to 3.326(2) Å, with at least one longer than normal bond (≥3.19 Å) to every Pr atom. Several Br atoms display unusually close halogen contacts; the shortest Br-Br distance is 3.408(2), 0.3 Å shorter than expected van der Waals distances.

The compound $Pr_8Br_{13}N_3O$ is very similar to α-Gd_2Cl_3N, both structurally and (presumably) electronically. α-Gd_2Cl_3N also consists of edge-sharing M_4Z tetrahedra forming isolated infinite chains, as pictured in Figure 47. The coordination sphere of the Gd atoms in this phase were also characterized by some unusually long M-X distances. As in $Pr_8Br_{13}N_3O$, this Gd compound

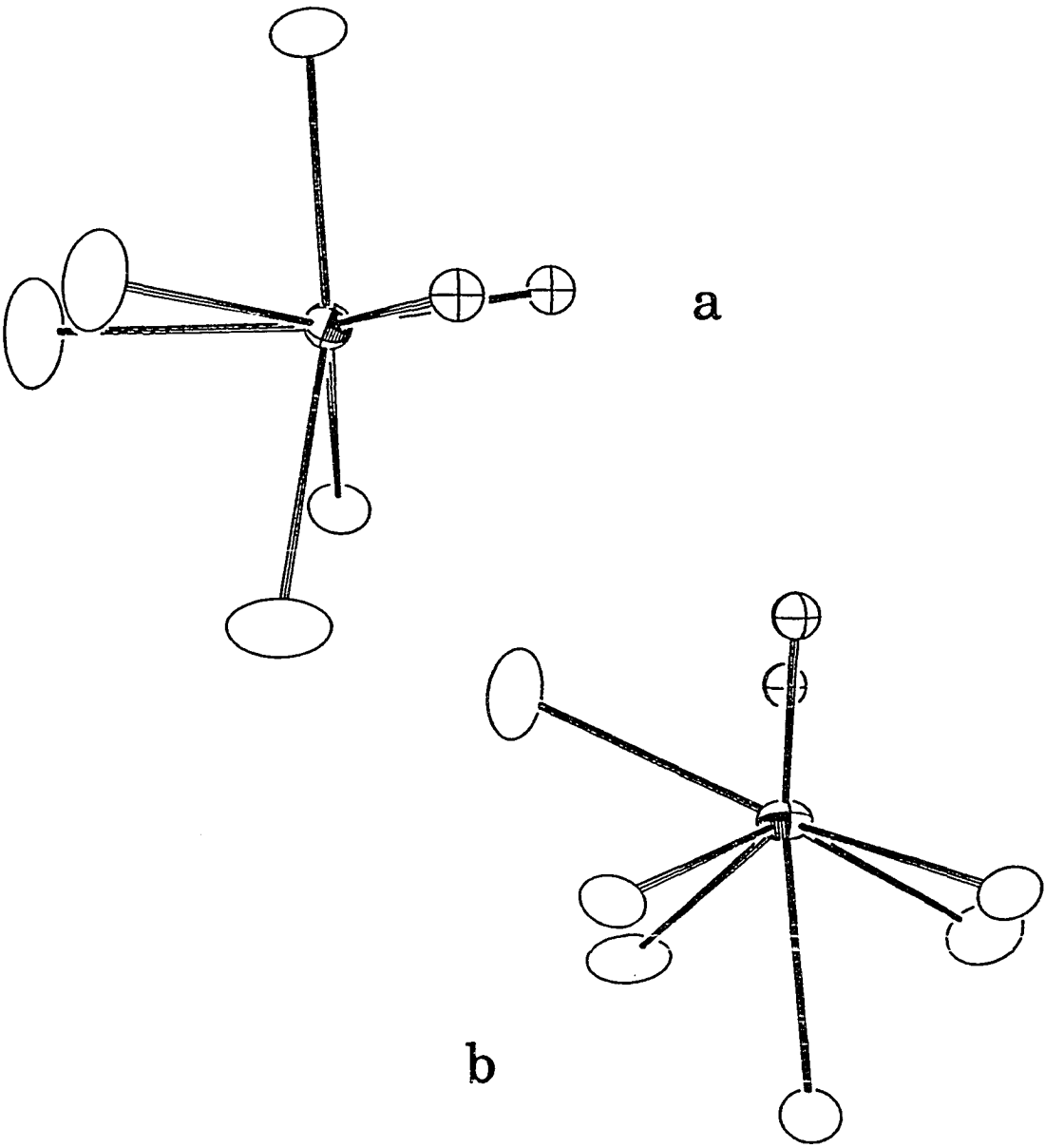

Figure 46. The coordination environments around a)Pr1 atoms, which center a monocapped trigonal prism of Br and (N,O) atoms, and b) Pr3 atoms, centering a bicapped trigonal prism.

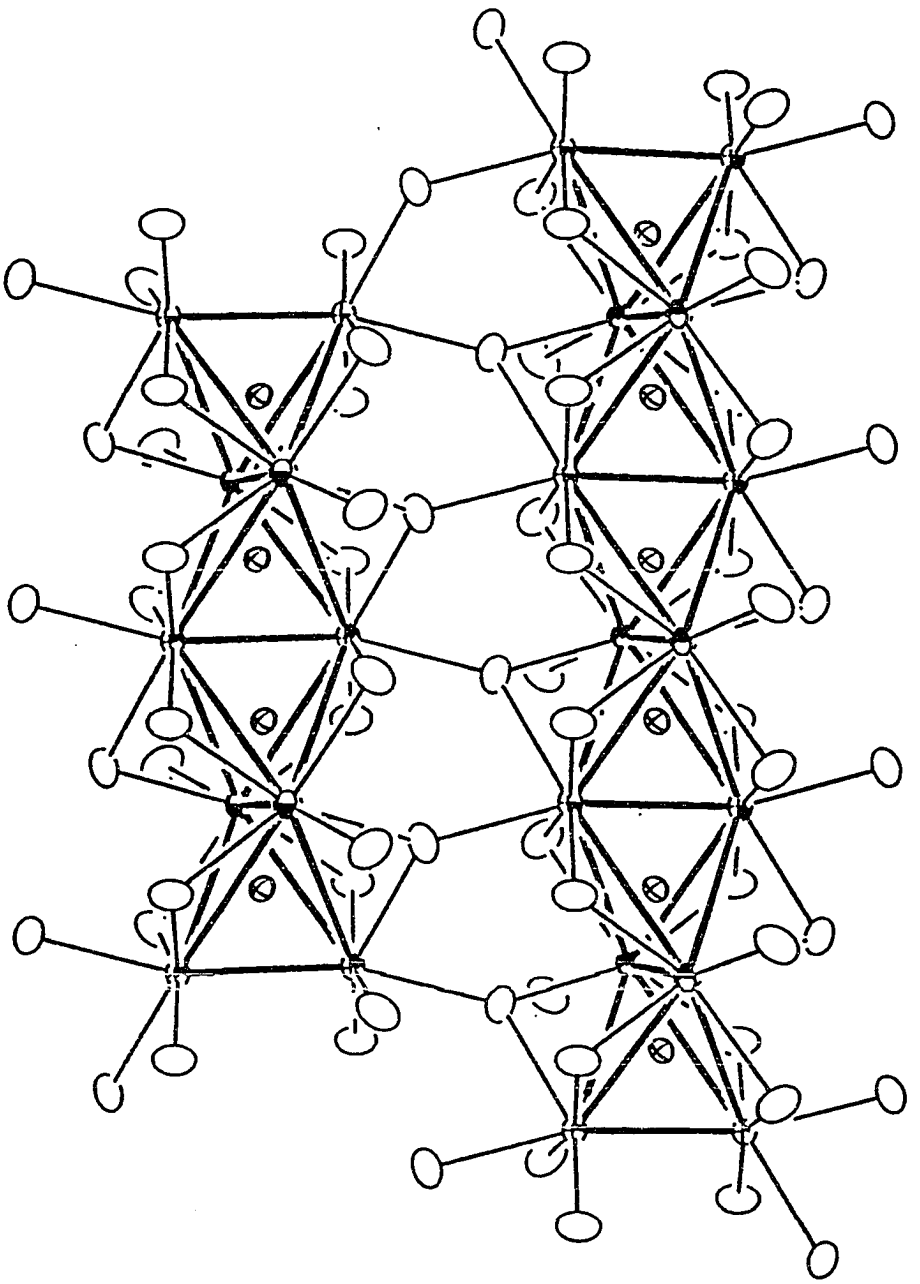

Figure 47. The structure of Gd_2Cl_3N, composed of edge-sharing tetrahedra similar to those found in $Pr_8Br_{13}N_3O$.

features very short M-M distances, although no M-M bonding is present; the dominant interactions are between Gd and N or Cl atoms. In fact, $Pr_8Br_{13}N_3O$ is nearly a sesquibromide, $Pr_2Br_{3.25}(N,O)$, where the addition of an extra Br atom electronically balances the mixed interstitial composition and results in a more distorted salt-like compound. Notably, many M_4OCl_6 phases are known that contain O atoms centering similar rare-earth metal tetrahedra. Thus, this new Pr phase contains features common to both trivalent Gd (Gd_2Cl_3N) and divalent Eu, Yb and Sm (M_4OCl_6) compounds.

General Observations

Exploratory synthesis in the Y–Br–Z and Sc–Br–Z systems has led to the discovery of several new reduced rare-earth metal bromides which are stabilized by interstitial atoms (Z). The majority of these phases incorporate the relatively new $M_{16}Z_4$ cluster unit (M=rare-earth metal, Z=transition metal interstitial), now firmly established as an important building-block in rare-earth metal halide structural chemistry. This cluster unit has been observed in four different structure types, two of which are built of only $M_{16}Z_4$ clusters coordinated by halogens ($Y_{16}Br_{20}Ru_4$, $Y_{16}Br_{24}Ir_4$), and two that include other structural fragments in addition to $M_{16}Z_4$ clusters and coordinating halogens ($Y_{20}Br_{36}Ir_4$, $Sc_{20-x}Br_{28}Z_4$).

These four structure types display many characteristic structural features and dimensional relationships. Each phase is based on approximately cubic-close-packed layers of Br and interstitial atoms (Z), with the rare-earth metals occupying pseudo-octahedral holes around groups of Z atoms to form the

clusters. In each structure, the clusters are surrounded in a nearly identical fashion by 36 coordinating halogens. The manner in which these halogens are shared between clusters changes for each structure type depends on the identity of Z and the Br:M ratio; as this ratio increases, the sharing of Br atoms decreases, resulting in the presence of more basic Br atoms within the phases. Because of the similar geometries and Br coordination around the clusters, $Y_{16}Br_{20}Ru_4$ and the $Sc_{20-x}Br_{28}Z_4$ phases exhibit similar square networks of clusters linked via Br atoms. Rotating the clusters and coordinating Br atoms in these square networks by ~28° generates a second type of square network, found in $Y_{20}Br_{36}Ir_4$, where a new style of intercluster linkage via Br atoms is observed. The fourth structure type, displayed by $Y_{16}Br_{24}Ir_4$, contains pseudo-close-packed layers of clusters, which can be generated from the first square network by shifting alternate rows of cluster by half of a unit cell length. Efficient packing of the clusters within the halogen network is a major factor in determining the structural arrangement.

The geometry of the $M_{16}Z_4$ clusters varies in a characteristic fashion, with the clusters undergoing a series of distortions as illustrated in Figure 48. The distortion involves the contraction of the M1-M1-M1 triangular faces which correspond to truncation of the rare-earth metal tetra-capped tetrahedron. Along with this contraction, a reduction in the size of the Z_4 tetrahedron occurs, in concert with an increase in the distance between the M2 atoms that cap the pseudo-hexagonal faces of the truncated tetrahedron. Table 32 lists ratios of the

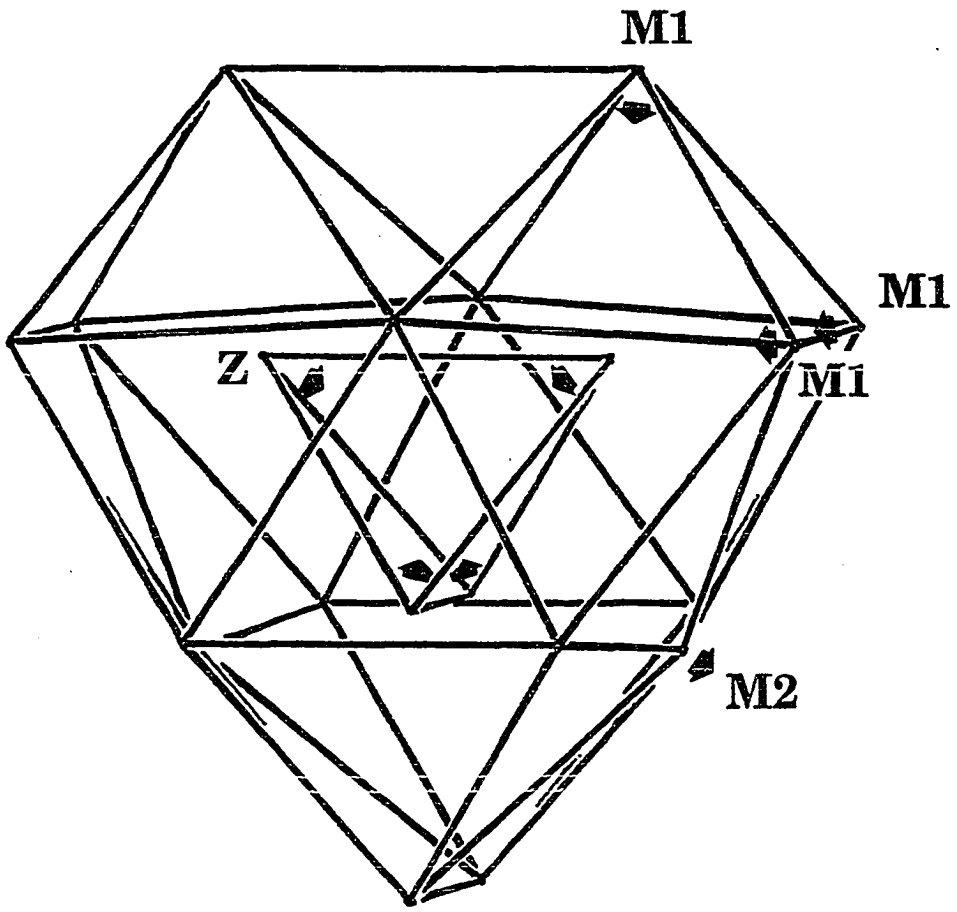

Figure 48. Illustration of the distortions exhibited by $M_{16}Z_4$ clusters. M1 triangular faces contract, while the Z_4 tetrahedron shrinks in concert with the movement of M2 away from the cluster center.

Table 32. Distance ratios, angles and bond orders helpful in understanding the distortions in $M_{16}Z_4$ clusters.

	$\bar{d}_{M1\Delta}/\bar{d}_{M2\text{-}M2}$	$\bar{d}_{M1\Delta}/d(1)_M$	$\bar{d}_{M1\Delta}/\bar{d}_{clus}$	$\bar{d}_{Z\text{-}Z}/\bar{d}(1)_Z$	Bond Order (Z–Z)	M1-Z-M2 Angle
$Y_{16}I_{20}Ru_4$[a]	0.842	1.125	0.967	1.433	0.02	169.57(5)
$Y_{16}Br_{20}Ru_4$	0.813	1.113	0.976	1.348	0.04	165.52(9)
$Y_{20}Br_{36}Ir_4$	0.814	1.133	0.983	1.326	0.04	164.3(2)
$Y_{16}Br_{24}Ir_4$	0.806	1.124	0.976	1.310	0.05	163.9(2)
$Sc_{20\text{-}x}Br_{28}Ru_4$	0.766	1.141	0.949	1.235	0.11	160.5(2)
$Sc_{20\text{-}x}Br_{28}Os_4$	0.764	1.144	0.950	1.202	0.14	159.3(2)
$Sc_{20\text{-}x}Br_{28}Mn_4$	0.729	1.120	0.942	1.183	0.19	153.2(3)
$Gd_{20}I_{28}Mn_4$[b]	0.730	1.103	0.952	1.200	0.16	148.3(2)

[a] from reference 62
[b] from reference 63

average distance in the M1-M1-M1 triangular faces to the average M2-M2 distance, to Pauling's single bond distance, and to the average M-M distance within the cluster. Also included are the ratios of the observed Z-Z distance to Z-Z single bond distance, the Z-Z bond order, and the *trans* M1-Z-M2 angle across M_6Z "octahedra". The gradual displacement of the Z atoms toward the cluster center strongly influences the *trans* M1-Z-M2 angles; the resulting interactions between Z and M2 atoms drive the M2 atoms farther away from the cluster center, giving a more acute *trans* angle. A comparison of the $\bar{d}(M_1\text{-}M_1)$:$\bar{d}(M_2\text{-}M_{2)}$ ratios shows a distinction between the Y clusters and the remaining clusters. The Y cluster framework values are fairly consistent regardless of the structure type, and only minimal Z-Z interaction is indicated. The Sc and Gd clusters, which are isostructural, show evidence of stronger Z-Z interactions, particularly with Mn as an interstitial.

The interesting new structures presented in this work are evidence of the subtle effect that slight differences in halogen size can have on determining structural stability. While the first examples of $M_{16}Z_4$ clusters were seen in iodides, the oligomeric unit appears to be more prolific with the smaller Br ligand. Similarly, the structure of $Pr_8Br_{13}N_3O$ incorporates one extra Br atom compared to the related chloride phases. The larger size of the halogen may allow for better coordination of the $Pr_{4/2}$ chains.

The electron count also has a large effect on the manner of halogen sharing; in all four $M_{16}Z_4$ structure types, the clusters maintain close to 60

electrons through a variety of structural modifications. The Y and Gd clusters achieve this exact count, while the Sc phases accommodate up to 61 electrons per cluster. In $Pr_8Br_{13}N_3O$, the additional electron from the oxygen atom (relative to α-Gd_2Cl_3N) coincides with the incorporation of another halogen atom, resulting in a new structural modification.

FUTURE WORK

During the last decade, exploratory research in rare-earth metal halide systems has resulted in a substantial number of new compounds which adopt a fascinating variety of structure types and contain several degrees of cluster condensation. Incorporation of a variety of interstitials, especially transition metals, has led to the discovery of many unique compounds which exhibit interesting electronic properties as well. One key to studying these properties, through either magnetic or electrical measurements, is the preparation of the material in high yield. Unfortunately, this has proved difficult in several of the systems investigated. Simply varying reaction temperatures and durations has not always resulted in single phase products. Although some success at increasing the yield has been found using alkali metal halides as flux agents, the formation of side products was troublesome. To avoid this problem, synthetic studies involving other materials as flux agents need to be conducted. A variety of alkaline-earth metal halides might prove to be more suitable at promoting crystal growth and not interfere greatly with magnetic measurements. This could also furnish suitable crystals for structural characterization of the many unidentified phases.

Additionally, the presence of a flux in certain reactions was observed to promote the formation of certain cluster phases over others, e.g. $Y_{16}Br_{24}Ir_4$ rather than $Y_{20}Br_{36}Ir_4$. This was observed in both the scandium bromide and yttrium bromide systems. The reason for this is unclear at present, although one might

speculate that the reaction processes are simply more rapid in the presence of the flux, thereby yielding products that were beyond the scope of the reaction times employed in synthesis. Alternately, the formation of ternary alkali-metal rare-earth metal halides may have a more subtle effect on the phase equilibria.

Continued research in the scandium bromide system should result in the discovery of new phases. Several promising unknowns have been observed, particularly with B and Os as interstitials. A number of phases that form as thin needles or fibers (especially for Z = Ir, Os, Re) may prove more difficult to characterize, owing to the propensity of these new phases to form as "mouse fur". Continued studies into the low temperature behavior of $Sc_{20-x}Br_{28}Os_4$ could provide insight into the nature of the transition observed in the magnetic susceptibility data. Low temperature powder diffraction should allow detection of a phase transition, if one should occur.

Lastly, the success of this research has shown that bromine chemistry can provide new and unexpected materials which have not been realized in either the chloride or iodide systems. Similarly, a rich structural chemistry exists in the zirconium bromide system, where several novel structure types unknown in either the chloride or iodide systems were discovered.[26] These results indicate that studies in other rare-earth metal bromide systems, perhaps La or Gd with transition metal interstitials, could be very fruitful.

REFERENCES

(1) Schäfer, H.; Schnering, H.-G. *Angew. Chem.* **1964**, *76*, 833.

(2) Wells, A. F. *Structural Inorg. Chem.*, 5th ed., Clarendon Press, Oxford, **1984**, 432-437.

(3) Simon, A.; von Schnering, H.-G.; Schäfer, H. *Z. Anorg. Allg. Chem.* **1968**, *361*, 235.

(4) Simon, A.; von Schnering, H.-G.; Wöhrle, H.; Schäfer, H. *Z. Anorg. Allg. Chem.* **1965**, *339*, 155.

(5) Schäfer, H.; Schnering, H.-G.; Niehues, K.-J.; Nieder-Vahrenholz, H. G. *J. Less-Common Met.* **1965**, *9*, 95.

(6) Bauer, D.; Schnering, H.-G. *Z. Anorg. Allg. Chem.* **1968**, *361*, 259.

(7) Corbett, J. D. *Pure and Applied Chem.* **1984**, *56*, 1527.

(8) Corbett, J. D.; McCarley, R. E. in *Crystal Chemistry and Properties of Materials with Quasi-One-Dimensional Structures*, J. Rouxel, ed. D. Reidel Publishing Company, Dordrecht, Holland, **1986**, 179-204

(9) Chevrel, R.; Sergent, M. in *Crystal Chemistry and Properties of Materials with Quasi-One-Dimensional Structures*, J. Rouxel, ed. D. Reidel Publishing Company, Dordrecht, Holland, **1986**, 315-373

(10) Bateman, L. R.; Blorent, J. F.; Dahl, L. F. *J. Am. Chem. Soc.* **1966**, *88*, 1082.

(11) Simon, A.; von Schnering, H.-G.; Schäfer, H. *Z. Anorg. Allg. Chem.* **1967**, *355*, 295.

(12) Meyer, H.-J.; Corbett, J. D. *Inorg. Chem.* **1991**, *30*, 963.

(13) Chevrel, R.; Sergent, M.; Prigent, J. *J. Solid State Chem.* **1971**, *3*, 515.

(14) Gronwold, F.; Kjekshus, A.; Raaum, F. *Acta Crystallogr.* **1961**, *14*, 930.

(15) Corbett, J. D. *Modern Perspectives in Inorganic Crystal Chemistry*, E.Parthé, ed. (NATO ASI Series C), Kluwer Academic Publishers, Dordrecht, The Netherlands, **1992**, 27-56.

(16) Simon, A. *Z. Anorg. Allg. Chem.* **1967**, *355*, 311

(17) Hwu, S.-J.; Corbett, J. D. *J. Solid State Chem.* **1986**, *64*, 331

(18) Ziebarth, R. P.; Corbett. J. D. *J. Am. Chem. Soc.* **1985**, *107*, 4571.

(19) Ziebarth, R. P.; Corbett, J. D. *J. Am. Chem. Soc.* **1987**, *109*, 4844.

(20) Ziebarth, R. P.; Corbett, J. D. *Acc. Chem. Res.* **1989**, *22*, 256.

(21) Ziebarth, R. P.; Corbett, J. D. *J. Am. Chem. Soc.* **1989**, *111*, 3272.

(22) Smith, J. D.; Corbett. J. D. *J. Am. Chem. Soc.* **1986**, *108*, 1927.

(23) Rosenthal, G.; Corbett, J. D. *Inorg. Chem.* **1988**, *27*, 53.

(24) Zhang, J.; Corbett, J. D. *Inorg. Chem.* **1991**, *30*, 431.

(25) Rogel, F.; Zhang, J.; Payne, M. W.; Corbett, J. D. *Adv. Chem. Ser.* **1990**, *226*, 369.

(26) Qi, R.-Y., Ph.D. Dissertation, Iowa State University, Ames, Ia, **1993**

(27) Smith, J. D.; Corbett, J. D. *J. Am. Chem. Soc.* **1985**, *107*, 5704.

(28) Hughbanks, T.; Rosenthal G.; Corbett. J. D. *J. Am. Chem. Soc.* **1988**, *110*, 1511.

(29) Rogel, F.; Corbett, J. D. *J. Am. Chem. Soc.* **1990**, *112*, 8198.

(30) Hughbanks, T.; Corbett. J. D. *Inorg. Chem.* **1989**, *28*, 631.

(31) Payne,M. W.; Corbett, J. D. *Inorg.Chem.* **1990**, *29*, 2246.

(32) Llusar, R.; Corbett, J. D. *Inorg. Chem.* **1994**, *33*, 849

(33) Hughbanks, T.; Corbett, J. D. *Inorg. Chem.* **1988**, *27*, 2022.

(34) Park, Y.; Corbett, J. D. *Inorg. Chem.* **1994**, *33*, 1705

(35) Simon, A.; Warkentin, E.; Masse, R. *Angew. Chem.* **1981**, *93*, 1071

(36) Masse R.; Simon A. *Mater. Res. Bull.* **1981**, *16*, 1007

(37) Warkentin, E.; Masse, R.; Simon, A.*Z. Anorg. Allg. Chem.* **1982**, *491*, 323

(38) Simon, A. *J. Solid State Chem.* **1985**, *57*, 2

(39) Kauzlarich, S.; Hughbanks, T.; Corbett, J. D.; Klavins, P.; Shelton, R. N. *Inorg. Chem.* **1988**, *27*, 1791

(40) Payne, M. W.; Dorhout, P. K.; Corbett, J. D. *Inorg. Chem.* **1991**, *30*, 1467.

(41) Dorhout, P. K.; Corbett, J. D. *J. Am. Chem. Soc.* **1992**, *114*, 1697

(42) Payne, M. W.; Dorhout, P. K.; Kim, S.-J.; Hughbanks, T. R.; Corbett, J. D. *Inorg. Chem.* **1992**, *31*, 1389

(43) Mattausch, Hj.; Schwarz, C.; Simon, A. *Z. Kristallagor.* **1987**, *178*, 156

(44) Mattausch, Hj.; Eger, S. R.; Simon, A. *Z. Anorg. Allg. Chem.* **1985**, *530*, 43

(45) Schwanitz-Schüller, U.; Simon, A. *Z. Naturforsch.* **1985**, *B 40*, 935

(46) Ruck, M.; Simon, A.; *Z. Anorg. Allg. Chem.* **1993**, *619*, 327

(47) Warkentin, E.; Simon, A. *Rev. Chim. Miner.* **1983**, *20*, 488

(48) Dorhout, P. K.; Payne, M. W.; Corbett, J. D. *Inorg. Chem.* **1991**, *30*, 4960.

(49) Simon, A; Mattausch, Hj.; Miller, G. J.; Bauhofer, W.; Kremer, R. K. in *Handbook on the Physics and Chemistry of Rare Earths,* Gschneidner, K. A., Eyring, L., Eds., Elsevier Science Publishers: North-Holland, The Netherlands, **1991**, *Vol. 15*, 191-285

(50) Meyer, G. *Chem. Rev.* **1988**, *88*, 93

(51) Artelt, H. A.; Schleid, T.; Meyer, G. *Z. Anorg. Allg. Chem.* **1992**, *618*, 18

(52) Uhrlandt, S.; Meyer, G., *Angew. Chem. Int. Ed. Eng.*, **1993**, *32*, 1318

(53) Artelt, H. M.; Uhrlandt, S.; Meyer, G. *Z. Anorg. Allg. Chem.* manuscript in preparation.

(54) Artlelt, H. M.; Meyer, G. *Z. Anorg. Allg. Chem.* **1993**, *619*, 1

(55) Imoto, H.; Corbett, J. D.; Cisar, A. *Inorg. Chem.* **1981**, *20*, 145

(56) Simon, A.; Koehler, T. *J. Less-Common Met.* **1986**, *116*, 279

(57) Schwanitz-Schüller, U.; Simon, A. *Z. Naturforsch,* **1985**, *40B*, 705

(58) Meyer,H.-J.; Jones, N. L.; Corbett, J. D. *Inorg. Chem.* **1989**, *28*, 2635

(59) Schleid, Th.; Meyer, G. *J. Less-Common Met.* **1987**, *127*, 161

(60) Schleid, Th.; Meyer, G. *Z. Anorg. Allg. Chem.* **1987**, *554*, 118

(61) Mattfeld, H.; Krämer, K.; Meyer, G. *Z. Anorg. Allg. Chem.* **1993**, *619*, 1384

(62) Payne, M. W.; Ebihara, M.; Corbett, J. D. *Angew. Chem., Int. Ed. Engl.* **1991**, *30*, 856.

(63) Ebihara, M.; Martin, J. D.; Corbett, J. D. *Inorg. Chem.* **1994**, *33*, 2079

(64) Hwu, S.-J. Ph.D. Dissertation, Iowa State University, Ames, IA, **1985**

(65) Meyer, G.; Dötsch, S.; Staffel, T. *J. Less-Common Met.* **1987**, *127*, 155

(66) Meyer, G.; Staffel, T.; Dötsch, S.; Schleid, T. *Inorg. Chem.* **1985**, *24*, 3504

(67) Corbett, J. D. in *Solid State Chemistry Techniques* Cheetham, A. K.; Day, P. Eds., Oxford University Press, New York, U.S.A. **1988**, 31-33

(68) Seaverson, L. M.; Corbett, J. D. *Inorg. Chem.* **1980**, *10*, 1241

(69) Poeppelmeier, K. R.; Corbett, J. D. *Inorg.Chem.* **1977**, *16*, 294.

(70) Schaeffer, H. A. in *Concise Encyclopedia of Semiconducting Materials and Related Technologies* Mahajan, S.; Kimerling, L. C. Eds., Permagon Press, Tarrytown, NY., U.S.A. **1992**, 457-458

(71) Miller, A. E.; Daane, A. H.; Haberman, C. E.; Beaudry, B. J. *Rev. Sci. Inst.* **1963**, *34*, 644.

(72) Schäfer, H. *Chemical Transport Reactions*, Academic Press Inc., New York, **1964**, Chapter 2.

(73) Holland L. *The properties of Glass Surfaces*, Chapman and Hall, London, **1966**, Chapter 4.

(74) *JCPDS Powder Diffractiion File* International Center for Diffraction Data, Swarthmore, PA., U.S.A, **1992**

(75) Clark, C. M.; Smith, D. k.; Johnson, G. J. A Fortran IV Program for Calculating X-Ray Powder Diffraction Patterns - Version 6, Department of Geosciences, Pennsylvania State University: University Park, PA, **1973**.

(76) Imoto, H., Ames Laboratory, Iowa State University, Ames, IA., unpublished research, **1978**.

(77) Takusagawa, F., Ames Laboratory, Iowa State University, unpublished research, **1981**.

(78) Werner, P. E. TREOR-V5, Department of Strusture Chem., Arrhenius Laboratory, University of Stockholm: Stockholm, Sweden, **1984**.

(79) Sheldrick, G. M., SHELXS-86, Programs for Structure Determination, Universit Göttingen, Germany, **1986**.

(80) TEXSAN: Single Crystal Structure Analysis Software, Version 5.0, Molecular Structure Corporation, The Woodlands, TX, **1989**.

(81) International Tables for X-Ray Crystallography, Kynoch Press: Birmingham, England, **1968**, Vol. III.

(82) Walker, N.; Stuart *Acta Cryst.* **1983**, *A39*, 158

(83) Johnson, C. K., ORTEP, A Fortran Thermal-Ellipsoid Plot Program for Crystal Structure Illustrations, Oak Ridge National Laboratory, Oak Ridge, TN, **1970**.

(84) Coppens, P.; Hamilton, W. C. *Acta Crystallogr.* **1970**, *A26*, 71.

(85) Köckerling, M., Iowa State University, Ames, IA., unpublished research, **1993**.

(86) Guthrie, D. H.; Meyer, G.; Corbett, J. D. *Inorg. Chem.* **1981**, *20*, 1192

(87) Meyer, H.-J., Iowa State University, Ames, IA., unpublished research, **1989**

(88) Pauling, L. *The Nature of the Chemical Bond*, Cornell University Press, Ithica, NY., U.S.A. **1960**, 403

(89) Pauling, L. *The Nature of the Chemical Bond*, Cornell University Press, Ithica, NY., U.S.A. **1960**, 410

(90) Converse, J. G.; McCarley, R. E. *Inorg. Chem.* **1970**, *9*, 1361

(91) Van Vleck, J. H. *The Theory of Electric and Magnetic Susceptibilities*, Oxford University Press, Oxford, England, **1932**, 277.

(92) Dudis, D. S.; Corbett, J. D.; Hwu, S.-J. *Inorg. Chem.* **1986**, *25*, 3434

(93) Karcher, B. Ph.D. Dissertation, Iowa State University, Ames, IA., **1981**

(94) Shannon, R. P. *Acta Crystallogr. Sec. A* **1976**, *A32, 751.*4

(95) Michaelis, C.; Simon, A., unpublished research, **1986**

(96) Hulliger, F. *Structural Chemistry of Layer-Type Phases*, D. Reidel Publishing Co., Dordrecht,Holland, **1976**, 333

(97) Bauhofer, C.; Mattausch, H.-J.; Miller, G. J.; Bauhofer, W.; Kremer, R. K.; Simon, A *J. Less-Common Met.*, **1990**, *167*, 65

(98) Martin, J. D., Iowa State University, Ames, IA., unpublished research, **1994**

(99) Hwu, S.-J.; Corbett, J. D.; Poeppelmeier, K. R. *J. Solid State Chem.* **1985**, *57*, 43

(100) Dudis, D. S.; Corbett, J. D. *Inorg. Chem.* **1987**, *26*, 1933

(101) McCollum, B. C.; Camp, M. J.; Corbett, J. D. *Inorg. Chem.* **1973**, *12*, 778

ACKNOWLEDGEMENTS

During my time at Iowa State University, I have been very fortunate to meet and work with many wonderful people too numerous to mention. I would like to extend special thanks to Dr. John D. Corbett, my major professor, for his patience, guidance, and support over the years. I am very grateful to Dr. Robert A. Jacobson and Dr. Robert E. McCarley for their many insightful discussions both in and out of the classroom.

I would like to acknowledge Dr. Jacobson's group members and Dr. Victor Young for their efforts in maintaining single crystal diffractometers, as well as Mr. Jerome Ostenson, for the measurement of magnetic properties. Ms. Shirley Standley deserves special recognition. Her help, friendship, and understanding has made my years as a graduate student more enjoyable. I also want to express my heartfelt appreciation to all my fellow group members, both past and present, for sharing their time, knowledge, and friendship with me on a daily basis.

I am very grateful to my parents and family for their love and inspiration, and especially to my brother Allan for sparking my interest in science. And finally, I wish to express my deepest thanks to my husband, Aaron, and children, Michael and Susan, whose constant help, encouragement, and love give my life meaning.